

**SURFACE ANALYSIS OF MATERIALS FOR
DIRECT WAFER BONDING**

**SURFACE ANALYSIS OF MATERIALS FOR DIRECT
WAFER BONDING**

By

ARIF UL ALAM, B.Sc.

A Thesis

Submitted to the School of Graduate Studies

In Partial Fulfillment of the Requirements

For the Degree

Master of Applied Science

McMaster University

© Copyright by Arif Ul Alam, October 2013

MASTER OF APPLIED SCIENCE (2013)

(Electrical and Computer Engineering)

McMaster University

Hamilton, Ontario, Canada

TITLE: Surface Analysis of Materials for Direct Wafer Bonding

AUTHOR: Arif Ul Alam, B.Sc. (Electrical and Electronic Engineering)
Islamic University of Technology (IUT), Bangladesh.

SUPERVISOR: Dr. Matiar R. Howlader

CO-SUPERVISOR Dr. Thomas E. Doyle

NUMBER OF PAGES: xi, 118

ABSTRACT

Surface preparation and its exposure to different processing conditions is a key step in heterogeneous integration of electronics, photonics, fluidics and/or mechanical components for More-than-Moore applications. Therefore, it is critical to understand how various processing and environmental conditions affect the surface properties of bonding substrates. In this thesis, the effects of oxygen reactive-ion etching (O₂ RIE) plasma followed by storage in ambient and 98% relative humidity on some key surface properties such as roughness, water contact angle, hardness, and the elemental and compositional states of three materials – silicon (Si), silicon dioxide (SiO₂) and glass – are investigated to analyze their influence on bondability.

Lower O₂ RIE plasma activation times cause low surface roughness, high surface reactivity and high hydrophilicity of Si, SiO₂ and glass. Although, the surface reactivity

of plasma- and ambient-humidity-treated Si and SiO₂ is considerably reduced, their reduction of roughness and increase of hydrophilicity may enable good bonding at low temperature heating due to augmented hydroxyl groups. The decrease of hardness of Si and SiO₂ with increased activation time is attributed to higher surface roughness and formation of amorphous layers of Si. While contact angle and surface roughness results show correlation with bondability, the role of hardness on bondability requires further investigation.

The high-resolution X-ray Photoelectron Spectroscopy (XPS) spectra of O₂ RIE treated Si, SiO₂ and glass showed the presence of Si(-O)₂ resulting in highly reactive surfaces. A considerable shift in the binding energy of Si(-O)₂ was observed only in Si. The ambient and 98% relative humidity storage of plasma-activated Si and SiO₂ increased Si(-OH)_x due to enhanced sorption of hydroxyls. The variation in the amounts of Si(-O)₂ and Si(-OH)_x in the ambient- and 98% relative humidity-stored Si were attributed to the crystal-orientation dependent surface roughness and oxidation of Si.

The surface roughness, contact angle and hardness measurement results and their correlation with the XPS results give useful insights into the direct wafer bonding of Si, SiO₂ and glass. Based on the analysis, the bondability of Si, SiO₂ and glass can be summarized. The high surface reactivity of Si, SiO₂ and glass obtained from oxygen plasma activation at lower activation times can result in better bondability. Also, the ambient humidity-induced Si(-OH)_x plays an important role in the hydrophilic wafer bonding of Si and SiO₂ which may require a low temperature heating.

ACKNOWLEDGEMENTS

This thesis would not have been possible without the cooperation, encouragement and support of many people. First of all, I would like to express my sincere gratitude to my supervisor Dr. Matiar R. Howlader, who has introduced me to the field of nanotechnology and provided me with thorough training and guidance in research, and helped me with learning the equipment in Micro- and Nano- Systems Laboratory (MNSL). His excellent supervision, utmost cooperation and incessant encouragement contributed greatly to this thesis. I also greatly appreciate my co-supervisor Dr. Thomas E. Doyle for his guidance.

I acknowledge Dr. M. Jamal Deen for his encouragements and suggestions. I would like to extend my appreciation to Fangfang Zhang for her assistance in the experiments. Without her help, the experiments presented in this thesis would have been very difficult

for me. I am indebted to Dr. Moon J. Kim, University of Texas at Dallas for his contribution to review and comment on my experimental results. I am especially grateful to Dr. Peter Cruse, Department of Chemistry at McMaster University for his critical comments and suggestions on X-ray Photoelectron Spectroscopy (XPS) results. I would like to acknowledge Mubeen Mashroor, Engineer, JEOL Canada for his special training in XPS instrument and his continuous support throughout my experimental works.

This research is supported by a discovery grant (#327947) from the Natural Science and Engineering Research Council (NSERC) of Canada and an infrastructure grant (#12128) from the Canada Foundation for Innovation (CFI). At last but not the least, I would like to thank my wife Kanij Sakara Nasrin, and my parents and brothers and sisters, for their eternal love, patience, and continuous encouragement throughout my study in Canada.

TABLE OF CONTENTS

ABSTRACT.....	III
ACKNOWLEDGEMENTS	V
TABLE OF CONTENTS	VII
LIST OF FIGURES	X
LIST OF TABLES	XII
CHAPTER 1.....	1
INTRODUCTION	1
1.1 SURFACE ANALYSIS FOR WAFER BONDING	1
1.2 DIRECT WAFER BONDING	2
<i>1.2.1 What is Direct Wafer Bonding?</i>	2
<i>1.2.2 High Temperature Wafer Bonding</i>	3
1.2.2.1 Hydrophilic Wafer Bonding	3
1.2.2.2 Hydrophobic Wafer Bonding	5
1.2.2.3 Anodic Bonding.....	6
<i>1.2.3 Low Temperature Wafer Bonding</i>	7
1.2.3.1 Plasma Activated Wafer Bonding	7

1.2.3.2	Sequential Plasma Activated Wafer Bonding	11
1.3	SURFACE PROPERTIES IN BONDING	12
1.3.1	<i>Role of Surface Morphology on Wafer Bonding</i>	12
1.3.2	<i>Role of Surface Hydrophilicity on Bonding</i>	17
1.3.3	<i>Role of Surface Mechanical Properties on Bonding</i>	19
1.4	SURFACE CHEMICAL STATE IN BONDING	20
1.5	CONTRIBUTIONS	24
1.6	OBJECTIVES AND OUTLINE OF THE THESIS	24
CHAPTER 2	26
EXPERIMENTAL PROCEDURES	26
2.1	SPECIMEN PREPARATION	26
2.2	HYBRID PLASMA BONDER.....	28
2.3	ATOMIC FORCE MICROSCOPY	29
2.4	DROP SHAPE ANALYSIS	32
2.5	NANOINDENTATION HARDNESS.....	34
2.6	X-RAY PHOTOELECTRON SPECTROSCOPY	37
2.7	HUMIDITY AND RELIABILITY CHAMBER	42
CHAPTER 3	44
SURFACE ROUGHNESS, CONTACT ANGLE AND HARDNESS	44
3.1	SURFACE ROUGHNESS	44
3.2	WATER CONTACT ANGLE.....	49
3.3	SURFACE HARDNESS	55
3.4	CONCLUSIONS	60
CHAPTER 4	63
SURFACE CHEMICAL ANALYSIS	63
4.1	SILICON	63
4.2	SILICON DIOXIDE.....	71
4.3	GLASS	75
4.4	CONCLUSIONS	78

CHAPTER 5.....	81
CONCLUSIONS AND FUTURE WORK.....	81
5.1 CONCLUSIONS	81
5.2 FUTURE WORK	84
APPENDIX I	86
APPENDIX II.....	90
APPENDIX III	98
REFERENCES.....	107

LIST OF FIGURES

FIGURE 1-1: SCHEMATICS OF DIFFERENT STAGES AT THE INTERFACE OF DIRECTLY BONDED WAFERS	4
FIGURE 1-2: SCHEMATIC OF PROPOSED MECHANISM FOR HYDROPHOBIC [Si(100)] WAFER BONDING	6
FIGURE 1-3: SCHEMATIC OF SURFACE-ACTIVATION-BASED NANOBONDING TECHNOLOGIES.....	10
FIGURE 1-4: SCHEMATIC FOR GAPS AT THE INTERFACE BETWEEN BONDED WAFERS	13
FIGURE 1-5: BONDING ENERGY AND REAL AREA OF CONTACT AS FUNCTIONS OF ADHESION PARAMETER...	15
FIGURE 1-6: CONCEPT OF BEARING RATIO	16
FIGURE 1-7: CONTACT ANGLE OF A DROP OF DI WATER AND AN INVERTED BUBBLE	18
FIGURE 1-8: XPS SPECTRUM OF THE GE (GERMANIUM) 3D CORE LEVEL OF DE-BONDED GE SURFACE.....	21
FIGURE 1-9: XPS SPECTRUM OF Si _{2p} REGIONS FOR FIVE OXIDATION STATES OF SILICON	22
FIGURE 1-10: O _{1s} SPECTRUM FOR THE X = 0.085 GLASS [(SiO ₂) _{0.7-x} (Na ₂ O) _{0.3} (Fe ₂ O ₃) _x] COMPOSITION.....	23
FIGURE 2-1: SCHEMATIC FOR SPAB PROCESS.....	28
FIGURE 2-2: WORKING PRINCIPLES OF AFM	30
FIGURE 2-3: THE FORMATION OF CONTACT ANGLE ON A SOLID SURFACE PROPOSED BY YOUNG	33

FIGURE 2-4: MEASUREMENT PRINCIPLE OF NANOINDENTATION HARDNESS TEST	36
FIGURE 2-5: DIFFERENT TYPES OF INDENTATION TESTS	37
FIGURE 2-6: SPECTROANALYTIC PROCESSES.....	39
FIGURE 2-7: PRINCIPLES OF X-RAY PHOTOELECTRON SPECTROSCOPY (XPS)	40
FIGURE 2-8: CROSS SECTION OF THE XPS ANALYSIS CHAMBER	41
FIGURE 2-9: PLATINOUS STERLING CHAMBER (ESL-2C)	43
FIGURE 3-1: THREE-DIMENSIONAL (3-D) AFM IMAGES OF SI WAFER SURFACES.....	45
FIGURE 3-2: SURFACE ROUGHNESS OF SI AS A FUNCTION OF O₂ RIE PLASMA ACTIVATION TIMES.....	46
FIGURE 3-3: THE DI WATER DROP SHAPE IMAGES ON SI SURFACES.....	49
FIGURE 3-4: CONTACT ANGLE OF SI AS FUNCTIONS OF ELAPSED TIME AND PLASMA ACTIVATION TIME	50
FIGURE 3-5: INDENTER FORCE VS. INDENTATION DEPTH AND MARTENS' HARDNESS OF SI, SiO₂, GLASS.....	57
FIGURE 4-1: WIDE-SCAN AND NARROW-SCAN XPS SPECTRA OF SI.....	65
FIGURE 4-2: DECONVOLVED XPS SPECTRA OF O_{1s} AND Si_{2p} FOR AS-RECEIVED SI	66
FIGURE 4-3: PERCENTAGE OF COMPONENTS IN O_{1s} XPS SPECTRA OF SI	68
FIGURE 4-4: WIDE-SCAN AND NARROW-SCAN XPS SPECTRA OF SiO₂.....	73
FIGURE 4-5: DECONVOLVED XPS SPECTRA OF O_{1s} FOR AS RECEIVED SiO₂.....	74
FIGURE 4-6: PERCENTAGE OF COMPONENTS IN O_{1s} XPS SPECTRA SiO₂	74
FIGURE 4-7: WIDE-SCAN AND NARROW-SCAN XPS SPECTRA OF GLASS	76

LIST OF TABLES

TABLE 2-1: DESCRIPTION OF THE MATERIALS, THEIR SURFACE ACTIVATION AND STORAGE CONDITIONS WITH THEIR CORRESPONDING ACRONYMS.	27
TABLE 3-1: SURFACE REACTIVITY OF Si, SiO ₂ AND GLASS AT DIFFERENT ACTIVATION TIMES FOR DIFFERENT TREATMENT AND STORAGE CONDITIONS.	51
TABLE 3-2: EVOLUTION OF SURFACE PROPERTIES WITH THE INCREASE OF OXYGEN PLASMA ACTIVATION TIMES AT DIFFERENT STORAGE CONDITIONS.	60
TABLE 4-1: ENERGY SHIFT AND CHANGE OF FWHM OF THE DECONVOLVED COMPONENTS OF O _{1s} AND Si _{2p} FOR Si AT DIFFERENT PLASMA TREATMENT AND STORAGE CONDITIONS	67
TABLE 4-2: EVOLUTION OF SURFACE PROPERTIES WITH THE INCREASE OF OXYGEN PLASMA ACTIVATION TIMES AT DIFFERENT STORAGE CONDITIONS.	78

CHAPTER 1.

INTRODUCTION

1.1 Surface Analysis for Wafer Bonding

Today's semiconductor industry faces a major challenge of heterogeneous integration of various technologies for emerging micro- and nano- systems in health, environmental, transportation and security applications. Typical examples for the emerging systems include DNA biosensors [1], wearable health-monitoring devices, biomedical sensing devices [2], and drug delivery devices for integrated therapeutic systems [3]. The More-than-Moore ITRS (International Technology Roadmap of Semiconductors) [4] scenario suggests that the surfaces of diverse substrates are required to be integrated onto a common platform. Proper cleaning and activation of surfaces are required for their heterogeneous integration. In fact, the surfaces of these substrates are one of the most important factors controlling the physical, chemical, electro-optical, and microfluidic

properties of the integrated lab-on-chip, sensing, and medical diagnostic systems. For these new systems, diverse materials including silicon (Si) [5], silicon dioxide (SiO₂) [6], and Pyrex glass [7] are commonly used for the assembly of integrated heterogeneous systems.

The surface properties of these materials, such as wettability, adhesion, morphology and chemical reactivity are critically dependent on the composition of their outermost layer [8]. Also, the surfaces may have impurities, contaminants and process-dependent residues that can alter their properties. In order to examine the materials surfaces and their interaction with other adjacent or contacting surfaces, the ability to analyze surface and sub-surface properties, defects, chemical adsorbents, and particulate contaminants is fundamentally significant. Thus, surface preparation (i.e., treatment/exposure) and analysis is a key step in realizing high-quality bonded interfaces of multiple substrates for electronics, photonics, fluidics and/or mechanical components. Ultimately, surfaces control the wafer bonding and the performance of the systems.

1.2 Direct Wafer Bonding

1.2.1 What is Direct Wafer Bonding?

Wafer direct bonding, also known as “fusion bonding” or “gluing without glue”, is the process of joining two wafers of smooth surfaces at room temperature [9]. Room-temperature bonded wafers usually have weak bonding strength (bonding energy is 10-100 mJ/m²) as compared to covalent or ionic bonding. Heat treatment is, therefore, typically used for increasing the bonding strength. The bonded solid interface can have

three types of surface forces, such as (1) van der Waals attraction forces, (2) electrostatic Coulombic forces, and (3) capillary forces, with additional “very short-ranged forces” resulting from the overlap of the electron clouds [10]. Theoretically, it is possible to bond any solid-state materials regardless of their structural, physical and chemical properties if requirements such as smoothness, flatness and cleanliness of the surfaces are met. The bonding energy of the mating wafer surfaces can be as high as $\sim 1000 \text{ mJ/m}^2$ depending on the nature of the surfaces and treatment methods [5].

Galileo Galilei first reported on the sticking of flat glass plates in 1638 [11]. In 1936, Lord Rayleigh investigated this phenomenon on polished quartz [12]. In 1960s and 1970s, Bueren *et al.*[13] utilized this adhesion process using glass, and Antypas and Edgecumbe [14] used III–V compounds. In 1980s, thick silicon wafers and silicon-on-insulator (SOI) were fabricated by Toshiba [15] and IBM [16] almost at the same time using room temperature adhesion mechanism and an annealing step. Gradually, SOI and other Si-based substrates fabricated by wafer bonding found enormous application in the field of very large scale integration (VLSI), micro/nano-electro-mechanical systems (M/NEMS) [17], and photonic and optoelectronic devices [18]. Also, different wafer bonding methods have been applied to various combinations of materials including silicon [19].

1.2.2 High Temperature Wafer Bonding

1.2.2.1 Hydrophilic Wafer Bonding

Hydrophilic wafer bonding is the most widely used wafer bonding method. It was first demonstrated by Lasky in 1986 [16]. This bonding method strongly relies on the influence of the surface hydroxyl (OH) groups. The term “hydrophilic” refers to the amount of OH groups. In wafer bonding, highly hydrophilic surfaces offer improved chemical affinity through the increased OH groups.

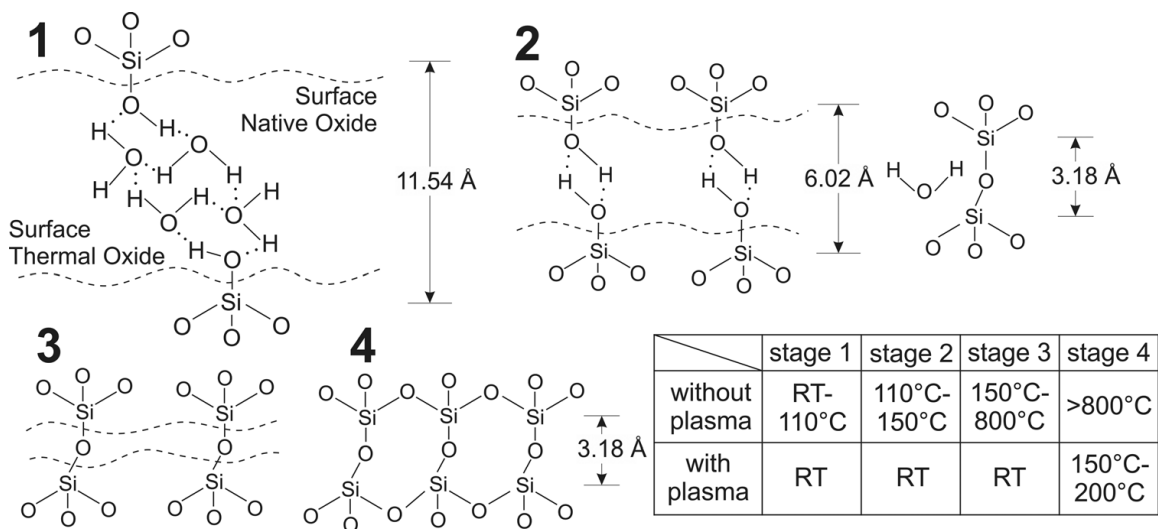


Figure 1-1: Schematics of four different stages at the interface during the annealing of directly bonded wafers [20].

The hydrophilic wafer bonding model was first proposed by Stengl *et al.* [21] based on the chemistry of silica and oxidized silicon. The Si–OH groups on the silica surface construct a three-dimensional hydrogen-bonded water molecule network. The desorption process of the adsorbed water molecules during heating above 180 °C under atmospheric pressure leaves the surface with hydroxylated silica, where the Si–O groups are mostly connected via hydrogen atoms. When two hydrophilic wafer surfaces are contacted, they bond to each other through hydrogen bonds with a low bonding energy of ~1000 mJ/m².

High temperature annealing (i.e., >800 °C without plasma) results in the formation of Si-O-Si bonds (Fig. 1-1) across the interface due to the following chemical reaction [20],



Hydrogen gas is formed across the interface as result of the reaction between water molecules with Si [20],



The product H_2 nucleates the voids at the bonded interface. The high temperature annealing step after bonding is the primary bottleneck of the hydrophilic wafer bonding due to the harmful effects on temperature sensitive structures and components on the wafers. The SiO_2 has lower packing density in which only 43% of its lattice space is occupied. Thus, the low-density interfacial SiO_2 layer accommodates H_2 gas and alleviates void issues at the interface [20].

1.2.2.2 Hydrophobic Wafer Bonding

In contrast to the hydrophilic wafer bonding, hydrophobic wafer bonding relies on the surfaces without OH groups. Hydrophobic surfaces are obtained by removing the native oxide layers using hydrofluoric acid (HF) [22]. The term “hydrophobic” refers to high resistance to water molecules and other chemicals. While Bengtsson and Engström [23] provided detailed analysis of hydrophobic wafer bonding in 1989, Bäcklund *et al.* [24],[25] presented the first concept of hydrophobic wafer bonding by suggesting that the contacting force is due to the van der Waals force and not the hydrogen bonds. However,

Tong *et al.* [26],[27] assumed that the hydrophobic surface forms hydrogen bonds via Si–F groups. This hypothetical model is well accepted by the community of wafer bonding research. In this model, the bonded wafers are annealed at different temperatures. A nearly constant interface energy increases at two different temperature regimes, such as $150\text{ }^{\circ}\text{C} \leq T \leq 300$ and $T \geq 300\text{ }^{\circ}\text{C}$, where the activation energies are characterized as 0.21 eV and 0.36 eV, respectively [22]. The high temperature annealing above $600\text{ }^{\circ}\text{C}$ forms interfacial Si-Si bonds (Fig. 1-2) [28]. Different reaction mechanisms at the interface are responsible for the different activation energies at high temperatures.

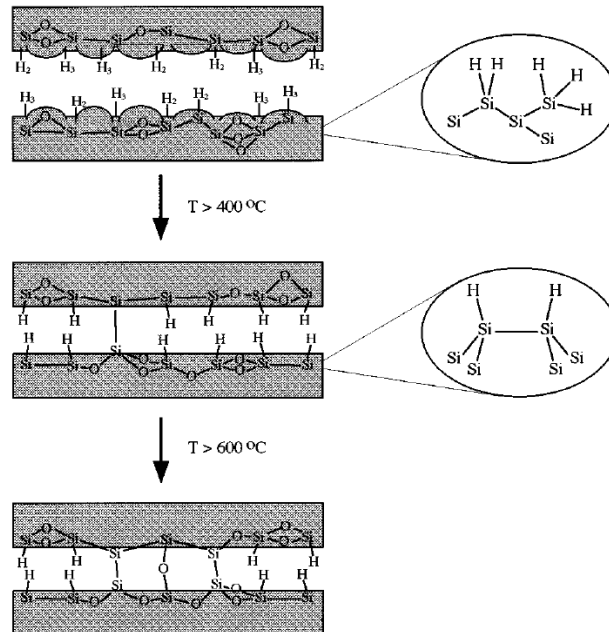


Figure 1-2: Schematic of proposed mechanism for hydrophobic [Si(100)] wafer bonding [28].

1.2.2.3 Anodic Bonding

Some wafers, such as glass, have weak adhesion and coefficient of thermal expansion (CTE) mismatch issues in the hydrophilic and hydrophobic wafer bonding. In order to

address these issues, anodic bonding is proposed using modified impurities in the wafers. Anodic bonding is a direct wafer bonding method, also known as “field-assisted bonding” or “electrostatic sealing” [29] which uses electric fields to bond, for example, Si/glass and metal/glass. A successful anodic bonding requires clean, smooth wafers, a powerful electrostatic field and high alkaline ion concentration in the case of borosilicate glass wafers. Comparable CTE of the mating wafers are also needed for high temperature (250 to 400 °C) anodic bonding with glass wafers [30].

Anodic bonding is useful for hermetic sealing of elements in MEMS devices, which protects the inner components of the device from environmental influences such as humidity and contaminants [31]. However, high temperature anodic bonding suffers from CTE mismatch. Thus, low temperature anodic bonding of RCA cleaned Si and glass was demonstrated [32] with a range from 200 to 300 °C. The oxidation of silicon and cleaning of glass in the hydrophilic treatment resulted in hydrogen bonding between hydroxyl groups of the surfaces.

1.2.3 Low Temperature Wafer Bonding

1.2.3.1 Plasma Activated Wafer Bonding

To increase bond strength, high temperature annealing (>1000 °C) is usually used in the direct wafer bonding that causes some deleterious effects in the bonded wafers [33]. For example, the metallic structures contained on wafers may suffer from interfacial metal diffusion [34]. Also, undesirable changes in the profiling of chemical elements,

Chapter 1. Introduction

temperature-sensitive reactions, and stresses due to CTE mismatch occur in the bonded wafers. To address the challenges in high temperature wafer bonding, a low temperature hydrophilic wafer bonding, known as “plasma-activated wafer bonding (PAWB)”, was demonstrated [10],[35],[36]. In this bonding method, the Si wafers were bonded after their activation (i.e., cleaning) with low-pressure plasma. Kissinger *et al.* suggested that plasma activation is the best hydrophilization method required for low temperature direct wafer bonding [37]. The high bond strength obtained in plasma-activated bonding is attributed to the formation of covalent siloxane (Si-O-Si) bonds at the interface [35]. Formation of this covalent bond becomes possible at room temperature through dissociation of silanol groups due to plasma activation. Also, a high surface reactivity is observed due to the disordered structure of the activated surface [10]. Different types of gases are used for plasma activation such as oxygen, nitrogen, and argon [38],[39],[40].

The influence of plasma activation on wafer surfaces is not completely known due to conflicting results and discrepant processing. For example, Farrens *et al.* [36] proposed that the increased oxidation at the bonding interface is due to the high surface charge induced by plasma activation. However, Amirifeiz *et al.* [35] suggested that the porous surface creates a reservoir for the water molecule. Reactive-ion etching (RIE) and microwave plasma treatment using either oxygen or argon showed high bonding strength with a low-density layer at the interface [41]. The plasma processing parameters in low vacuum - ranging from a power of 40-300 W, a pressure of 10-50 sccm, an activation time of 10-300 s, and a contacting time of several minutes to several days - caused discrepant bonding results.

Surface activation using Ar-beam etching under vacuum at room temperature was also demonstrated with high bond strength for Si/Si and SiO₂/SiO₂ [6]. Increased bonding strength was achieved when plasma activation was combined with anodic bonding of Si and glass [42]. Howlader *et al.*[43] reviewed surface-activation-based nanobonding technology for bonding, packaging, and integration of electronic, fluidic and photonic systems. They first classified nanobonding technology into two broad classifications as follows (Fig. 1-3):

- (1) Nanobonding in ultrahigh vacuum (UHV)
 - (a) Direct adhesion
 - (b) Nano-layers adhesion
- (2) Nanobonding in air
 - (c) Sequential plasma activation
 - (d) Hybrid Adhesion (Sequential Plasma Activation + Electrostatic)

The room temperature direct bonding methods are based on Ar fast atom bombardment (Ar-FAB) in ultra-high vacuum (UHV), and O₂ plasma in low vacuum. In the UHV, bonding of dissimilar materials such as Cu/Cu, Si/GaAs, Si/InP, GaAs/GaP, Si/LiNbO₃, Si/Ge, Ge/glass, etc., were discussed.

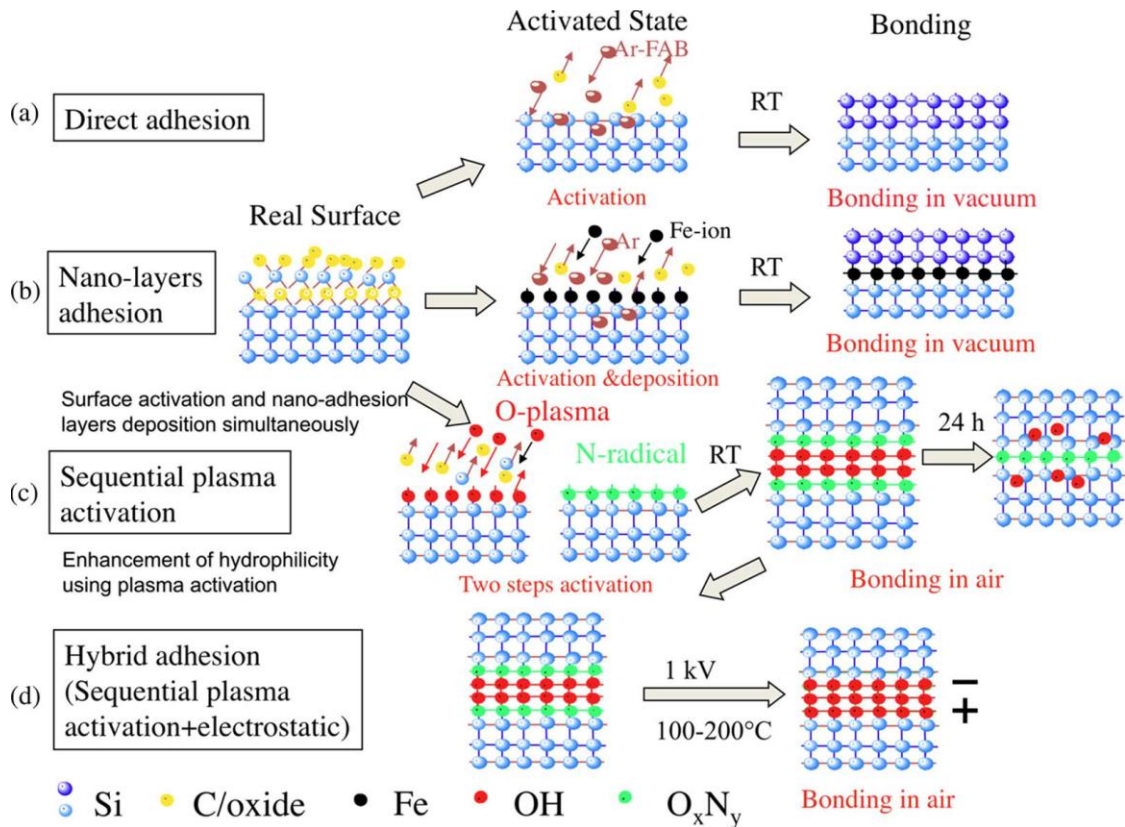


Figure 1-3: Schematic diagram for surface-activation-based nanobonding technologies that provide atomic-level bonding through (a) direct adhesion, (b) nano-layers adhesion, (c) sequential plasma activation, and (d) hybrid adhesion (i.e., the enhancement of adhesion of sequentially plasma-activated surfaces through electrostatic force in anodic bonding) between the mated surfaces. Four types of surface activation have been developed based on the nature of the mated surfaces [43].

This thesis focuses on the low vacuum plasma activated bonding rather than UHV bonding. Low vacuum plasma activated bonding is especially attractive for MEMS applications and 3D interconnects in integrated circuits [44]. All of these applications require low temperature processing and bonding of Si to PECVD oxide layers, highly mismatched materials and polymers. However, the use of moderate temperature annealing in PAWB is harmful for temperature sensitive devices. For example, reduced

bonding strength along with a growing number of interface voids were observed due to heating of plasma activated Si wafers [45]. Thus, a room temperature wafer direct bonding method is necessary to avoid high temperature induced degradation in bond quality.

1.2.3.2 Sequential Plasma Activated Wafer Bonding

Sequential plasma activated bonding (SPAB) is a novel direct bonding method which is a combination of plasma activations made from reactive-ion etching (RIE) plasma and microwave (MW) radical plasma (Fig. 1-3) [46]. The highly reactive and hydrophobic surfaces induced by SPAB offers spontaneous adhesion of mating surfaces at nanometer resolution without the use of intermediate layers, external pressure, and high temperature annealing. SPAB is an attractive solution to the problems related to high temperature annealing that are being utilized in most current wafer bonding techniques. Moreover, thermal expansion mismatch can cause thermal stress and eventually crack the bonded interface. Also, the quality of the bonded interface may degrade through doping profile modification, thread generation, misfit dislocations, and lattice mismatch [47]. On the other hand, SPAB technique requires no thermal processing, thus eliminating the aforementioned bond quality degradation [48].

The two-step SPAB technique requires surface activation using O₂ RIE plasma and N₂ radical plasma, respectively. While O₂ RIE plasma is responsible for the removal of surface oxides, contaminants, and molecules by a physical sputtering process, N₂ radical

plasma is necessary to enhance the surface reactivity [49]. The resulting surface is highly hydrophilic in nature. The contact angle measurement data showed that SPAB makes a more hydrophilic surface than either only O₂ RIE plasma activation or only N₂ MW radical plasma [46]. The bonding strength obtained by SPAB without post-bonding heating was found to be equivalent to bulk fracture strength [45]. Although, different low temperature bonding techniques are being utilized, the influence of surface properties and surface chemical states on bondability is still not fully realized. Thus, in next couple of sections, the influence of surface properties on bondability will be discussed.

Although sequential plasma activation (i.e., O₂ RIE plasma + N₂ MW plasma) is a highly attractive plasma activation process for direct bonding, the most integral step of this method is the physical/chemical sputtering process done by the O₂ RIE plasma. The physical sputtering of oxygen plasma removes particles and contaminants from the surface and deposits a very thin layer of oxides. The activation process also creates a porous surface layer that dramatically enhances the bond strength through absorbing the interfacial gases [38]. Therefore, this thesis focuses on the effect of O₂ RIE plasma on surface properties to identify their effect on bondability. Other advantages of using O₂ RIE plasma include its uses in the majority of wafer bonding techniques and cleaning processes in the microelectronics industry [50].

1.3 Surface Properties in Bonding

1.3.1 Role of Surface Morphology on Wafer Bonding

Although direct wafer bonding is primarily dependent on short-range intermolecular force and interatomic attraction forces, wafer surface morphology plays a significant role in determining bonding strength. The immediate consequence of high surface roughness is a smaller contact area between wafers that may result in interface voids [51]. Even bonding might be totally failed if the surface roughness is higher than that of a critical value, which is approximately 1 nm as reported by Howlader *et al.* [52]. The two parameters that describe surface morphology are surface flatness and roughness. Surface flatness, alternatively termed as total thickness variation (TTV), is determined by the difference in highest and lowest point on a wafer [53]. Surface roughness is expressed as a root mean square (RMS) of surface heights at a microscopic location. A surface-flatness-dependent gap-closing mechanism based on elastomechanics theory was first proposed by Stengl *et al.* [54]. Later, the mechanism was developed further by Tong *et al.* [55] by proposing gap closing conditions, which are dependent on a wafer's lateral extension ($2R$) and thickness (d) as shown in Fig. 1-4. Two cases for closing of gap arise.

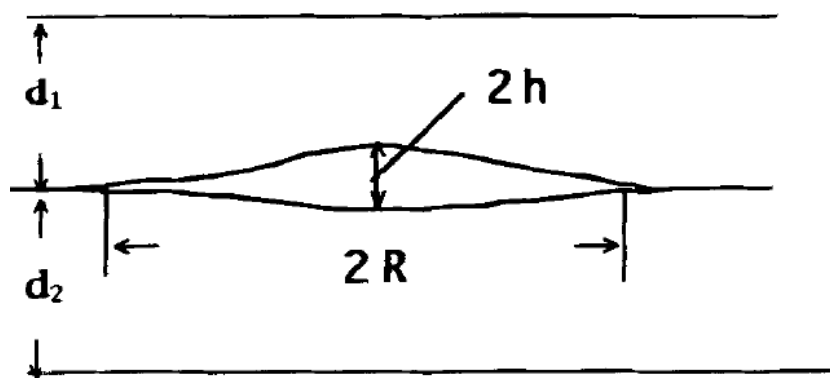


Figure 1-4: Schematic for gaps at the interface between bonded wafers [55].

If $R < 2d$, the gap height (h) becomes independent of wafer thickness d , as shown in the following equation [55],

$$h < 2.6(R\gamma / E)^{1/2} \quad (1.3)$$

E is the Young's modulus, and γ is the surface energy of the bonding pair. Again, for $R > 2d$ the gap-closing becomes dependent on wafer thickness (d), as per the following equation,

$$h = \frac{R^2}{\sqrt{1.2Ed^3 / \gamma}} \quad (1.4)$$

Room temperature wafer-bonding criteria are thus well-explained by gap-closing theory. But the mechanism of real area contact still needs further consideration to find a relation between surface bondability and the random distribution in the topography of the surface. The increased surface roughness of Si wafers with Ar beam etching caused degradation in bonding strength [56]. Also, reduced surface adhesion force was observed with increased surface roughness of silicon wafers under ultra-high vacuum conditions [57]. In another study of transmission laser bonding of Si, SiO₂, and glass wafers, the tensile strength of bonding was decreased almost linearly with increased surface roughness [58]. Gui *et al.* [51] addressed this issue by developing a continuous model of surface-roughness-influenced wafer bonding. The model is based on the theory of Deryagin, Muller, and Toporov (DMT) contact mechanics and a statistical model of surface roughness. They derived a dimensionless surface adhesion parameter (θ) that determines

the real area of contact after wafer bonding at room temperature. The adhesion parameter (θ) is as follows [51]:

$$\theta = \frac{E}{w} \sqrt{\frac{\sigma^3}{R}} \quad (1.5)$$

E is the material elasticity, w is the surface energy of adhesion, σ is the standard deviation of the asperity height (i.e., surface roughness) and R is the radius of elastic sphere. The bonding energy and the real area of contact (A_b) were found to be closely related to each other, which is clearly evident in Fig. 1-5 [51].

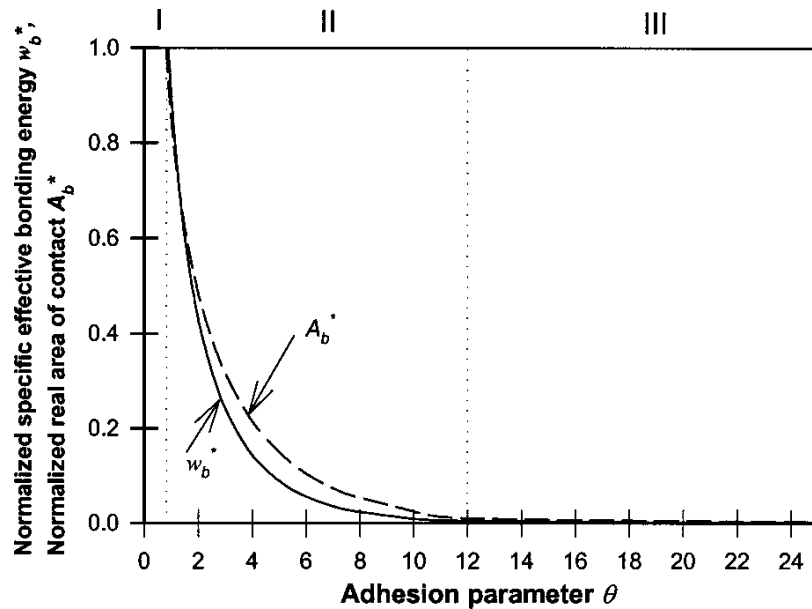


Figure 1-5: Normalized specific effective bonding energy (solid line) and the normalized real area of contact (dashed line) as functions of the surface adhesion parameter [51].

In fact, three regimes are indicated in Fig. 1-5: (I) bonding regime, (II) adherence regime and (III) nonbonding regime depending on the value of adhesion parameter (θ).

Considering equation (1.5), it can be concluded that a higher percentage of the real area of contact and a higher bonding energy are derived from smaller surface roughness, higher specific energy of adhesion, and lower elasticity.

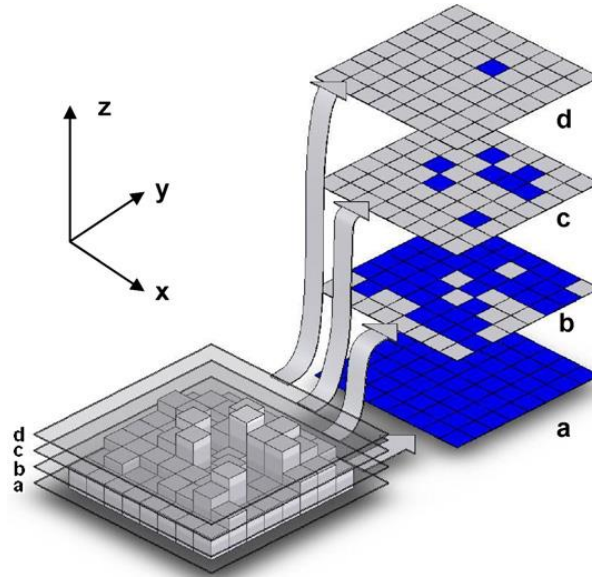


Figure 1-6: Concept of bearing ratio. The darker area represents the bearing area [59].

Miki *et al.* [60] explicitly correlated the bond quality (i.e., bonding energy) with the nanoscale surface morphology by calculating the bearing ratio. Bearing ratio (BR) (shown in Fig. 1-6) is the ratio of the area of a surface lying above a given depth (also known as bearing depth) to the total surface area as expressed in the following equation [60]:

$$BR = \int_0^{z_b} p(z) dz \quad (1.6)$$

z_b is the bearing depth, and $p(z)dz$ is the probability of the surface to have a depth between z and $z + dz$.

To demonstrate the effect of nanoscale surface roughness on bonding energy, two different types of Si wafers were bonded: buffered oxide-etched and KOH-etched wafers. The normalized bonding energy versus bearing ratio at a bearing depth of 1.4 nm showed a linear relationship between them. Thus bearing ratio was considered a good predictor for bond quality. In another study, low-temperature wafer bonding of Si using ultraviolet (UV) light activation showed that bearing ratio analysis of surface roughness is a more appropriate approach for characterizing surface roughness and bonding process optimization [59].

1.3.2 Role of Surface Hydrophilicity on Bonding

Surface hydrophilicity or wetting property is considered to be an important parameter for direct wafer bonding of dissimilar materials. The hydrophilic/hydrophobic nature of the bonding surface can be modified by exposing surfaces in different ambiances such as O₂ and N₂ plasma [61],[62], wet chemical treatment [63], and high relative humidity containing OH groups [27]. The most common technique of measuring hydrophilicity is the measurement of contact angle. Different techniques are available for contact angle measurement (Fig. 1-7). Generally, the contact angle of a droplet of water on a solid surface is measured. If the volume of the droplet of water is too small, measuring the contact angle might be difficult due to water evaporation. Thus, inverted bubble

technique can also be utilized, where the contact angle of an air bubble in deionized water which contacts with the treated surface is measured [63].

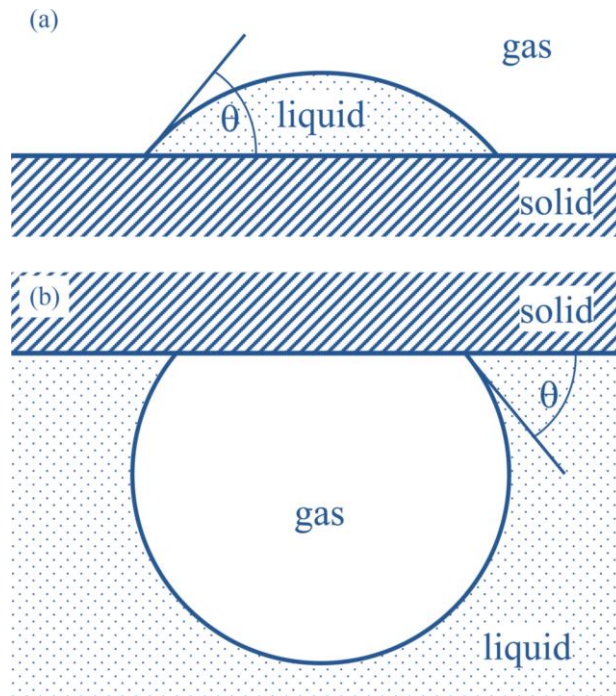


Figure 1-7: Contact angle of (a) a drop of water on a surface, (b) an inverted bubble at a surface in a liquid [64].

Contact angle measurement is critical in systems integration to identify the hydrophilicity of bonding surfaces. For example, a highly hydrophilic Ge wafer surface was obtained by O_2 plasma activation for only 10 s [65],[66]. Kissinger *et al.* showed that hydrophobic Si wafer requires pretreatment, such as RCA cleaning and plasma activation before bonding [37]. A high relative humidity environment which contains a high amount of OH groups resulted in either lower contact angle or higher hydrophilicity in Si-based wafer bonding [27]. In another study, contact angle measurements of plasma-immersion ion-implanted

(PIII) silicon wafers with nitrogen and carbon showed increased reliability for high-temperature microelectronics [67]. Also, argon (Ar) and H₂O plasma-treated SiO₂ films and their aging behavior were investigated by measuring the surface charge and contact angle (i.e., surface reactivity) [68]. Higher compositional stability was observed in H₂O plasma treatment than that of Ar plasma. In a study of passive microfluidic valve fabrication, SiO₂/glass hydrophobic (contact angle ~102°) micro-channels were made by utilizing a self-assembled monolayer of octadecyltrichlorosilane and plasma-deposited CHF₃ patterns [69].

1.3.3 Role of Surface Mechanical Properties on Bonding

Surface mechanical properties of Si based wafers in direct bonding is becoming increasingly important in today's mainstream Silicon-on-Insulator (SOI) and MEMS technology. These properties are analyzed by measuring surface hardness and modulus of elasticity by nanoindentation hardness tests [70] and fracture toughness and bending tests [71]. The study of nanomechanical properties of thin SOI made by wafer bonding and SMART CUT™ was compared with bulk Si. The nanoindentation test results of the standard and strained SOI showed that thin bonded Si films exhibit considerably lower hardness and modulus of elasticity than that of bulk single crystal Si [72]. Also, reliability of MEMS/NEMS depends upon the mechanical properties of micro/nanoscale structures. In the comparative micro/nanomechanical characterization of single-crystal Si, SiO₂, SiC, Ni-P and Au, scratch and indentation tests showed that SiC has higher hardness, elastic modulus, and resistance than other materials [71].

Materials with varying hardness and elastic modulus are employed to design highly reliable MEMS devices that can withstand friction, wear and other failure mechanisms [73]. Tuning of mechanical properties, such as gradient residual stress, was also done by using NH_3 , O_2 , and H_2 plasma [74]. Although the tuning of mechanical properties has potential application in controlling the shape and resonant frequencies of micromachined beams in MEMS devices, the influence of mechanical properties (e.g., surface hardness) on bondability is not fully realized. In fact, wafer bonding is an important step in the MEMS fabrication in which wafers are exposed in different ambiances. Also, surface hardness could be a critical parameter in the direct wafer bonding where applied bonding forces have significant influence on the mechanical properties (e.g., elasticity, stress, strain, crack propagation etc.) of the narrow area of bonding surfaces and interfaces. Finally, the hardness of the materials may be used to forecast mechanical fracture and fatigue-related reliability of MEMS devices for pressure-sensing, micro-pumping, and switching [73].

1.4 Surface Chemical State in Bonding

The elemental and compositional state of material surfaces plays a major role in determining the hydrophilicity (OH groups)/hydrophobicity (H groups) and other physical/chemical properties of the direct wafer bonding of Si/Si, Si/SiO₂, Si/glass [65],[75],[33]. For example, the O₂ RIE plasma treatment of Si, SiO₂ and glass surfaces plays an important role in their hydrophilic wafer bonding. Also, the hydrophilic Si surfaces at relative humidity of 50% or greater contain more than one monolayer of OH

group termination [27]. The hydrogen bonding between adsorbed water molecules on the two surfaces makes the Si—OH···OH—Si in Si wafer bonding [27]. Thus, a versatile chemical state analysis technique, such as X-ray photoelectron spectroscopy (XPS) is needed to study the elemental compositions and chemicals states of materials surfaces.

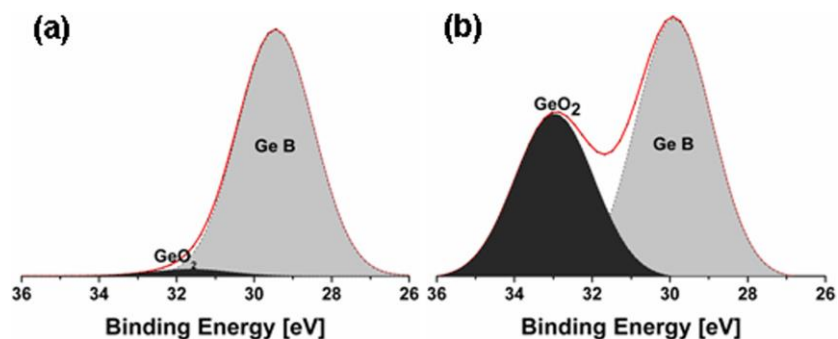


Figure 1-8: XPS spectrum of the Ge (Germanium) 3d core level of de-bonded Ge surface at post-bonding and post two step annealing: (a) cleaned in an SC1-equivalent solution (reference sample) and (b) for sample with SC1-equivalent clean followed by O₂ radical 10 min exposure prior to bonding [76].

An XPS study of Si surface chemistry in the form of adsorbents, catalysts and thin films was reported [77]. It was shown that the binding energy shift in ambient-humidity-exposed Si is due to different chemical groups. In another study of an oxygen radical plasma-activated Si/Ge-bonded interface showed that the oxygen radical plasma-activated Ge surface had higher O/Ge ratio (Fig. 1-8) than that of untreated Ge surface through interfacial hydrophilic reaction [76]. The resulting GeO₂ contributed to the decrease of process-induced deformation. Other XPS studies of Si included oxide layer thickness in oxygen plasma-activated surfaces [36], oxidized Si with ion-implanted oxygen [78], contaminants (C_{1s} peak) and oxides (O_{1s} peak) in hydrogen plasma-treated

polycrystalline Si [79], and high oxygen-to-silicon ratio in oxygen plasma-treated Si generated by electron cyclotron resonance [80].

An XPS analysis of SiO₂ investigated the compositional stability of native SiO₂ and SiO₂ thin films after plasma treatments and different types of aging in humidity [68]. It was reported that SiO₂ thin films fabricated by hexamethyl-siloxane/O₂ plasma were less sensitive to aging effects. Other XPS studies of SiO₂ included a crystal orientation-dependent chemical shift due to distribution of electric dipole moment at the interface of ultra-thin silicon oxide [81], and different oxidation states of Si⁰⁺, Si¹⁺, Si²⁺, Si³⁺ and Si⁴⁺ after plasma anodization and rapid thermal annealing of Si (Fig. 1-9) [82].

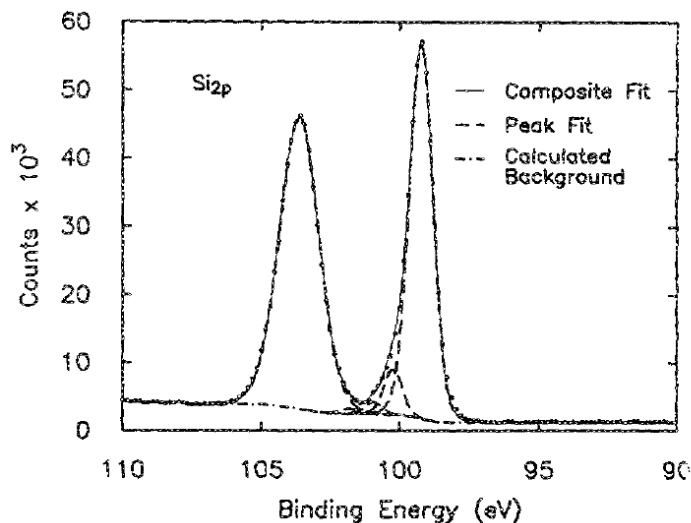


Figure 1-9: Photoelectron spectrum of Si_{2p} regions, dots, with individual peak fits for each of the five oxidation states of silicon (Si⁰⁺, Si¹⁺, Si²⁺, Si³⁺ and Si⁴⁺) and the composite fit formed by the sum of those individual fits [82].

A literature survey of glass XPS analyses shows a wide range of investigations. For example, an XPS study of sodium silicate glass that analyzed the O_{1s} spectra indicated an

increase in the ratio of non-bonding oxygen due to increase of iron concentration (Fig. 1-10) [83]. In another XPS study of silane-treated microscope glass slide surfaces showed the presence of Si-CH bond (different from the Si-O bond) [84]. Also, drifting of oxygen from the Pyrex glass toward Si in Si/Pyrex glass laser bonding was reported, which controlled the bond strength [85],[86]. Moreover, the O_{1s} XPS spectra of silica and soda lime glasses at room temperature and humidity (RH:64%) revealed that the nanoindentation hardness was dependent on the ratio of cuprous (Cu^+) and cupric (Cu^{2+}) ions [87].

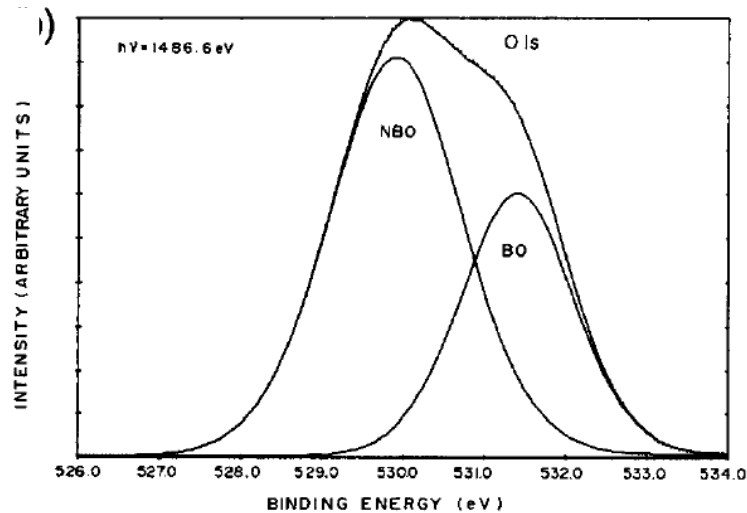


Figure 1-10: O_{1s} spectrum for the $x = 0.085$ glass $[(SiO_2)_{0.7-x}(Na_2O)_{0.3}(Fe_2O_3)_x]$ composition. The points are the experimental data while the fitted components and their sums are represented by the continuous lines [83].

The majority of XPS studies on plasma processing parameters of wafers are not directly related to the bonding and packaging of microelectronic, MEMS and microfluidic devices. A literature survey showed that plasma power critically impacts the formation of

Chapter 1. Introduction

OH and H ranges from 10-300 W with the activation time of up to 300 s and chamber pressure of up to 100 Pa [35],[88],[38]. Recently, surface-activated bonding of Si, SiO₂, and glass treated by O₂ RIE were investigated without the elemental and compositional analysis [46],[89],[90]. In all the cases of bonding, the bonding strength was mainly characterized, rather than the chemical state of Si, SiO₂ and glass after their surface treatments. Also, bonding of such materials for mass production may go through different ambient humidity conditions which may influence their bondability [91]. Thus, an analysis of the chemical states and elemental compositions of the treated surfaces (with short and long activation times) is required in order to identify the role of plasma and ambient humidity conditions on the surfaces.

1.5 Contributions

From this study, we have submitted two articles to peer-reviewed journals. The first one [92] is on the effect of oxygen plasma and humidity on surface roughness, contact angle, and hardness of Si, SiO₂, and glass for direct wafer bonding. The second one [93] is on the surface chemical analysis of Si, SiO₂, and glass due to their exposure in oxygen plasma and humidity for direct wafer bonding. I was primarily responsible for conducting the experiments, literature search, and manuscript writing for the articles.

1.6 Objectives and Outline of the Thesis

The objectives of this thesis are to investigate the influence of oxygen plasma and humidity exposure on the surface properties of Si, SiO₂, and glass surfaces that ultimately

controls their direct bonding for microelectronic, lab-on-a-chip, and MEMS applications. The surface morphology, hydrophilicity, hardness, and surface chemical states of Si, SiO₂, and glass have been investigated as functions of O₂ plasma activation time and storage in ambient humidity to understand the role of plasma and humidity on bondability.

This thesis consists of five chapters. Chapter 1 presents the importance of surface analysis, the fundamentals and historical background of wafer bonding, and the role of different surface properties on direct wafer bonding. The last part of Chapter 1 concludes with the motivations and objectives of this study.

Chapter 2 concentrates on the fundamental principles and relevant experimental aspects of the characterization of different surface properties.

Chapter 3 describes the experimental results on the influence of plasma activation time, storage in ambient humidity on the surface roughness, contact angle and hardness of Si, SiO₂, and glass, and discusses their role in bondability.

Chapter 4 demonstrates the experimental results regarding the effect of oxygen plasma and humidity on the surface chemical states of Si, SiO₂, and glass to investigate the chemical mechanisms for direct wafer bondability.

Finally, Chapter 5 concludes with the overall findings in surface analysis for direct wafer bonding and proposes future work.

CHAPTER 2.

EXPERIMENTAL PROCEDURES

2.1 Specimen preparation

Three types of wafers were used for the surface analysis: (i) p-type Si(100) wafers with one-side mirror polish and 450 μm thickness; (ii) SiO₂-on-Si wafers with 50 nm thick thermal oxides; and (iii) glass (Pyrex, from SCHOTT, US) wafers. The glass wafers might have contained alkaline elements similar to the standard Pyrex glass. The wafers were cut into 10×10 mm² pieces. For, Si, SiO₂, and glass wafers, first the surfaces were activated using oxygen reactive-ion etching (O₂ RIE) plasma for different times such as, 60, 150, 300, 600 and 1200 s. The as-received and plasma-activated wafers were then analyzed by a Drop Shape Analyzer (DSA 100), an Atomic Force Microscope (AFM), an

Ultra-micro Hardness tester (DUH-211S), and by X-ray Photoelectron Spectroscopy (XPS) to measure surface hydrophilicity, roughness, hardness, and chemical states, respectively.

Table 2-1: Description of the materials, their surface activation and storage conditions with their corresponding acronyms.

Acronyms	Surface Activation	Storage Conditions	Materials
Si:O₂RIE	O ₂ RIE plasma	No storage	Si
Si:O₂RIE+20RH	O ₂ RIE plasma	20 days of storage in 98% RH and 15 °C temperature	Si
Si:O₂RIE:20D+20RH	O ₂ RIE plasma	20 days of storage in class 1000 cleanroom ambient humidity and 20 days in 98% RH and 15 °C temperature	Si
SiO₂:O₂RIE	O ₂ RIE plasma	No storage	SiO ₂
SiO₂:O₂RIE+20RH	O ₂ RIE plasma	20 days of storage in 98% RH and 15 °C temperature	SiO ₂
SiO₂:O₂RIE+20D+20RH	O ₂ RIE plasma	20 days of storage in class 1000 cleanroom ambience and 20 days in 98% RH and 15 °C temperature	SiO ₂
Glass:O₂RIE	O ₂ RIE plasma	No storage	Glass

A second set of plasma-activated Si and SiO₂ surfaces were analyzed using the aforementioned techniques after storage in a humidity chamber at a constant temperature of 15 °C and constant humidity of 98% relative humidity (RH) for 20 days. A third set of plasma-activated Si and SiO₂ surfaces were analyzed after storage in clean room (class 1000) ambience (i.e., 23 °C and 45% RH) for 20 days as well as 20 days of storage in humidity chamber (i.e., 15 °C temperature and 98% RH). No additional cleaning or

treatments were done before the plasma activation of the wafers. The following sections will discuss the tools used for plasma activation, humidity storage, and surface analysis. In order to express the different sets of wafers with/without activation and storage conditions, the acronyms given in Table 2-1 will be used throughout the thesis.

2.2 Hybrid Plasma Bonder

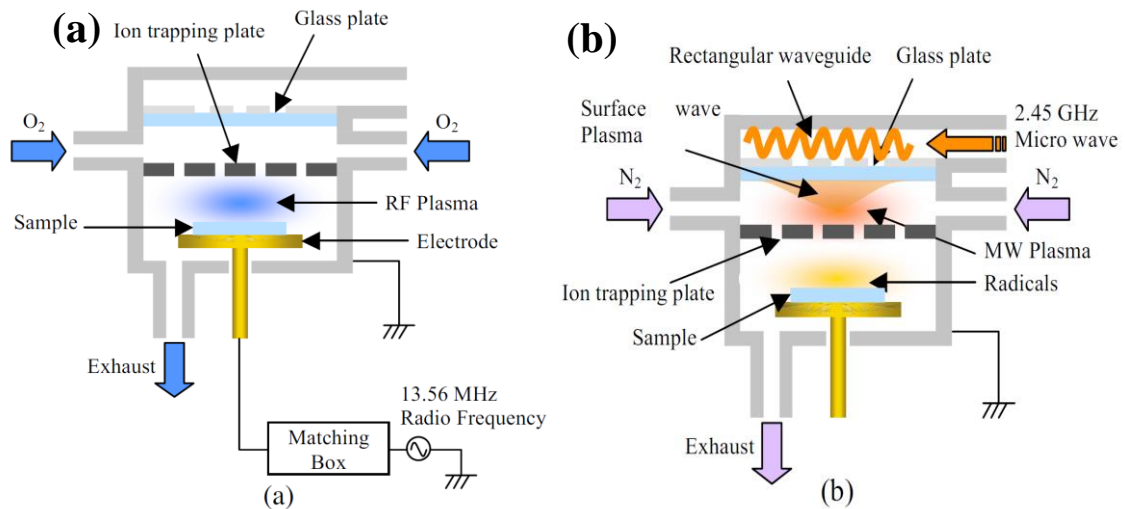


Figure 2-1: Schematic diagrams for SPAB process consisting of (a) O_2 RIE plasma system with self-biased condition and (b) N_2 MW radical plasma [45].

The surface activation of Si, SiO_2 , and glass wafers was accomplished using a Hybrid Plasma Bonding (HPB) system as shown in Fig. 2-1. Fig. 2-1 (a) shows the HPB operation in RIE plasma mode and Fig. 2-1 (b) shows the operation in MW plasma mode. The HPB consists of two chambers: a plasma activation chamber and an anodic bonding chamber (the anodic chamber is not shown in the Fig. 2-1). Wafers as big as 200 mm can be accommodated in the HPB chamber. The top and bottom parts of the plasma

activation chamber contain the RIE plasma- (13.56 MHz) and microwave plasma- (2.45 GHz) generating equipment separated by an ion-trapping grounded metallic plate. The wafers are placed on the RF electrode for plasma activation.

The discharge between the RF electrode and the metallic plate creates the RIE plasma. A rectangular metal waveguide coupled with a quartz circular glass guides the MW to radiate MW plasma inside the top compartment [45]. There are 1 mm-sized holes in the metallic plate which trap charged ions to produce neutral radicals at the bottom compartment. Oxygen is used for RIE plasma generation, whereas nitrogen is used for neutral radical plasma. The anodic chamber consists of high voltage electrodes and heaters (200 ° C) in bonding heads. Irrespective of temperatures, the applied DC voltage and the time for the anodic bonding are constantly held at 1 kV and 10 min, respectively.

In this study, the O₂ RIE plasma was produced in a chamber background pressure of 10 Pa at 13.85 MHz radio frequency in the HPB. The plasma power was 300 W and the pressure during plasma glow was 200 Pa.

2.3 Atomic Force Microscopy

The sub-nanometer scale morphology of Si, SiO₂, and Pyrex glass surfaces with or without O₂ RIE plasma activation at different storage conditions was measured using Atomic Force Microscopy (AFM). The Dimension Icon Atomic Force Microscope, made by the Bruker Corporation, was used for the measurement. A Si RTSPA tip was used in standard tapping mode with a scan area of 2×2 μm².

Chapter 2. Experimental Procedures

A three-dimensional surface profile is evaluated by measuring the forces (<10 nm) between the probe (mounted on the cantilever tip) and the surface with a very short tip-sample separation (0.2-10 nm). While the tip softly touches/oscillates above the surface with a raster scan, the interacting force is recorded. Thus, there are three primary imaging modes in AFM: contact AFM, intermittent contact or tapping-mode AFM, and non-contact AFM [94]. Contact AFM is a faster approach that utilizes the spring constant of the cantilever to image the sample surface, but this method can damage soft and delicate samples. On the other hand, non-contact AFM has lower resolution and the probe is easily influenced by the contaminants. It utilizes the oscillations of cantilevers above the sample surface monitored by a feedback loop.

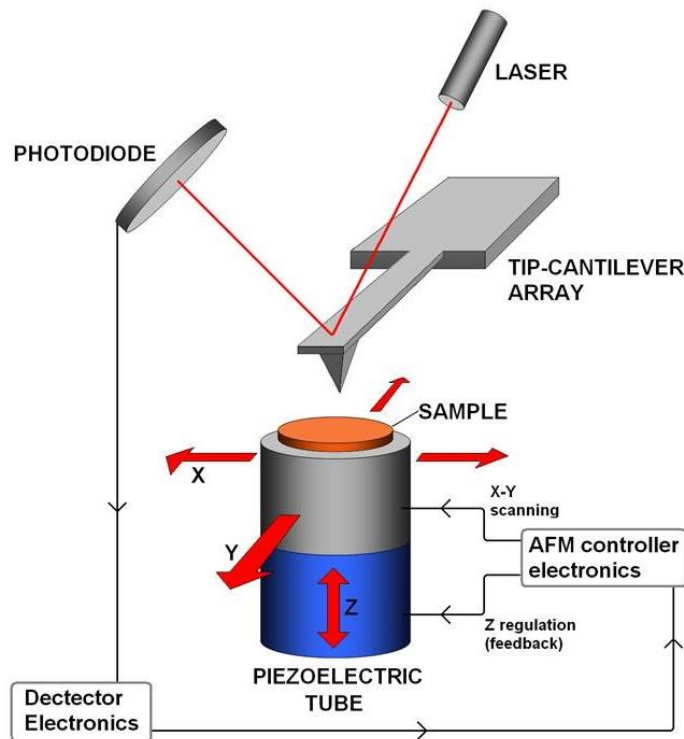


Figure 2-2: Working Principles of AFM [95]

Tapping-mode AFM is a mixed approach that allows high resolution imaging of sensitive surfaces using slower scan speeds, but it is difficult to use for imaging liquids. Thus, tapping-mode AFM has been used in this study as an optimum solution, since it entails less damage, more resolution, and lower scan speed. The schematic of the principle of operation of tapping-mode AFM is shown in Fig. 2-2 [95]. The probe taps the surface with a resonant frequency governed by a drive signal (Fig. 2-2). The relative change in the cantilever oscillation amplitude and phase is transduced as the reflection of a laser light from the cantilever back surface with a photodetector, depicted as the detector signal in Fig. 2-2. The probe moves over the specimen surface using a feedback loop and piezoelectric scanners. The feedback loop maintains the RMS amplitude set-point of the oscillation by adjusting the Z position of the scanner [94]. The adjusted Z position at each point during the (x,y) raster scan is used by the computer software to generate topographic image of the specimen surface. The resolution of the scanner in x-, y-, and z-directions is on the scale of sub-angstroms. The Z position of the surface is then used to calculate the root-mean-square (RMS) surface roughness (R_q) as shown by the following equation [96]:

$$R_q = \sqrt{\sum_{n=1}^N \frac{(Z_n - \bar{Z})^2}{N}} \quad (2.2)$$

Chapter 2. Experimental Procedures

N is the number of points in the specimen surface, Z_n is the height of the surface at each point, and \bar{Z} is the mean value of the surface height. The value of surface roughness may vary depending on the AFM mode, scan resolution, and total scanning area of the surface.

In this study, the surface roughness was measured by using Si RTSPA tip in standard tapping mode with scan area of $2 \times 2 \mu\text{m}^2$. The surface roughness (R_q) was measured using the root mean square (RMS) method.

2.4 Drop Shape Analysis

It has already been discussed that surface hydrophilicity/hydrophobicity and the surface reactivity of any materials surface are important parameters for the processing and bonding of MEMS devices. These parameters can be obtained by analyzing the water drop shape on the surface of the materials. The contact angle depends on the surface and interfacial tensions. The interrelationship between these tensions was formulated by Young. Young considered a 3-phase contact line point (Fig. 2-3) and gave the following equation:

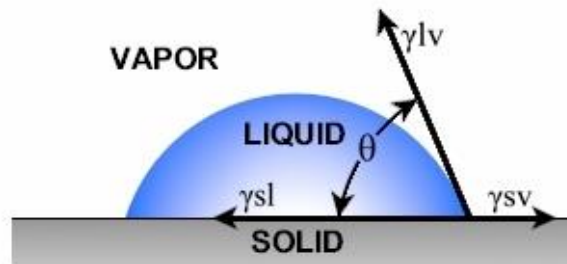
$$\gamma^{sv} = \gamma^{sl} + \gamma^{lv} \cdot \cos \theta \quad (2.1)$$

γ^{sv} and γ^{lv} correspond to the surface tension component of a solid and a liquid, respectively, and γ^{sl} corresponds to the interfacial tension between a solid and a liquid. The contact angle of any hydrophilic surface is usually much lower than 45° , whereas hydrophobic surfaces have a much higher contact angle than 45° [97].

There are two ways of measuring the contact angle: static and dynamic. Static contact angles are measured without changing the size of the drop; dynamic contact angles are measured by increasing or decreasing the volume of the drop. In this study, the static contact angle was measured at an interval of two minutes. The variation of the static contact angle with elapsed time was considered to describe the surface reactivity. The primary reasons for the variation in the contact angle could be the evaporation of liquid, migration of surfactants to the liquid from the solid, and the chemical reactions between the liquid and the solid surface [98]. Therefore, the higher the variation, the more likely the surface will be reactive.

Young's Equation

$$\gamma^{sv} = \gamma^{sl} + \gamma^{lv} \cos\theta$$



θ is the contact angle

γ^{sl} is the solid/liquid interfacial free energy

γ^{sv} is the solid surface free energy

γ^{lv} is the liquid surface free energy

Figure 2-3: The formation of Contact angle on a solid surface proposed by Young [99].

Chapter 2. Experimental Procedures

The calculation of the contact angle is based on the image, which consists of the drop shape and the contact line or base line taken by the instrument camera. The drop shape derived from the image pixel is then adapted to a mathematical model to calculate the contact angle. According to the mathematical model used, different methods of calculating contact angle are utilized such as Tangent method 1, Tangent method 2, Height-weight method, Circle-fitting method, and Young-Laplace (sessile drop fitting) method. In this study, the Drop Shape Analysis system (Model: DSA 100) by Krüss was used to calculate the contact angle of a DI water droplet by utilizing the sessile drop method. This instrument is capable of calculating a minimum contact angle of 2° [98]. Although sessile drop method is the most complicated, it is theoretically the most exact method to calculate the contact angle. The complete drop contour assessed by this method accounts for the interfacial effects as well as the weight of the liquid. The contact angle is then determined by the slope of the contour line at the 3-phase point [98].

In this study, water contact angle was measured with $6\ \mu\text{l}$ de-ionized (DI) water droplet. The contact angle measurement of the first set of wafers after O_2 RIE activation were delayed for approximately 3 minutes due to transfer of specimens from HPB to DSA100 workstation. The sessile drop method was used for the contact angle measurements.

2.5 Nanoindentation Hardness

Nanoindentation hardness tests are the most common means of evaluating mechanical properties of materials surfaces. In such a test, an indenter is pressed against the surface

by using an increasing electromagnetic force at a constant speed from a minimum to a maximum preset test force (Fig. 2-4) [100]. By measuring the changes that occur on the specimen surface, a wide variety of data including hardness and plastic and elastic deformations can be obtained.

In this study, the Dynamic Ultra-micro Hardness Tester (Model: DUH-211S) from Shimadzu was used with a triangular pyramid indenter (tip angle of 115°). Depending on the type of indenter and the use of diagonal length (d_1 & d_2) or indentation depth (h) data, there are several types of hardnesses that can be measured, including dynamic hardness and Martens' hardness. Martens' hardness was measured in this study since it is an ISO standard (ISO14577-1). The Martens' hardness is calculated from the applied test force and the indentation depth while increasing the test force using the following formula [101]:

$$HM = \frac{1000 F}{26.43 \times h^2} [\text{Unit : } N / \text{mm}^2] \quad (2.3)$$

F = applied test force (mN), and h = indentation depth (μm).

The DUH-211S is capable of conducting different types of tests such as load-unload test, cycle test, depth-setting test, step load test and step load-unload test as shown in Fig. 2-5. However, only two types of tests were conducted for hardness measurements: load-unload test and cycle test. In load-unload test mode, the indenter force is increased to a preset maximum force, holds the test force for a specified time, and then unloads the

indenter (Fig. 2-5b). Cycle test indentation experiment actually consists of multiple load-unload tests on the same spot of the surface (Fig. 2-5c). The preset maximum test force for both load-unload test and cycle test was 10 mN. In cycle tests, the total numbers of cycles were 5.

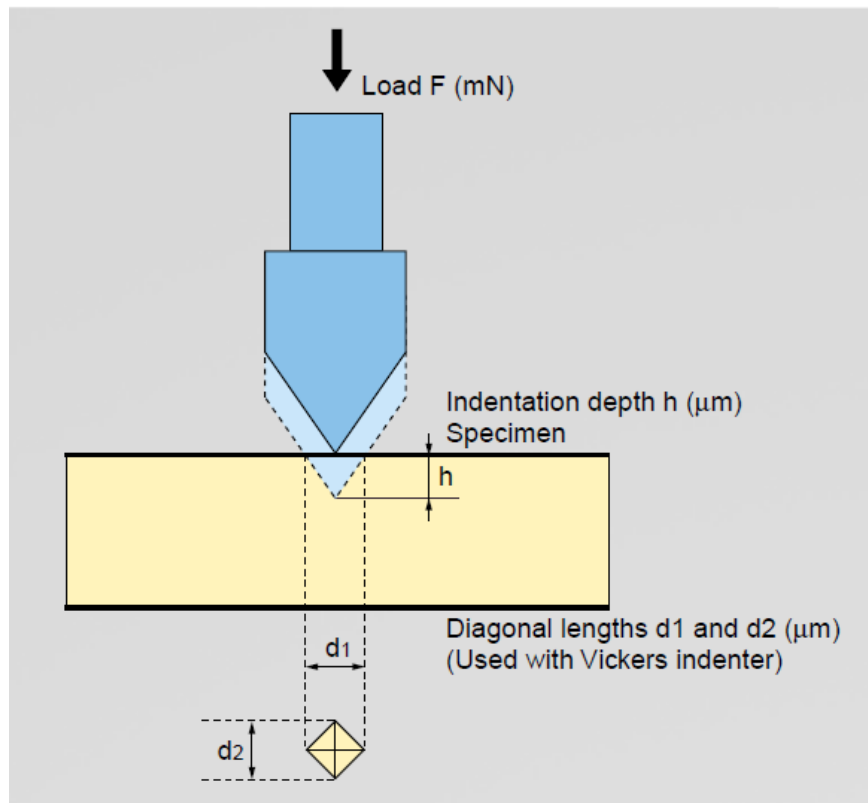


Figure 2-4: Measurement principle of Nanoindentation hardness test [100].

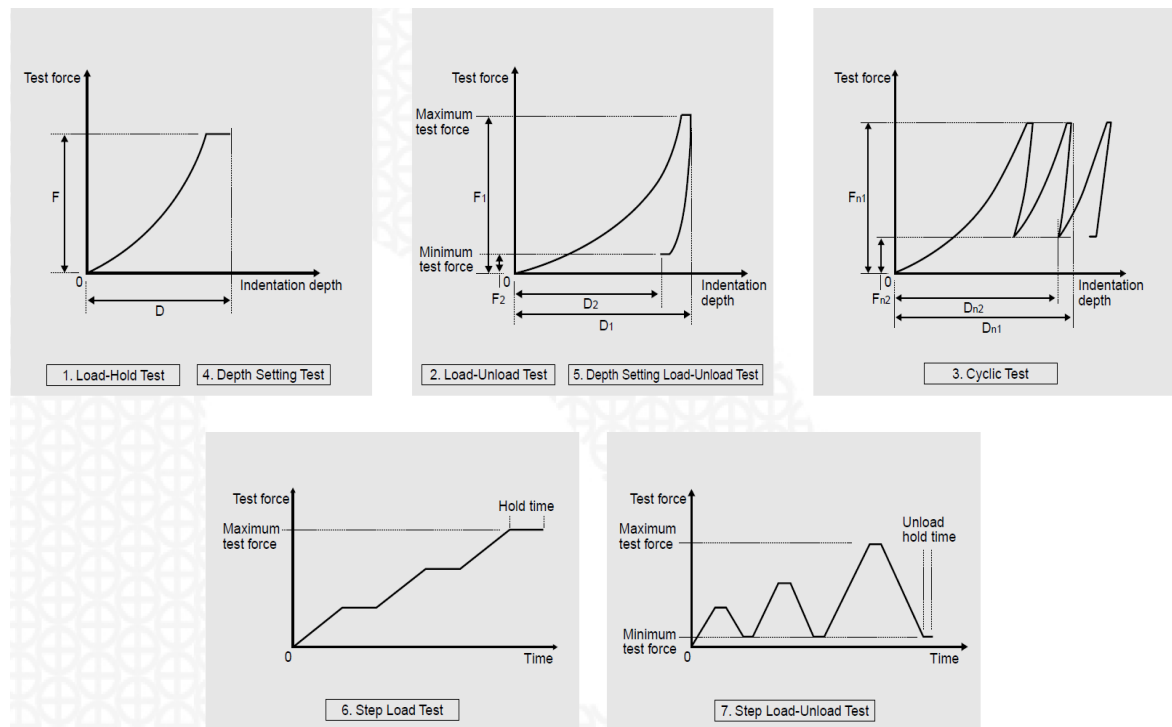


Figure 2-5: Different types of indentation tests [101].

2.6 X-ray Photoelectron Spectroscopy

The chemical state of the materials surfaces was analyzed using the JPS-9200 X-ray Photoelectron Spectroscopy (XPS) instrument from JEOL Ltd. The specimen is irradiated with magnesium (Mg) or aluminum (Al) X-rays to excite photoelectrons, and the energy of the emitted photoelectrons is then analyzed to measure the binding energies of the constituent atoms on the specimen. This analysis is alternately known as Electron Spectroscopy for Chemical Analysis (ESCA). Because of the large interactions between

Chapter 2. Experimental Procedures

photoelectrons and the specimen surface, it can analyze only a few nanometers deeper into the specimen surface region [102].

XPS provides information about the electronic levels of atoms and molecules. Thus, it gives not only the composition of elements, but also the chemical state of atoms and molecules [102]. The XPS is based on the photoelectric effect. When a specimen is irradiated with electromagnetic waves such as ultraviolet rays or X-rays, electron emission (i.e., photoelectron) occurs due to the photoelectric effect. A three-stage process is involved in photoelectron emission: (i) X-ray absorption in the specimen causing photoelectrons to escape from atoms; (ii) reaching of photoelectrons to the surface; and (iii) emission of photoelectrons from the surface. The first stage is responsible for the characteristic XPS.

Principal spectroanalytic processes are shown in Fig. 2-6. Among these four processes, (A) and (B) are the primary processes, and (C) and (D) are the secondary processes. In primary processes, atoms are excited and ionized from their ground state. For example, infrared absorption analysis utilizes the light excitation in process (A). Process (B) is used in XPS. In secondary processes, the excited or ionized atoms again return to ground state. This is used in emission spectrochemical analysis, X-ray fluorescence analysis, and auger electron spectroscopy. The law of energy conservation holds between the incident X-rays and the photoelectron energy as the following equation:

$$E_{kin} = h\nu - E_B - e\phi$$

$h\nu$ is the incident X-ray energy, E_{kin} is the kinetic energy of the photoelectrons, E_B is the binding energy of inner-shell electrons, and e_ϕ is the work function.

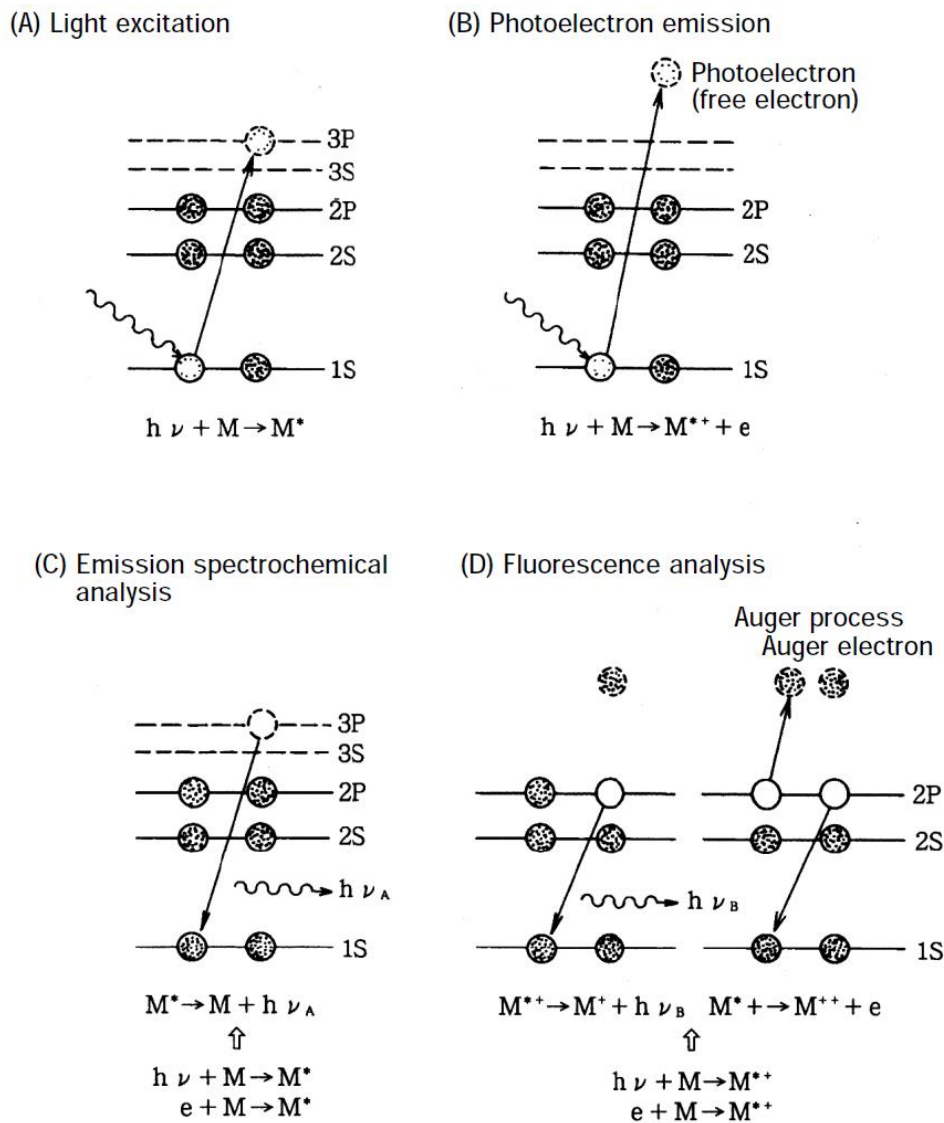


Figure 2-6: Spectroanalysis processes [102].

Chapter 2. Experimental Procedures

Since $h\nu$ and e_ϕ are constant, the binding energy of the inner-shell electrons of atoms determines the kinetic energy of the photoelectrons. In other word, binding energy represents the electronic energy level in an atom and is unique to each element. Thus, an element can be identified by simply measuring the kinetic energy of its photoelectrons. The inner-shell electron binding energy can be changed due to the rearrangement of the outermost electrons as a result of a chemical bond. This change is known as the chemical shift. The chemical shifts can be observed as a change of 0 to several eV. The energies of the chemical bonds can also be estimated by measuring their chemical shifts.

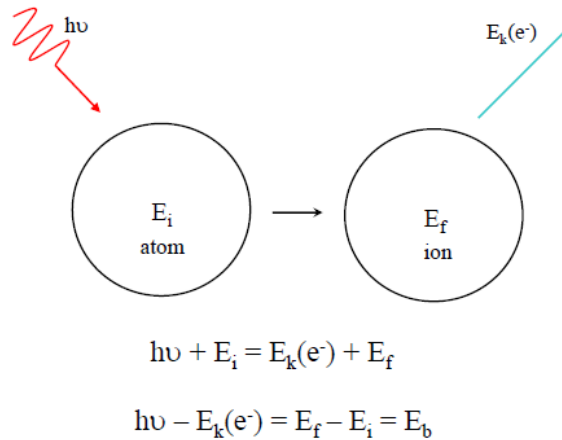


Figure 2-7: Principles of X-ray Photoelectron Spectroscopy [103].

Fig. 2-7 depicts a typical photoemission process. Before photoemission, the systems' total energy is the sum of the X-ray photon ($h\nu$) energy and the initial energy of the target atom (E_i). After photoemission, the total energy of the system consists of the kinetic energy of the photoelectron ($E_k(e^-)$) and the energy of the ionized atom in its final state (E_f). Comparison of the Einstein equation with the equated total energies before and after

photoemission gives the binding energy (E_b) of the electronic orbital. It is evident that E_b is the difference between the final state and initial state energies of the analyzing specimen atom, i.e., $E_f - E_i$. For a specific electronic orbital of an atom, the specific characteristic binding energy peak can be found in the XPS spectra [103].

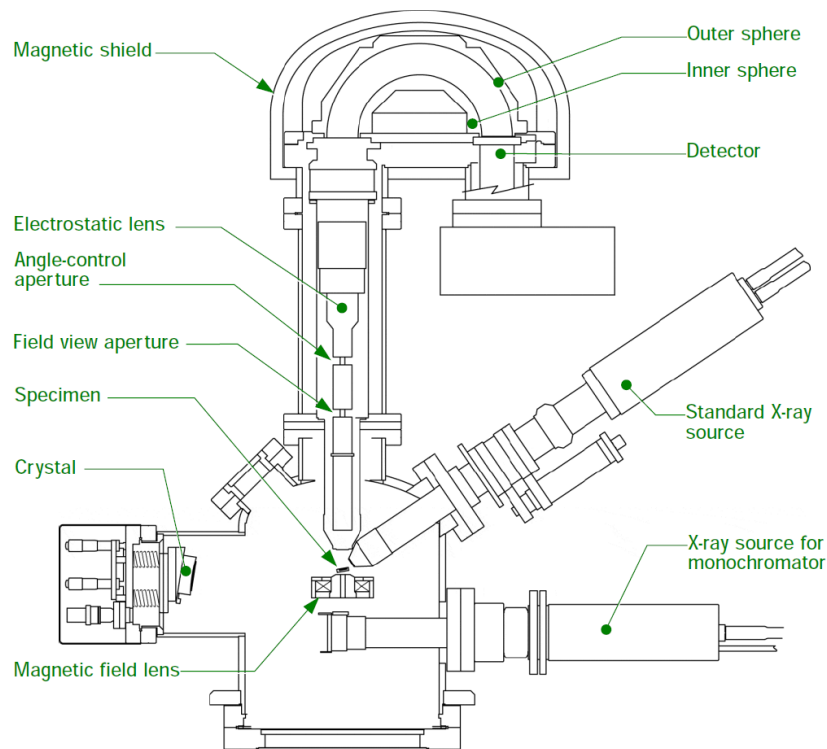


Figure 2-8: Cross section of the XPS analysis chamber (JEOL-JPS 9200) [102].

Fig. 2-8 shows the cross-sectional diagram of the JEOL JPS-9200 analysis chamber [102]. The chamber is kept in ultra-high vacuum for permitting XPS measurements. There are two X-ray sources such as standard X-ray source and monochromator X-ray source. The quartz crystal monitors the Z positions. The magnetic field lens allows a

Chapter 2. Experimental Procedures

higher proportion of the photoelectrons without changing their energy into the analyzer. The electrostatic lens refocuses the photoelectrons into the aperture. The crystal is used to make a diffraction pattern in producing a single wavelength X-ray (i.e., monochromator X-ray). The field view aperture is a view-limiting aperture that adjusts the measurement range of capturing photoelectrons into the lens. The angle-control aperture adjusts the angle-limiting aperture for capturing photoelectrons into the lens. The upper part of the analyzer contains a hemispherical magnetic shield and a multi-detector for detecting photoelectrons.

In this study, the Magnesium X-ray source with 12 kV and 15 mA was used for acquiring wide-scan and narrow-scan spectra with binding energy resolution of 0.1 eV. Also, the Ar-ion etching (with 3 keV) was done with 0.08 Pa pressure. The XPS instrument was calibrated using an Au sample.

2.7 Humidity and reliability chamber

Specimens were stored in Platinous Sterling Chamber (Model: ESL-2C) from ESPEC as shown in Fig. 2-9. The temperature and relative humidity were held in constant mode of 15 °C and 98% RH, respectively. The temperature and humidity range of the chamber is -35 to 180 °C and 10 to 98% RH, respectively. Also, the temperature constancy is ± 0.3 °C, and the humidity constancy is ± 2.5 % RH.



Figure 2-9: Platinous Sterling Chamber (ESL-2C) [104].

CHAPTER 3.

SURFACE ROUGHNESS, CONTACT ANGLE AND HARDNESS

3.1 Surface Roughness

The three-dimensional (3-D) Atomic Force Microscope (AFM) images of Si surfaces before and after O₂ RIE plasma activations are shown in Fig. 3-1. The AFM images of the rest of the wafer surfaces at different plasma-activation times and storage conditions are given in Appendix I. Fig. 3-2 shows the surface roughness of Si, SiO₂ and glass at different surface activation times and storage conditions. The surface roughness of Si:O₂RIE increases with the increase of activation time. While the rate of increase of

surface roughness was not significant until 300 s (Fig. 3-2a), it was considerable after 300 s. The highest surface roughness (~ 6 nm) occurred at 1200 s, which is larger than in our previous study (~ 1.68 nm) [45]. This is due to use of higher plasma power and gas pressure [42],[65].

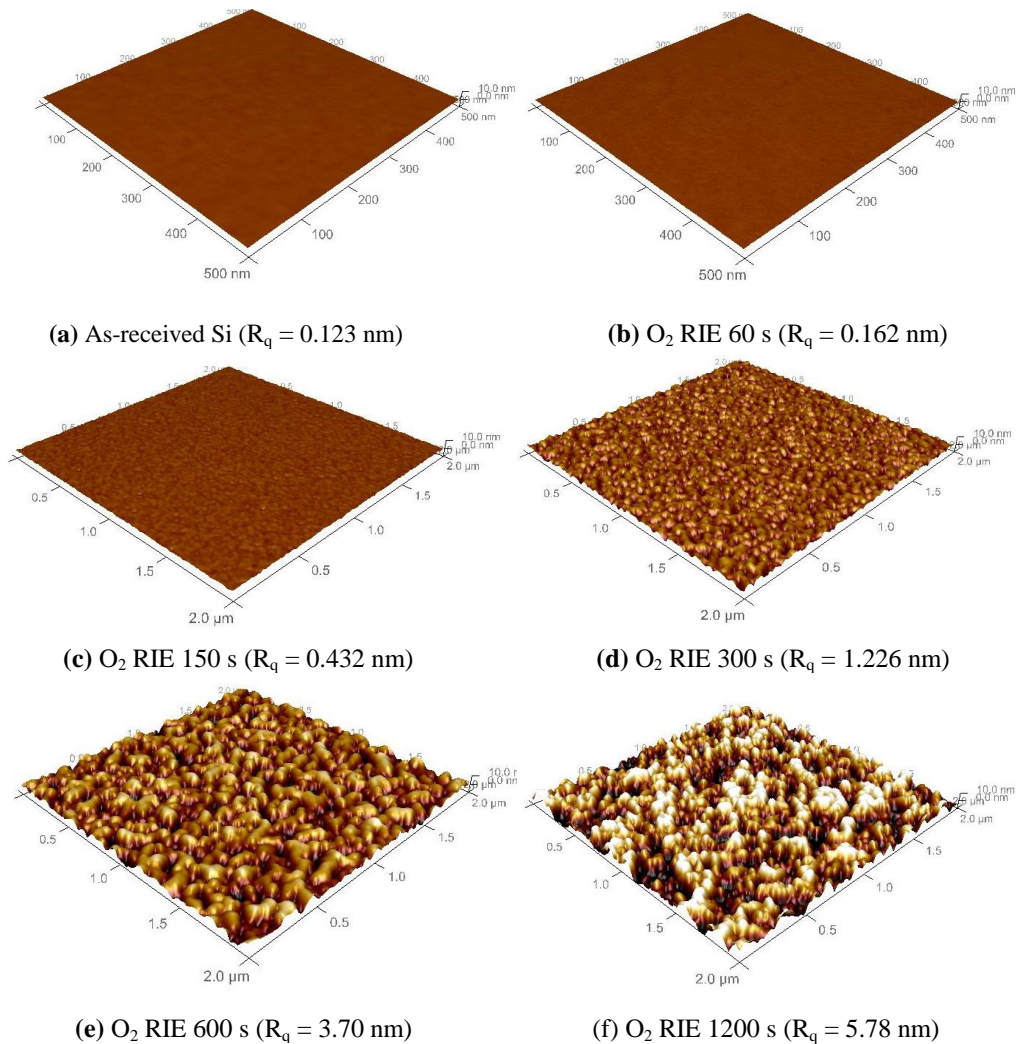


Figure 3-1: Three-dimensional (3-D) Atomic Force Microscope (AFM) images of Si wafer surfaces before and after O₂ RIE plasma activation taken by. The RMS surface roughness (R_q) due to the corresponding plasma treatment times are given in the image titles.

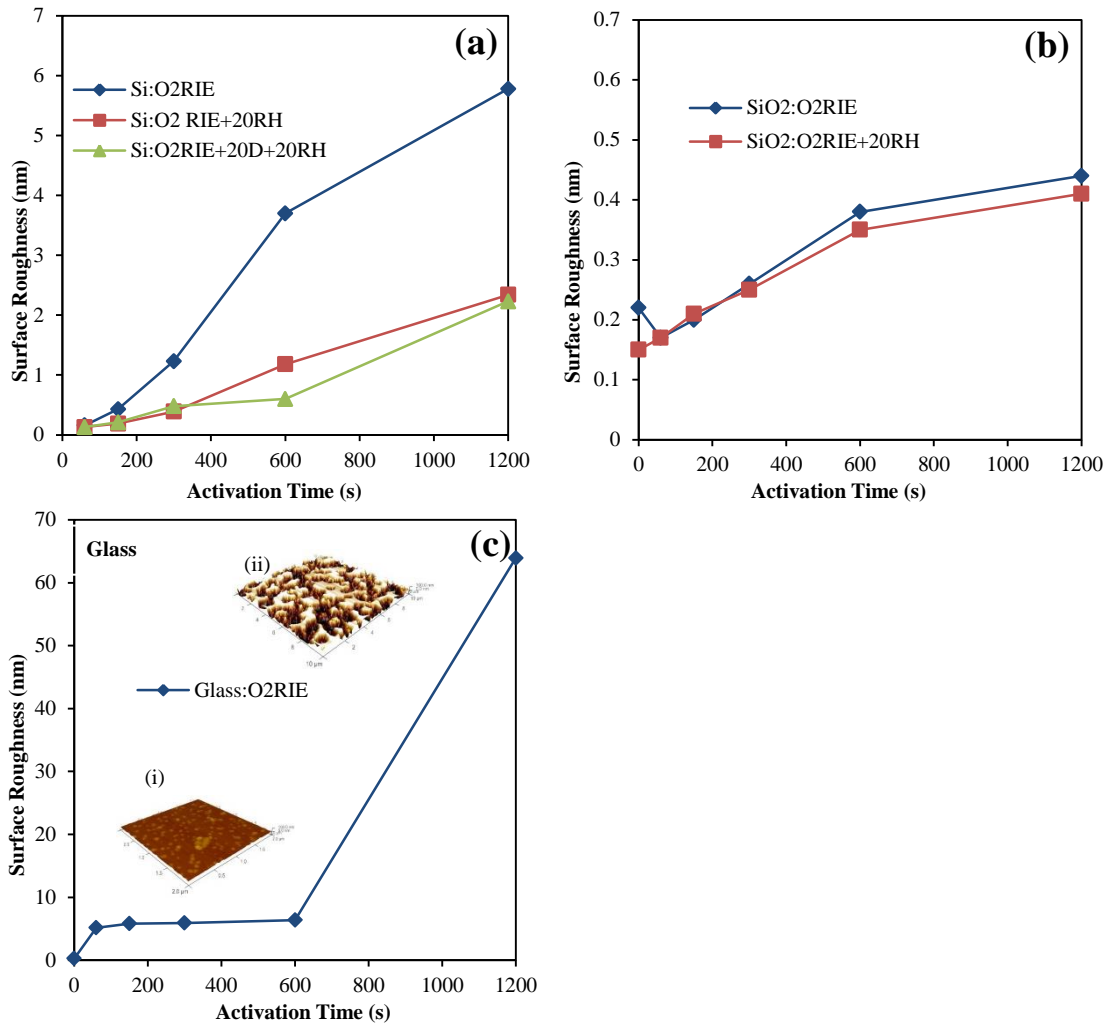


Figure 3-2: Surface roughness of (a) Si as a function of O₂ RIE plasma activation time for different storage conditions, (b) SiO₂ as a function of O₂ RIE plasma activation time for different storage conditions, and (c) Glass as a function of O₂ RIE plasma activation time. Activation time 0 s means as-received condition.

An increase of surface roughness with increasing activation time for the Si:O₂RIE+20RH and Si:O₂RIE+20D+20RH specimens was also observed. However, they show (Fig. 3-2a) reduced surface roughness as compared to Si:O₂RIE. This surface smoothing indicates the influence of high relative humidity on the Si surface. Surface smoothing was also reported [65] for Ge after oxygen plasma-activation and rinsing with DI water due to the

removal of the soluble GeO_2 layer and other defects. The modified surface was mainly terminated by hydroxyl groups. Although in our study the plasma-activated Si surfaces were not rinsed with DI water, their storage in 98% relative humidity for a long period of time caused accumulation of water molecules due to their strong affinity with the hydroxyl group [105]. Moreover, high surface roughness at higher plasma activation times increased the total surface area [65], which resulted in higher chemical affinity with the OH groups.

The surface roughness of $\text{SiO}_2:\text{O}_2\text{RIE}$ at 60 s (Fig. 3-2b) was lower than that of as-received SiO_2 before activation. A similar surface roughness reduction of SiO_2 was also observed in [41] where the surface was treated by RIE plasma with a 50 mT oxygen atmosphere, and a treatment time higher than 10 s. Such smoothing effect was attributed to surface cleaning of hydrocarbons. The lower surface roughness of as-received SiO_2 after humidity treatment might be due to the accumulation of OH groups from the humidity chamber. In both the cases (i.e., $\text{SiO}_2:\text{O}_2\text{RIE}$ and $\text{SiO}_2:\text{O}_2\text{RIE}+20\text{RH}$), the surface roughness increases with increased activation time and their amplitudes of roughness are identical. While the surface roughness of the as-received Si (0.2 nm) and SiO_2 (0.22 nm) are identical, their plasma treatment and humidity storage at identical conditions shows a higher roughness of Si than that of SiO_2 . This difference is due to the different etching rates of Si and SiO_2 during O_2 RIE activation. Unlike Si and SiO_2 , the surface roughness of glass suddenly increased after 60 s activation to about ten times (Fig. 3-2c). Afterwards, the roughness did not significantly change with the increase of

activation time until 600 s. The AFM images are identical for the surfaces activated from 60 to 600 s. An AFM image at 150 s is shown in the inset (i). The activated glass surfaces had island-like nanostructures with varying heights of 5-7 nm. In fact, at 1200 s the glass was severely damaged, causing a high surface roughness of about 63 nm (inset of Fig. 3-2c(ii)).

The lower surface roughness of Si until 300 s (Fig. 3-2a) is suitable for hydrophilic bonding due to the added benefit of higher hydrophilicity. Lower surface roughness allows for an increased area of adhesion between contacting surfaces. This is because the surface roughness determines the contact area between the wafers in the bonding. A bearing ratio analysis of the surface morphology of Si wafers revealed a clear correlation of bonding strength with surface roughness (i.e., the bearing ratio) [106]. Bearing ratio is a quantity that describes how much surface area is above a given depth (i.e., bearing depth). The higher the surface roughness, the lower the bearing ratio, which means less surface area for bonding. Therefore, surface roughness controls the adhesion between the bonding surfaces [51],[106], the interface void [75], and the hermetic sealing performance of MEMS and microfluidic devices [107], for example. On the other hand, the roughness of SiO₂ may not have significant impact on the bonding due to its lower value (higher smoothness) than that of Si. In addition, the reduction of surface roughness of Si, compared to that of SiO₂, after storage in ambient humidity, indicates that the Si surface accumulates more water molecules. Thus, SiO₂ is suitable for passivation for MEMS applications. Also, the high surface roughness of glass at prolonged activation may not be suitable for direct wafer bonding.

3.2 Water Contact Angle

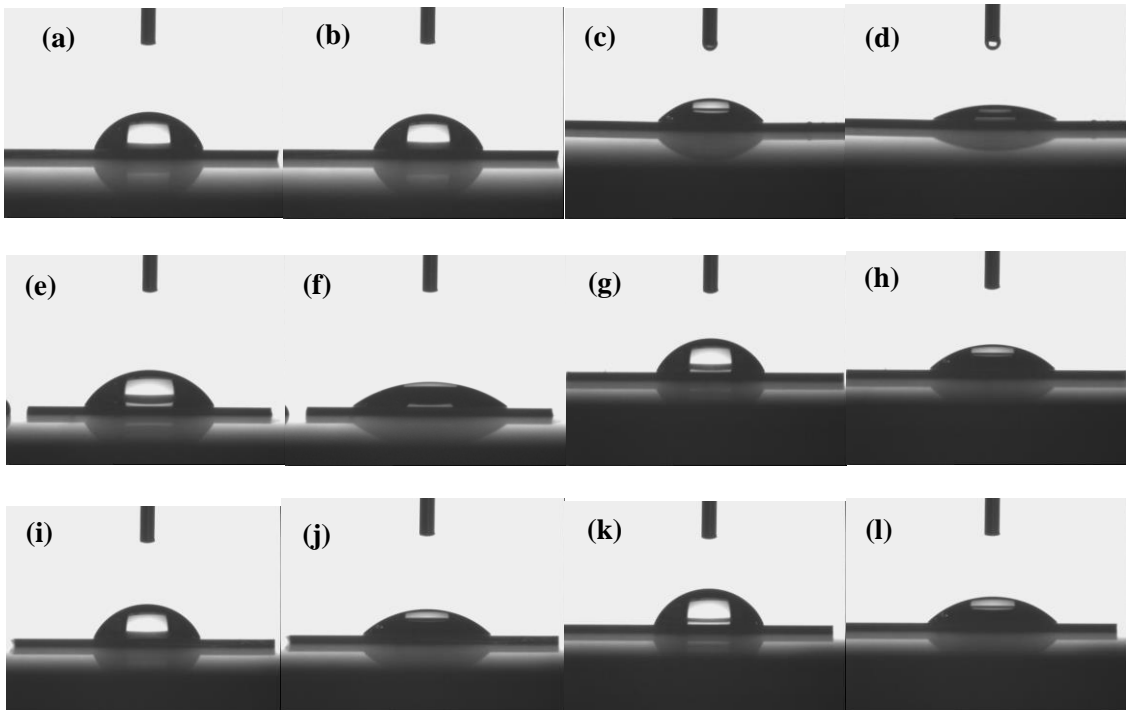


Figure 3-3: The DI water drop shape images on Si surfaces. Figures (a), (c), (e), (g), (i), and (k) correspond to drop shape images immediately after putting the water drop on as-received, 60, 150, 300, 600 and 1200 s activated Si, respectively. Figures (b), (d), (f), (h), (j), and (l) correspond to drop shape images after 2 minutes of putting the water drop on as-received, 60, 150, 300, 600 and 1200 s activated Si, respectively.

To investigate the surface reactivity and hydrophilicity of Si, SiO₂, and glass in practical processing conditions for MEMS and microfluidics, we measured the contact angle of a DI water drop. Fig. 3-3 shows the DI water drop shape images on Si wafers before and after O₂ RIE plasma activation. For each activation time, there is one pair of drop shape images. The first drop shape image of each pair was taken right after putting the water drop on the specimen surface. The second drop shape image of each pair was taken after

two minutes of elapsed time. In each pair, the first drop shape creates a relatively larger contact angle than that of the second one. In the case of plasma surface activation, this phenomenon is more obvious. The rest of the drop shape images of Si and SiO₂ at different activation times and storage conditions are given in Appendix II.

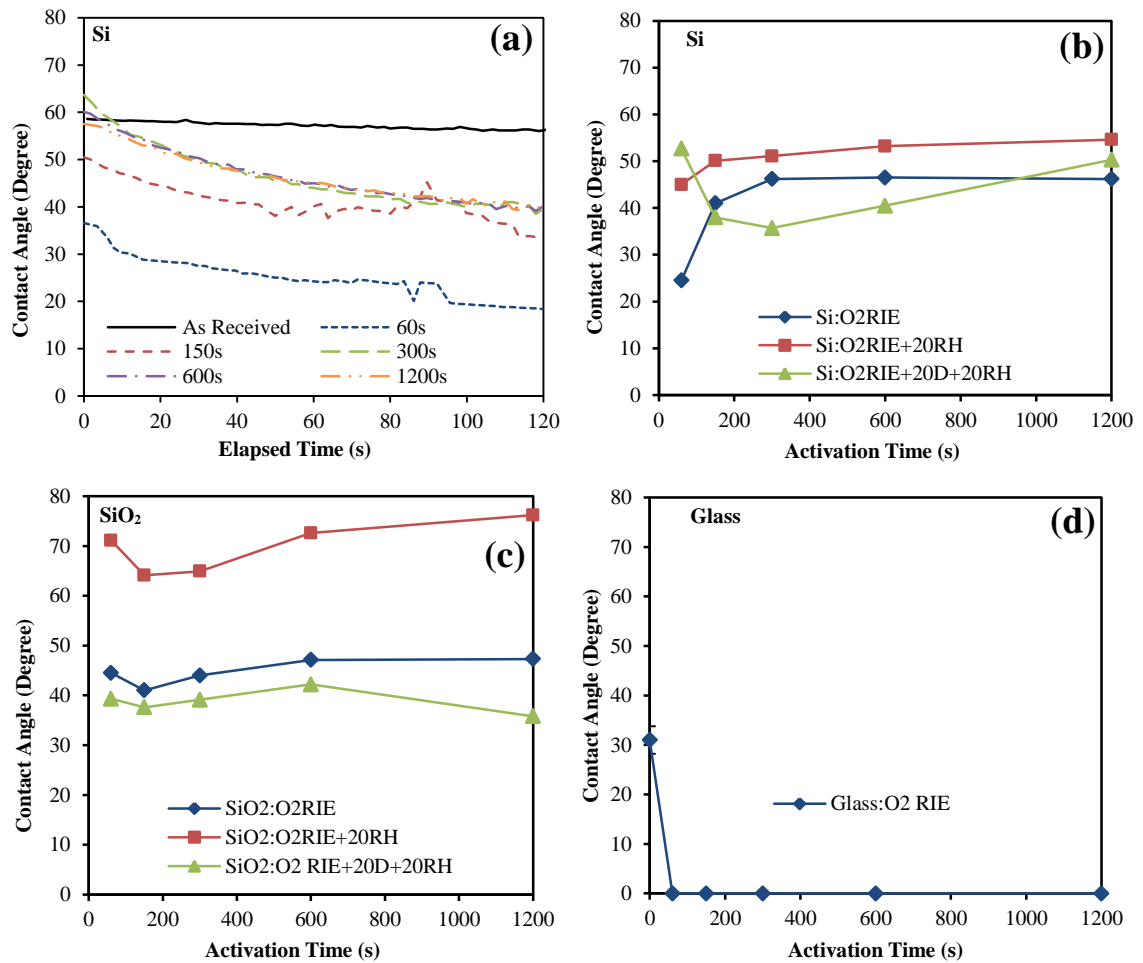


Figure 3-4: Contact angle of (a) Si as a function of elapsed time before and after O₂ RIE plasma activation at different activation times for 60 to 1200 s; (b) Si as a function of O₂ RIE plasma activation time for different storage conditions; (c) SiO₂ as a function of O₂ RIE plasma activation time for different storage conditions; and (d) glass as a function of O₂ RIE plasma activation time.

Fig. 3-4a shows the contact angle of Si:O₂RIE surface as a function of elapsed time. As-received Si shows the highest contact angle, and remains almost constant throughout the elapsed time. The plasma-activated Si shows a lower contact angle, and the contact angle decreases with a higher rate. Thus, the contact angle information gives two kinds of surface properties: surface reactivity (i.e., rate of decrease of contact angle throughout the measurement time), and surface hydrophilicity (i.e., the average contact angle).

Table 3-1: Surface reactivity of Si, SiO₂ and glass at different activation times for different treatment and storage conditions.

Specimen	Surface Reactivity (degree per second)					
	As received (0 s)	60 s	150 s	300 s	600 s	1200 s
Si:O ₂ RIE	0.02	0.12	0.09	0.16	0.15	0.14
Si:O ₂ RIE+20RH		0.02	0.03	0.02	0.03	0.04
Si:O ₂ RIE+20D+20RH		0.01	0.01	0.01	0.01	0.01
SiO ₂ :O ₂ RIE	0.02	0.08	0.11	0.10	0.12	0.12
SiO ₂ :O ₂ RIE+20RH	0.04	0.03	0.02	0.06	0.03	0.03
SiO ₂ :O ₂ RIE+20D+20RH	0.03	0.02	0.03	0.03	0.02	0.02
Glass:O ₂ RIE	0.05	-	-	-	-	-

The contact angle is the measure of the surface energy that controls the quality of the hydrophilic wafer bonding. The lower contact angle results in higher hydrophilicity and higher wetting of the surface [46]. The surface reactivity also governs the hydrophilicity since higher surface reactivity results in lower average contact angle (i.e. higher hydrophilicity). The summarized hydrophilicity of Si, SiO₂, and glass are shown in Figs. 3-4b, 3-4c and 3-4d, respectively. Each marker represents average contact angle at that particular plasma-activation time and storage condition. On the other hand, the surface reactivity (i.e., rate of decrease of contact angle, unit: degree/second) of Si, SiO₂, and

Chapter 3. Surface Roughness, Contact Angle and Hardness

glass is summarized in Table 3-1. The surface reactivity and hydrophilicity controls the bondability and reliability of MEMS and integrated heterogeneous systems [33].

The high surface reactivity of Si:O₂RIE (Table 3-1) as compared to as-received Si is due to removal of native oxides and organic contaminants and the increased number of dangling bonds (free bonds) from broken Si-O and Si-H [46]. Similar surface reactivity behavior is also observed in the case of SiO₂:O₂RIE (Table 3-1). The increased surface reactivity also leads to higher surface energy and hence increased adhesion and bonding strength in plasma-activated wafer bonding [108].

The surface reactivity of SiO₂:O₂RIE is slightly lower than that of Si:O₂RIE, indicating high bonding strength of Si-based wafer bonding [33], [109]. Besides, the Glass:O₂RIE showed highest surface reactivity, which makes it a promising candidate for anodic bonding [42]. The DI water drop quickly spread on the O₂ RIE plasma-processed glass surface, resulting in a contact angle that was below the measurement limit of the equipment. Storage in 98% relative humidity (i.e., O₂RIE+20RH) and ambient humidity (i.e., O₂RIE+20D+20RH) shows a significant reduction in the surface reactivity of Si and SiO₂ (Table 3-1) due to the augmented OH groups on the surface [45]. It has also been reported [65] that the surface reactivity of Si and SiO₂ are at their maximum immediately after plasma activation, even though they remain hydrophilic in excess of 150 h after plasma activation. The highly reactive surface attracts particles from air when exposed in ambient conditions for a long period of time, eventually decreasing its surface reactivity as well as hydrophilicity.

The contact angles of as-received Si and SiO₂ are almost identical (~57°, Figs. 3-4b, 3-4c), and are higher than that of as-received glass (30°, Fig. 3-4d). Glass:O₂RIE shows the highest hydrophilicity (contact angle <5°), and Si:O₂RIE shows higher hydrophilicity (24.5°) than that of SiO₂:O₂RIE at 60 s. In a previous study, the contact angle of as-received SiO₂ was reported as 52° [89] with 9 µl DI water droplet, and O₂ RIE plasma-activated Si and SiO₂ was reported as 29.1° and 38.5°, respectively with flow rate of 50 sccm, power of 200 W, chamber pressure of 60 Pa, and plasma treatment time 30 s [89]. In another study, the contact angle of oxygen plasma treated glass was <5° at a plasma power of 140 W, working pressure of 20 mTorr, and activation time of 60 s [42]. The variation in the comparative analysis of the contact angle can be attributed to the use of different measurement techniques, plasma powers, activation times, chamber pressures, and length of exposure time in ambient conditions before measurement.

With increased activation time, the contact angle of Si increases until 300 s and becomes saturated at 600 s (46.5°) and 1200 s (46.2°). This is due to increased surface roughness (discussed in section 3.1) of Si:O₂RIE at higher activation times. Surface roughness obstructs the spreading of a water droplet in the contact angle measurements. A higher surface roughness creates a larger barrier to the spreading of water, resulting in larger contact angle and vice-versa [110]. On the other hand, the contact angle of SiO₂:O₂RIE does not change significantly with activation time (Fig. 3-4c). The highly passivated SiO₂ layer is less likely to react with oxygen plasma. The lower activation times of Si:O₂RIE can thus result in good bonding due to higher hydrophilicity and reactivity of the surface

(Fig. 3-4b). On the other hand, higher contact angles in the case of Si:O₂RIE+20RH (Fig. 3-4b) and SiO₂:O₂RIE+20RH (Fig. 3-4c) reflects their reduced surface reactivity and lower hydrophilicity due to passivation of the dangling bonds. The initial decrease of contact angle of Si:O₂RIE+20D+20RH until 300 s and its increase afterwards (Fig. 3-4b) is attributed to the surface roughness-induced variation in the amount of Si-(OH)_x bonds [93].

The decrease of contact angle for SiO₂:O₂RIE+20D+20RH (Fig. 3-4c), in contrast to that of SiO₂:O₂RIE, was due to the increased incorporation with OH groups resulting from ambient and 98% relative humidity conditions. Thus, Si and SiO₂ need proper passivation to reduce the risks of poor adhesion due to humidity-induced increased hydrophilicity in MEMS packaging [91]. Also, storage in ambient humidity can result in good bondability, since the gap-closing mechanism in room temperature direct wafer bonding requires water vapor from ambient conditions to initiate covalent bonding between the surfaces [111]. For further enhancement of bonding strength, a low temperature (i.e., 300 °C) heating for a short period of time (i.e., 2 h) was reported [111],[45]. The findings here can also be extended to the sequential plasma-activated bonding (O₂ RIE + N₂ radicals) of Si/Si [46], Si/Pyrex glass [42], glass/glass [90], Si/Ge and SiO₂/Ge [89].

3.3 Surface Hardness

Development of MEMS devices for the existing pressure-sensing and force-sensing systems, [112] as well as emerging applications such as energy harvesting [113], require materials that may have to go through different processing steps such as surface activation using plasma for the bonding, integration, and packaging of MEMS devices [44]. Therefore, the nanoindentation hardness test is commonly used to evaluate the mechanical properties and reliability of MEMS structures [71]. Fig. 3-5a shows a typical force-indentation depth curve, applying 10 mN peak force in the cycle test and the load-unload test of as-received Si. The load-unload test has only one loading and unloading curve, whereas the cycle test has five. Both the cycle tests and load-unload tests were done in 5 and 10 different positions, respectively, for each specimen. Figs. 3-5 (d-f) and 3-5 (g-i) show the summarized Martens' hardnesses results for Si and SiO₂, respectively, at different activation times and storage conditions. Hereafter, the term hardness will be used instead of Martens' hardness. Each marker on the plot shows average hardness and the error bar shows the standard deviation of the hardness from the average.

The surface hardness of Si may be attributed to the crystal structure, deposited layers, absorbents, morphology, and reactivity of the surfaces. For example, the loading-unloading process in the cycle test for as-received Si (Fig. 3-5a) shows hysteresis. It could be due to pressure-induced phase transformation [71] of Si from diamond cubic form into β -tin form with a 22% decrease in volume.

Chapter 3. Surface Roughness, Contact Angle and Hardness

Since the surface roughness of the as-received Si and Si:O₂RIE at 60 s are identical, the lower hardness for the as-received Si (Fig. 3-5d) may be attributed to the native oxides and contaminants. Alternatively, the increase of hardness at 60 s is due to the removal of the native oxides. On the other hand, if only the lower deviation is considered at 150 s of Si:O₂RIE, a decreasing trend in the hardness of Si is observed with the increase of activation time both in the cycle test and load-unload test. This decrease could be related to higher surface roughness and changes in the atomic structure of the surfaces.

As discussed in the previous section, the surface roughness of Si increases with the increase of activation time. Therefore, higher surface roughness results in a lower contact area for the indenter tip, which causes an increase of the indentation depth observed in the depth versus force profiles. The indentation depth for the as-received Si at low activation times (i.e., 60 s and 150 s) is lower (~0.26 μm) than that (~0.30 μm) of the higher activation times (i.e., 600 s and 1200 s). Therefore, the surface roughness controls the hardness of Si. It is also known that a surface treatment using plasma, with enough physical sputtering capability, results in an amorphous layer [114]. The decrease of hardness with the increased activation time (Fig. 3-5d) may also be attributed to the formation of an amorphous layer at higher plasma activation times. The formation of an amorphous layer in the plasma surface-activated wafer bonding was demonstrated elsewhere [115].

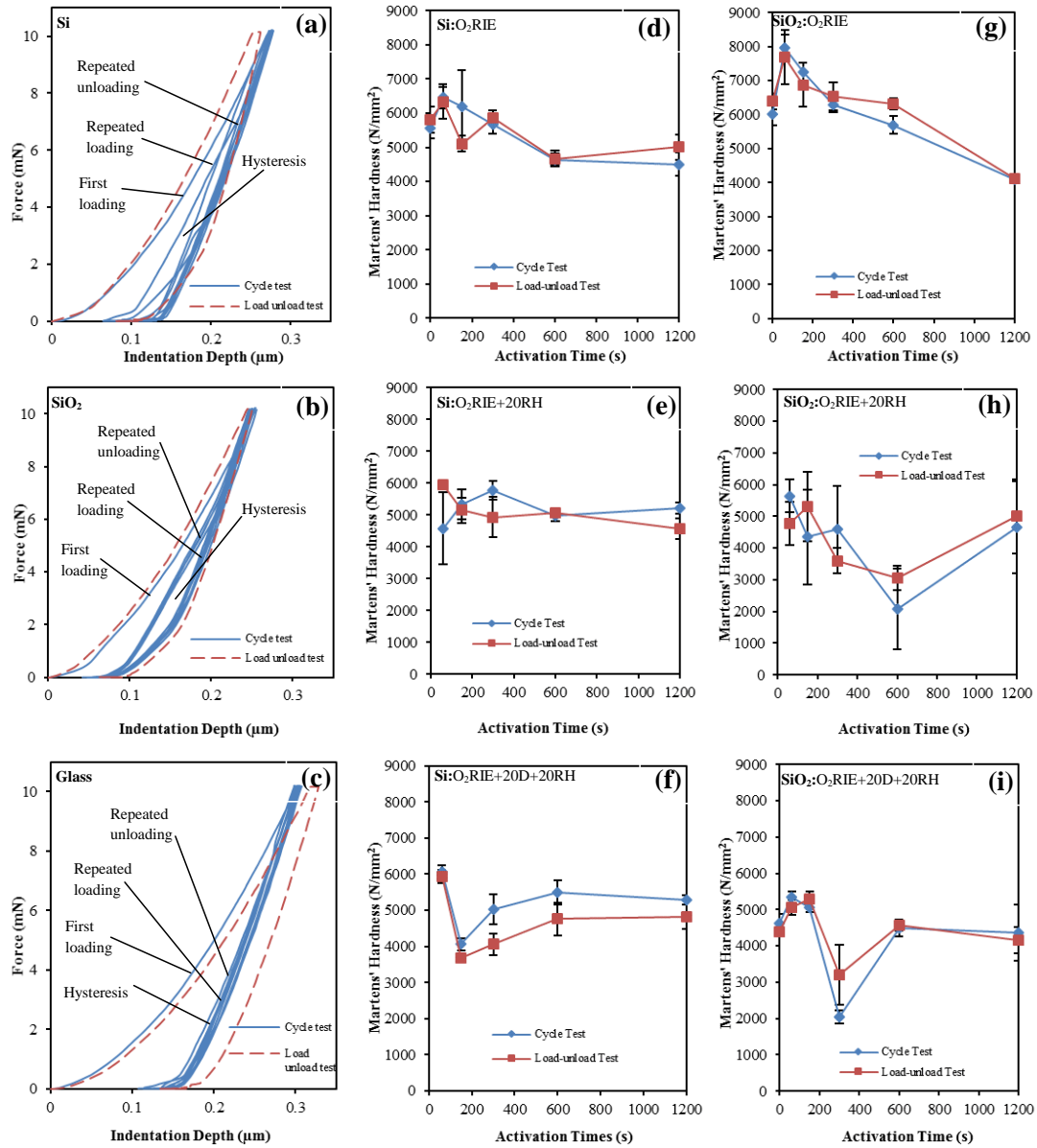


Figure 3-5: Indenter force vs. indentation depth of (a) as-received Si, (b) as-received SiO₂, and (c) as-received glass, in cycle tests and load-unload tests for the analysis of Martens' hardness. Martens' hardness using cycle tests and load-unload tests as a function of O₂ RIE plasma activation time for (d) Si without storing, (e) Si after storing in 98% relative humidity for 20 days, and (f) Si after storing in ambient humidity for 20 days and in 98% relative humidity for 20 days, (g) SiO₂ without storing, (h) SiO₂ after storing in 98% relative humidity for 20 days, and (i) SiO₂ after storing in ambient humidity for 20 days and in 98% relative humidity for 20 days.

There was no considerable influence of humidity on the hardness of Si:O₂RIE+20RH (Fig. 3-5e). However, a decreasing trend of the hardness was observed in load-unload tests. Also, the rate of decrease of hardness for Si:O₂RIE+20RH with increased activation time was lower than that of Si:O₂RIE in load-unload tests. Further storage in ambient humidity (i.e., Si:O₂RIE+20D+20RH, Fig. 3-5f) caused a decrease in hardness (~6000 to ~3500 N/mm²) from 60 to 150 s, and an eventual increase up to ~5000 N/mm² at 1200 s. The ambient- and 98% relative humidity-storage-induced variation in the hardness attributes to the quality of the complex formation of the absorbents (e.g., -OH) and deposited layers (e.g., carbon) on the surface. The surface reactivity determined by the relative composition of surface oxides due to hydroxyl groups (i.e., Si-OH) and sub-oxides (i.e., Si-O₂, Si-O₄) also may influence on the hardness of Si.

The repeated force-indentation depth curves of the as-received SiO₂ (Fig. 3-5b) shows higher hysteresis than that of Si (Fig. 3-5a). The hardness behavior of SiO₂:O₂RIE is identical to that of Si (Fig. 3-5g), except for its higher values from 60 to 600 s, and its lower value at 1200 s. For SiO₂:O₂RIE+20RH (Fig. 3-5h), the hardness decreased except for 1200 s activation time both in the load-unload test and the cycle test. On the other hand, for SiO₂:O₂RIE+20D+20RH (Fig. 3-5i), the hardness values in load-unload tests did not change significantly, if only the upper deviation at 300 s is considered.

Unlike Si, the surface roughness may not have significant impact on the reduction of hardness, since SiO₂ shows a small increase of surface roughness with increased

activation time. The role of deposited oxides, hydroxyl layers/absorbents, and surface reactivity on the hardness of SiO₂ is not clear from this study due to its higher hardness than that of the surface additives. Unlike Si and SiO₂, glass showed the least amount of hysteresis (Fig. 3-5c). Also, the change in the hardness ($\sim 4000 \text{ N/mm}^2$, not shown in Fig. 3-5) of Glass:O₂RIE was insignificant with the increase of activation time except for when it reached 1200 s, where it reduced to almost half ($\sim 2000 \text{ N/mm}^2$). This reduction in the hardness may be attributed to the severe damage of glass surface after such a long activation time. The surface roughness of glass for this condition was increased by more than ten times that of the as-received specimen.

A comparison among the O₂ RIE-treated specimens (Figs. 3-5d, 3-5g and Glass:O₂RIE) shows that SiO₂ has the highest hardness and glass has the lowest hardness for identical conditions of activation time. The loading and unloading curves show the plastic and elastic deformation of the surface [116]. Whereas the as-received glass has an elasticity of $\sim 7.5 \times 10^4 \text{ N/mm}^2$, the elasticity of as-received Si and SiO₂ surfaces is almost equal at about $\sim 1.2 \times 10^5 \text{ N/mm}^2$. Thus, the glass has lower plastic deformation as compared to Si and SiO₂. The lower plastic deformation of glass makes it a good candidate material for microfluidic devices with other polymer or flexible materials [117]. The summarized surface properties of Si, SiO₂ and glass are shown in Table 3-2.

Table 3-2: Evolution of Surface properties with the increase of oxygen plasma activation times at different storage conditions.

Surface Treatment	Change in surface properties with the increase of activation times (60, 150, 300, and 600 s) under different storage conditions				
	Surface Roughness	Surface Reactivity	Hydrophilicity	Hardness	Bondability
Si:O ₂ RIE	Increases	High	High	Decreases	Better at lower activation time [45]
Si:O ₂ RIE+20RH	Slower increase than Si:O ₂ RIE	Low	Low	Slight decrease	Good at lower activation
Si:O ₂ RIE+20D+20RH	Similar to Si:O ₂ RIE+20RH	Very low	High	Overall decrease	Good at lower activation
SiO ₂ :O ₂ RIE	Slight increase	High	High	Decreases	Better at lower activation time
SiO ₂ :O ₂ RIE+20RH	Similar to SiO ₂ :O ₂ RIE	Low	Low	Slight decreases	Better at lower activation time
SiO ₂ :O ₂ RIE+20D+20RH	-	Very low	High	Overall decrease	Good at lower activation
Glass:O ₂ RIE	~ 5-10 nm	Very high	Very high	Negligible change	Better at low activation time

3.4 Conclusions

The water contact angle, roughness, and hardness of oxygen reactive-ion etching (O₂RIE) plasma-activated silicon (Si), silicon dioxide (SiO₂), and glass surfaces with or without storage in ambient and 98% relative humidity conditions were investigated. The surface roughness of Si increased as a function of plasma activation time, which was higher than that of SiO₂. Plasma-activated Si showed reduced surface roughness after treatment with humidity and air. However, no considerable change was observed in the case of SiO₂. This reduction in the roughness of Si is due to the higher accumulation of water molecules on the Si surface. The surface roughness of glass suddenly increased after activation by an order of magnitude, then was unchanged until 600 s, and finally

increased by another order of magnitude at 1200 s. The increase of the surface roughness of glass at 1200 s is due to severe surface damage. The low surface roughness induced by low plasma-activation times is suitable for bonding.

Lower contact angle was observed for the oxygen plasma-activated Si than that of as-received Si. It also showed a trend of increasing activation time. Si and SiO₂ also showed high surface reactivity after plasma activation. The surface reactivity of Si and SiO₂ were considerably reduced after storage in ambient humidity. Plasma-activated Si and SiO₂ surfaces showed a decreased contact angle due to the augmented OH groups in ambient humidity. Furthermore, plasma-activated glass was highly reactive and had a hydrophilic surface. The high reactivity and hydrophilicity resulted in contact angles below 2°, which is beyond the detection limit of the equipment. Better bondability can be achieved at lower activation time because of high hydrophilicity and surface reactivity. Also, high hydrophilicity after ambient humidity treatment may also have good bondability if the surface contains considerable OH groups.

The loading-unloading results in the hardness test identify hysteresis for Si, SiO₂ and glass due to the pressure-induced phase transformation. The higher surface roughness and formation of amorphous layers of Si caused a decreased hardness of Si with an increased activation time. Also, an increased surface roughness caused considerable reduction in the hardness of the plasma-activated glass at 1200 s. Moreover, Si and SiO₂ showed ambient- and 98% relative humidity-storage-induced variations on their hardness. This dependence of the hardness on storage humidity conditions can be attributed to the

Chapter 3. Surface Roughness, Contact Angle and Hardness

complex formation of the absorbents (e.g., OH), deposited layers (e.g., carbon), oxides (i.e., Si-OH) and sub-oxides (i.e., Si-O₂, Si-O₄) on the surface. The effect of hardness on bondability needs further investigation.

CHAPTER 4.

SURFACE CHEMICAL ANALYSIS

4.1 Silicon

The chemical states of the Si surfaces treated with O₂ RIE plasma-activation and/or different storage conditions are shown in Fig. 4-1. Charge correction was done by shifting the position of the Si_{2p} peak binding energy at 99.0 eV, since there was no significant carbon peak [68]. The wide-scan XPS spectra of as-received Si (Fig. 4-1a) shows peaks at 100, 150, 284 and 532 eV for Si_{2p}, Si_{2s}, C, and O_{1s}, respectively [77],[102]. The wide-scan spectra of plasma-activated Si shows additional peaks of fluorine at 688 eV and Cu_{LVV} at 600 eV. The presence of fluorine might be due to

physisorbed or chemisorbed surface contaminants during hydrofluoric acid treatment for wafer cleaning [118]. The $\text{Cu}_{L_{VV}}$ peak is due to the copper clamp used for holding the specimens during XPS acquisition. However, 40 s etching of the plasma-activated surfaces using Ar-ion removed the fluorine peaks. Strong peaks for Si_{2p} and Si_{2s} were observed. High-resolution XPS spectra of O_{1s} and Si_{2p} peaks are shown in Figs. 4-1b to 4-1d and 4-1e to 4-1f, respectively, for different storage conditions.

The dashed and solid lines in Fig. 4-1 indicate the O_{1s} and Si_{2p} peaks. The peak positions shift to the higher binding energies with increased activation times. The O_{1s} and Si_{2p} peaks were deconvolved using the mixed Gaussian/Lorentzian function to understand the nature of the embedded components of the chemical elements. The maximum full-width-half-maximum (FWHM) of the deconvolved peaks was 1.0 eV.

The deconvolved O_{1s} and Si_{2p} peaks for the as-received Si are shown as typical examples in Figs. 4-2a and 4-2b, respectively [105],[119],[120]. The peaks in the deconvolved O_{1s} spectra (Fig. 4-2a) are mainly composed of $\text{Si}(\text{-O})_2$, $\text{Si}(\text{-OH})_x$, and $\text{Si}(\text{-O})_4$ (tetrahedral silicon oxide) that appeared at 531.97, 531.12, and 532.95 eV respectively. The deconvolved Si_{2p} spectra (Fig. 4-2b) are composed of three peaks: Si_0 , $\text{Si}(\text{-OH})_x$, and $\text{Si}(\text{-O})_2$, that appeared at 99.0, 99.49, and 102.6 eV respectively. For further clarification of the influence of plasma, ambient and 98% relative humidity on the $\text{Si}(\text{-O})_2$, $\text{Si}(\text{-OH})_x$, and $\text{Si}(\text{-O})_4$, a succinct analysis (without Figure) is given in the following paragraphs.

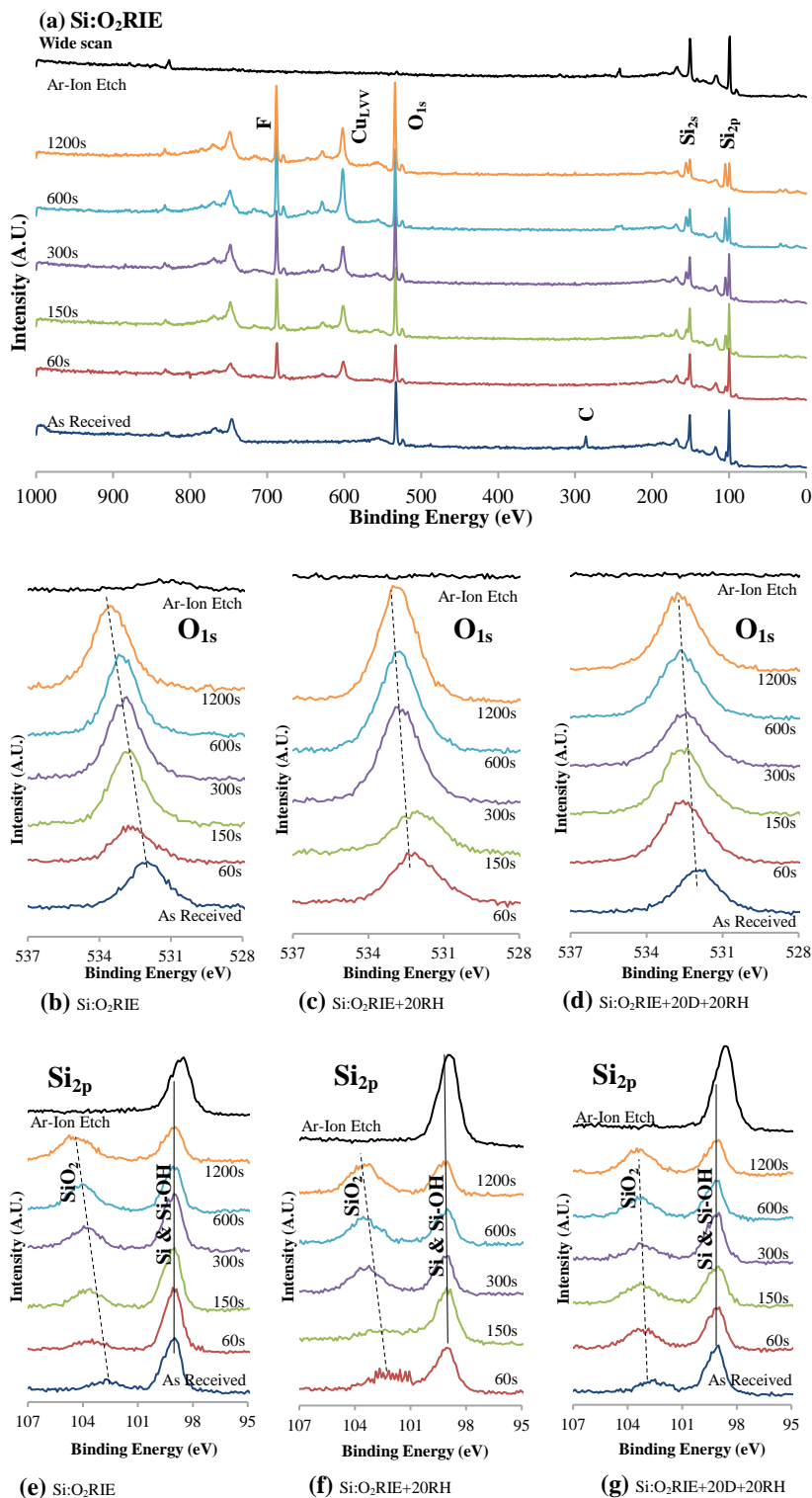


Figure 4-1: (a) XPS wide-scan spectra of Si before and after O₂ RIE plasma activation. XPS O_{1s} spectra as a function of O₂ RIE plasma-activation time for (b) Si without storing, (c) Si after storing in 98% relative humidity for 20 days, and (d) Si after storing in ambient humidity for 20 days, and in 98% relative humidity for 20 days. XPS Si_{2p} spectra as a function of O₂ RIE plasma activation time for (e) Si without storing, (f) Si after storing in 98% relative humidity for 20 days, and (g) Si after storing in ambient humidity for 20 days, and in 98% relative humidity for 20 days.

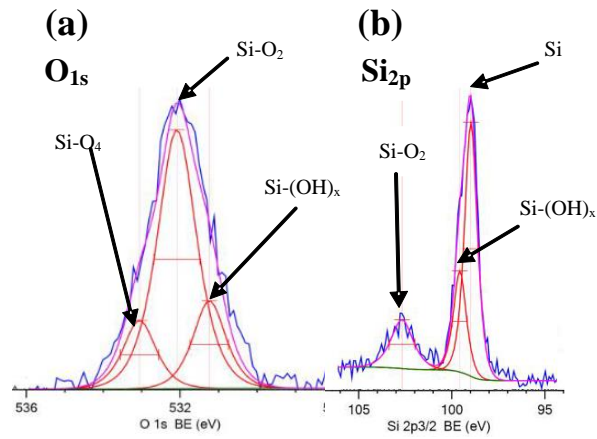


Figure 4-2: Deconvoluted XPS spectra of (a) O_{1s} and (b) Si_{2p} for as received Si.

Table 4-1 summarizes the energy shifts and changes of FWHM of the deconvoluted components of O_{1s} and Si_{2p} for Si at different plasma-treatment and storage conditions (details are given in Appendix III). In the case of Si:O₂RIE, the energy shift of Si(-O)₂ is significant due to O₂ RIE oxidation of the surface compared to Si(-OH)_x and Si(-O)₄. Also the increase of FWHM of Si(-O)₂ for O_{1s} spectra is higher than that of Si(-OH)_x and Si(-O)₄. For Si:O₂RIE+20RH, while considerable energy shifts of Si(-O)₂, Si(-OH)_x, and Si(-O)₄ are observed for O_{1s} spectra, only the Si(-O)₂ energy shift in Si_{2p} spectra is observed. But the overall FWHM of all the components is not considerably changed. These results may be indicative of the overlapping of the O₂ RIE oxidation (i.e., Si(-O)₂) of the surface by the water molecules from humidity storage (i.e., Si(-OH)_x). For Si:O₂RIE+20D+20RH, the binding energy shift of Si(-OH)_x is more significant than that of other components, both in the O_{1s} and Si_{2p} spectra. The FWHM of all the components is unchanged. Therefore, the ambient storage of the O₂ RIE-treated surface might have more considerable Si-OH coverage than the SiO₂ layers.

Table 4-1: Binding Energy shift and change of FWHM of the deconvolved components of O_{1s} and Si_{2p} for Si at different plasma treatment and storage conditions. The energy shift and change of FWHM at any activation time are calculated with respect to the previous activation time/condition. For example, the increase/decrease of energy shift at 60 s is calculated by comparing the components of the peak positions at 60s with respect to the components of the peaks positions for as-received conditions. The upward and downward arrows indicate increase and decrease of energy and FWHM, respectively. “0” means no change.

Condition	Element	Component	Shift of Binding Energy (eV)					Change of FWHM (eV)				
			60s	150s	300s	600s	1200s	60s	150s	300s	600s	1200s
Si:O ₂ RIE	O _{1s}	Si(-OH) _x	↑0.5	↑0.1	0	↑0.5	↑0.4	↑0.2	↓0.1	↓0.2	↑0.1	↑0.1
		Si(-O) ₂	↑0.7	↑0.1	↑0.1	↑0.4	↑0.2	↑0.1	↑0.1	↑0.1	↓0.1	0
		Si(-O) ₄	↑0.6	↑0.3	↓0.2	↑0.1	↑0.8	↓0.2	↓0.1	↑0.2	0	↑0.1
	Si _{2p}	Si	0	0	0	0	0	↑0.2	↓0.1	0	↓0.1	0
		Si(-OH) _x	0	↑0.1	↓0.2	0	↑0.2	↓0.1	↑0.1	0	0	0
		Si(-O) ₂	↑1.0	↑0.1	↑0.2	↑0.2	↑0.4	↑0.3	↓0.1	↓0.1	0	↑0.3
Si:O ₂ RIE +20RH	O _{1s}	Si(-OH) _x		0	↑0.8	↑0.2	0		↓0.2	0	↑0.1	↓0.1
		Si(-O) ₂		↓0.2	↑0.6	↑0.2	0		↑0.1	↓0.1	0	0
		Si(-O) ₄		0	↑0.3	↑0.4	↓0.1		0	0	0	0
	Si _{2p}	Si		0	0	0	0		↑0.1	↓0.1	0	0
		Si(-OH) _x		↑0.4	↓0.4	↓0.1	0		0	↓0.2	↑0.1	0
		Si(-O) ₂		↑0.2	↑1.0	↑0.1	0		0	0	↓0.1	0
Si:O ₂ RIE +20D +20RH	O _{1s}	Si(-OH) _x	↑0.5	↑0.3	↓0.2	↑0.2	↓0.1	0	↑0.1	↓0.1	0	↓0.1
		Si(-O) ₂	↑0.6	0	0	↑0.2	0	0	0	0	0	0
		Si(-O) ₄	↑0.3	↓0.1	0	↑0.3	0	↓0.1	0	0	0	↓0.1
	Si _{2p}	Si	0	0	0	0	0	0	↑0.2	↓0.2	↑0.1	↓0.1
		Si(-OH) _x	0	↑0.1	↑0.1	0	↓0.1	0	0	0	0	0
		Si(-O) ₂	↑0.7	0	↓0.1	↑0.2	↑0.1	↑0.1	0	↓0.1	0	0

The shifts in the binding energies (Table 4-1) show the dependence of the chemical changes of the surface functional groups on the reactions due to the O₂ RIE oxide film, ambient and 98% relative humidity [68]. In general, oxidation of atoms shifts their binding energy [81]. Higher oxidation results in a higher shift of the binding energy [102]. This indicates that an increased activation time using O₂ RIE plasma shifts Si(-O)₂

to the higher binding energy. The high surface reactivity for Si:O₂RIE may also be attributed to the energy shift of Si(-O)₂ [92]. For both Si:O₂RIE+20RH and Si:O₂RIE+20D+20RH, the insignificant shift in binding energy of Si(-O)₂, and the significant shift to that of Si(-OH)_x, may be attributed to the introduction of humidity and the reduction in surface reactivity. To demonstrate the role of oxidation on the binding energy, we etched all the Si:O₂RIE-, Si:O₂RIE+20RH-, and Si:O₂RIE+20D+20RH-treated surfaces inside the XPS chamber. The results are shown in the ‘Ar-ion Etch’ curves in Fig. 4-1. After etching, the O_{1s} peak completely disappears after ~40 s of Ar-ion etching (pressure 0.08 Pa) of the surface. Also, the Si(-O)₂ peaks of Si_{2p} spectra in Figs. 4-1e, 4-1f, and 4-1g disappear after Ar-ion etching. This supports the conclusion in reference [102] and [81] that oxidation plays a major role in shifting the binding energy. The etched surface shows the Si peak at a lower binding energy than that of the as-received surface.

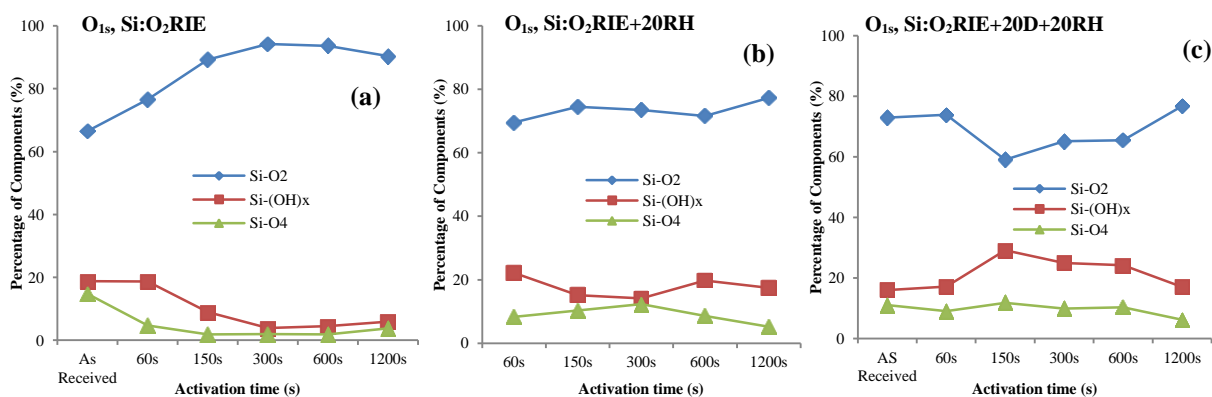


Figure 4-3: Percentage of Si-O₂, Si-(OH)_x, and Si-O₄ components in O_{1s} XPS spectra of (a) Si without storing, (b) Si after storing in 98% relative humidity for 20 days, and (c) Si after storing in ambient humidity for 20 days, and in 98% relative humidity for 20 days.

We have also summarized the amount of $\text{Si}(-\text{O})_2$, $\text{Si}(-\text{OH})_x$, and $\text{Si}(-\text{O})_4$ from the deconvolved O_{1s} and Si_{2p} spectra as a function of activation time with or without storage in ambient humidity and 98% relative humidity in Fig. 4-3. Figs. 4-3a to 4-3c correspond to Figs. 4-1b to 4-1d, respectively. The variation of $\text{Si}(-\text{O})_2$, $\text{Si}(-\text{OH})_x$, and $\text{Si}(-\text{O})_4$ may be explained by the plasma-induced changes in surface roughness and crystal-oriented oxidation. The oxidation rate is defined as the rate of reaction between water molecules and silicon bonds at the silica-silicon interface [121]. The Si wafer for our analysis had (100) crystal orientation. The number of available bonds per cm^2 to react with water (known as N) is the smallest in (100) crystal orientation. As the roughness of the Si surface increases, other crystal orientations such as (110), (111), and (311) are more exposed to the water molecules derived from the ambient humidity and 98% relative humidity chambers. These orientations have a higher value of N as compared to the (100) orientation, resulting in larger oxidation rates [121].

With the increased activation time up to 150 s, the surface roughness of Si surface is not increased significantly (i.e., ~ 0.25 nm for $\text{Si}:\text{O}_2\text{RIE}+20\text{D}+20\text{RH}$), as compared to the higher activation times (e.g., ~ 2.5 nm in 1200 s for $\text{Si}:\text{O}_2\text{RIE}+20\text{D}+20\text{RH}$) [92]. Thus, the percentage of $\text{Si}(-\text{O})_2$ components decreases until 150 s in Fig. 4-3(c) due to lower surface roughness. This lower surface roughness does not allow for the exposing of other crystal orientations. On the other hand, the $\text{Si}(-\text{O})_2$ increases from 300 to 1200 s due to high surface roughness. The high surface roughness dominantly oxidizes due to the exposure of crystal orientations other than (100). The increase of $\text{Si}(-\text{OH})_x$ until 150 s and

then its decrease (Fig. 4-3c) is also correlated with the surface roughness and oxidation. Due to lower surface roughness until 150 s, the accumulated water is higher compared to that of the higher surface roughness. Here, the total surface area plays a dominant role in increasing the $\text{Si}(\text{-OH})_x$ on the surface. With higher surface roughness, the total surface area increases significantly and results in decreased $\text{Si}(\text{-OH})_x$, as shown in the activation time from 300 to 1200 s. However, these explanations assume the crystal orientation-dependent oxidation may be incorrect if there is a decreased oxidation rate at a higher surface roughness due to the exposure of the least reactive crystal planes (e.g., (111)) [122].

The plasma-induced $\text{Si}(\text{-O})_2$ and $\text{Si}(\text{-OH})_x$ increase the surface reactivity and hydrophilicity that control the direct bonding of Si based substrates [41]. The higher amount of $\text{Si}(\text{-OH})_x$ below 300 s (Fig. 4-3a) activation time for $\text{Si}:\text{O}_2\text{RIE}$ controls the sorption on the surface that is directly involved in the hydrophilic wafer bonding [111]. Also, the $\text{Si}(\text{-O})_4$ is required for the absorption of voids. These results are consistent with the summary table (Table 4-1) of surface properties and bondability in references [41] and [45]. The 98% relative humidity- and ambient humidity-induced $\text{Si}(\text{-OH})_x$ also play a significant role in enhanced adhesion for good bondability with low temperature heating (below 300 °C) [111].

4.2 Silicon Dioxide

Fig. 4-4a shows the wide-scan spectra of SiO₂:O₂RIE. Charge correction was done by shifting the position of the C peak binding energy at 284.0 eV. The peaks at 100, 150, 284, 531, 933 and 953 eV are for Si_{2p}, Si_{2s}, C, O_{1s}, Cu_{2p3/2}, and Cu_{2p1/2}, respectively [102]. Here also, the Cu peaks might be due to the copper clamp in the specimen holder. As compared to Si and glass, SiO₂ has stronger Cu peaks. This is due to smaller specimen size of SiO₂, resulting in the incorporation of Cu clamps into the XPS acquisition area. There is no significant difference between the wide-scan spectra of plasma-activated- and Ar-ion-etched SiO₂. Fig. 4-4b shows the high-resolution O_{1s} and Si_{2p} spectra of SiO₂ surfaces treated with O₂ RIE plasma and different storage conditions. The dashed lines and the solid lines in the O_{1s} spectra (Figs. 4-4b, 4-4c, and 4-4d) indicate the Si(-O)₄ and Si(-O)₂ peaks, respectively. Similarly, the dashed lines and solid lines in the Si_{2p} spectra (Figs. 4-4e, 4-4f, 4-4g) indicate the Si(-O)₂ and Si₀ peaks, respectively. In contrast to Si (Fig. 4-1), no considerable binding energy shift and change of FWHM was observed in case of SiO₂ (Fig. 4-4) (detailed curve fitting information are given in Appendix III). This could be due to the negligible surface charging caused by the oxygen RIE plasma-activation in comparison to that of the Si surface. This behavior also relates to the minor variation in the contact angle of SiO₂ [92].

Although the Si(-O)₂ and Si₀ peaks in Si_{2p} spectra are easily distinguishable, there is a hidden peak of Si(-OH)_x in between Si(-O)₄ and Si(-O)₂ peaks in O_{1s} spectra [123]. In order to quantify these three peaks at different plasma-activation and storage conditions,

the O_{1s} spectra were deconvolved using a mixed Gaussian/Lorentzian function with a maximum FWHM of 1 eV. Fig. 4-5 shows a typically deconvolved O_{1s} spectra of as-received SiO_2 consisting of $Si(-O)_2$, $Si(-OH)_x$, and $Si(-O)_4$ [123]. They appeared at 530.36, 531.6, and 533.36eV, respectively.

The summarized amount of $Si(-O)_2$, $Si(-OH)_x$, and $Si(-O)_4$ components from the deconvolved O_{1s} spectra as a function of activation time and storage conditions are shown in Fig. 4-6. Figs. 4-6a to 4-6c correspond to Figs. 4-4b to 4-4d, respectively. A decreasing trend of $Si(-O)_2$ and an increasing trend of $Si(-OH)_x$ and $Si(-O)_4$ are observed with the increase of activation time. The higher amount of $Si(-OH)_x$ in $SiO_2:O_2RIE+20RH$ and $SiO_2:O_2RIE+20D+20RH$ than that of $SiO_2:O_2RIE$ is attributed to its affinity with water molecules from the ambient and relative humidity storage, resulting in higher hydrophilicity. The presence of $Si(-OH)_x$ after plasma-activation, and its increase after relative and ambient humidity treatment, is good for hydrophilic wafer bonding at low temperature [41]. The amount of $Si(-O)_2$ and $Si(-OH)_x$ might have influence on the reduction of hardness of SiO_2 [92] with the increase of O_2 RIE activation time.

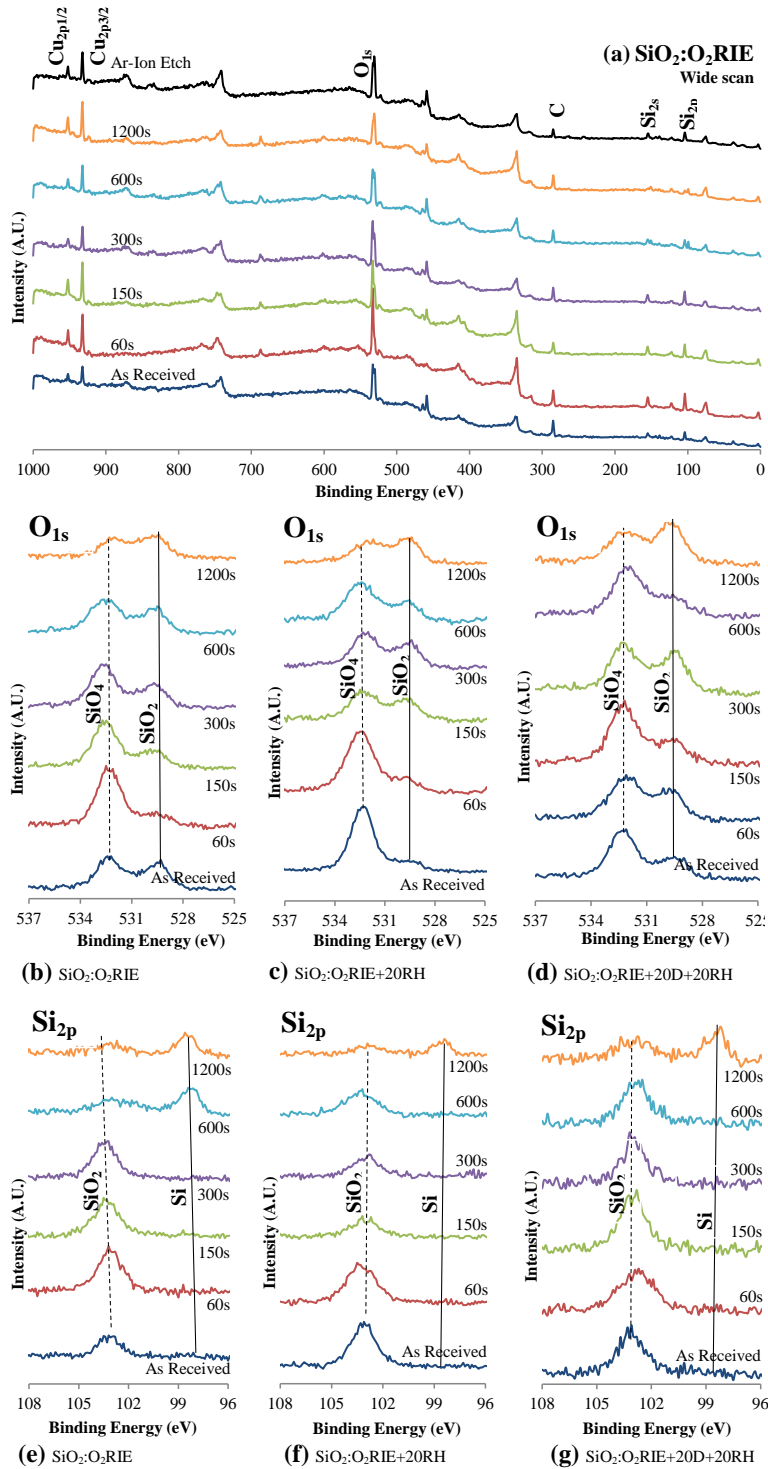


Figure 4-4: (a) XPS wide-scan spectra of SiO₂ before and after O₂ RIE plasma activation. XPS O_{1s} spectra as a function of O₂ RIE plasma activation time for (b) SiO₂ without storing, (c) SiO₂ after storing in 98% relative humidity for 20 days, and (d) SiO₂ after storing in ambient humidity for 20 days, and in 98% relative humidity for 20 days. XPS Si_{2p} spectra as a function of O₂ RIE plasma-activation time for (e) SiO₂ without storing, (f) SiO₂ after storing in 98% relative humidity for 20 days, and (g) SiO₂ after storing in ambient humidity for 20 days, and in 98% relative humidity for 20 days.

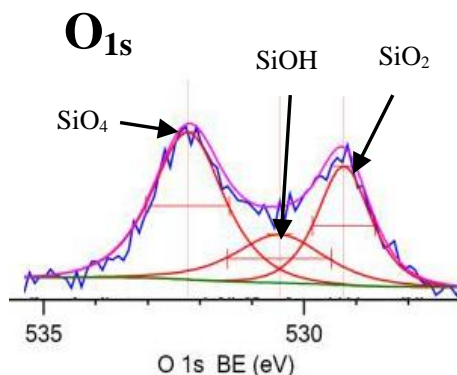


Figure 4-5: Deconvoluted XPS spectra of O_{1s} for as received Si.

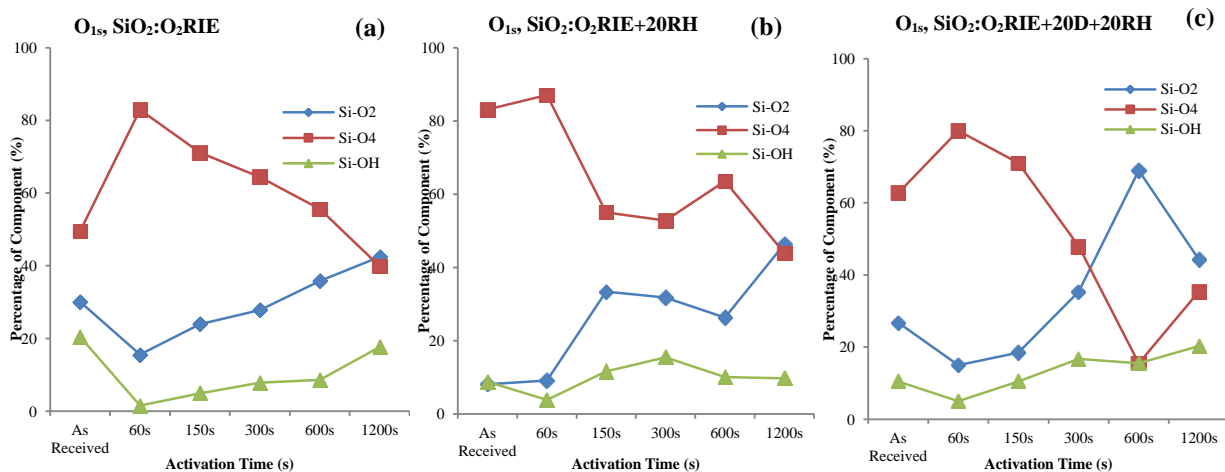


Figure 4-6: Percentage of $Si-(O)_2$, $Si-(O)_4$ and $Si-(OH)_x$ components in O_{1s} XPS spectra of (a) SiO_2 without storing, (b) SiO_2 after storing in 98% relative humidity for 20 days, and (c) SiO_2 after storing in ambient humidity for 20 days and in 98% relative humidity for 20 days.

4.3 Glass

The wide-scan XPS of glass surfaces before and after O₂ RIE plasma-activation (i.e., Glass:O₂RIE) are shown in Fig. 4-7a. Charge correction in this case was also done by shifting the position of the C peak binding energy at 284.0 eV. Before plasma-activation, the as-received glass surface contains three major peaks: Si at ~106 eV, adventitious amorphous carbon at 284 eV, and oxygen at 534 eV [102]. After O₂ RIE plasma-activation, additional peaks are observed at 270, 600, 690, 933, and 953 eV, which are due to Na_{KLL}, Cu_{LVV}, F, Cu_{2p3/2}, and Cu_{2p1/2} respectively [102],[124],[118]. Figs. 4-7b, 4-7c, and 4-7d show the high-resolution XPS spectra of the O_{1s}, Si_{2p} and carbon and other peaks, respectively, for Glass:O₂RIE.

The solid line in Fig. 4-7b shows the O_{1s} peak appeared at 530.5 eV due to oxides which, we believe, is related to oxides of alkaline elements other than Si. This is because the peak does not shift with the increase of O₂ RIE activation times [85]. While the peak is getting stronger after 60 s and 150 s, after that, it becomes weak. Similarly, the intensity of the carbon (~284 eV, Fig. 7d) peak increases at 60 s and then decreases until 1200 s. In fact, while the alkaline oxide peak completely disappears at 1200 s, the C peak still remains. The remaining C at 1200 s may be caused by prolonged irradiation to the glass. Also, the increase of Na_{KLL} peak is evident, which may be indicative of the presence of alkaline oxides. Therefore, the identical behavior both for carbon (~284 eV) and O_{1s} (530.5 eV) peaks supports the presence of alkaline oxides.

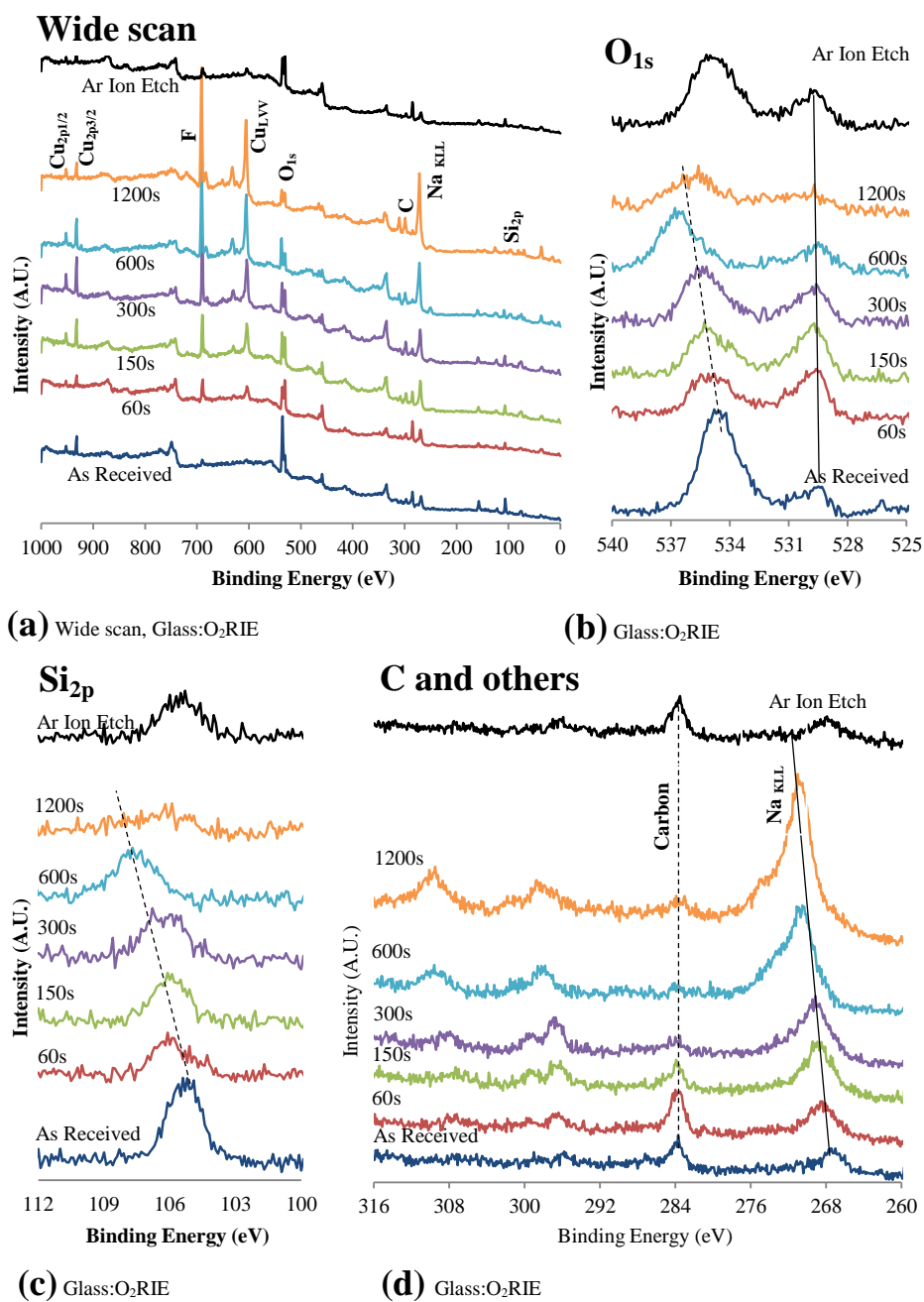


Figure 4-7: (a) XPS wide-scan spectra of glass. (b) XPS O_{1s} spectra of glass after O₂ RIE plasma-activation, (c) XPS Si_{2p} spectra of glass after O₂ RIE plasma-activation, and (d) XPS C_{1s} spectra of glass after O₂ RIE plasma-activation.

The silicon oxides peak (indicated by the dashed line in Fig. 4-7b) shifts to a higher binding energy with increased activation time [85]. The study of Pyrex glass, using quantum cascade laser absorption spectroscopy [125], showed that oxygen plasma-treatment of Pyrex glass materials resulted in a highly oxygen-saturated surface. In a study of the anodic bonding of GaAs and Pyrex glass [126], using sequential plasma activation (i.e., O₂ RIE plasma and N₂ microwave plasma), it was found that the low-frequency Raman peaks were due to alkaline–oxygen–alkaline stretching, Si–O–Si networks, and aluminate networks (Al–O/Al–O–B). After plasma-activation, the intensity of these peaks was enhanced with their shapes unchanged. These results also support the presence of silicon oxides and alkaline oxides. At 1200 s, the silicon oxide peak (~535 eV) becomes weak, similar to the peak at 530.5 eV. The prolonged activation results in an opaque surface due to severe surface damage. The damage increased the surface roughness by 100 times compared to that of the as-received surface [92]. The high surface roughness may be attributed mainly due to the oxidation of the alkaline elements of the glass during prolonged O₂ RIE activation. Thus, lower activation time is suitable for better bondability in glass-based wafer bonding [41].

The peak for the as-received surface at ~106 eV is assigned by Si_{2p} (Fig. 4-7c). The peak broadens after O₂ RIE activation at different times, and shifts to a higher energy due to the oxidation of Si. The deconvolution of the broadened peaks, using mixed Gaussian-Lorentzian curve fitting, revealed two peaks consisting of silicon-dioxide and suboxides [127]. In fact, at 1200 s the silicon-dioxide and suboxides peaks almost completely

disappear. After Ar-ion-etching of the as-received specimen, the Si_{2p} peak appears at a binding energy lower than that of the O₂ RIE plasma-treated surface, but identical to that of as-received surface. Therefore, the comparison between the as-received, O₂ RIE-treated, and Ar-ion-etched surfaces indicates that the O₂ RIE results in silicon-dioxide and suboxides on glass. A comparison in the change of the surface chemical properties of the specimens with increases in activation times is summarized in Table 4-2.

Table 4-2: Evolution of Surface properties with the increase of oxygen plasma activation times at different storage conditions.

Surface Treatment	Change in surface chemical properties with the increase of activation times (60, 150, 300, and 600 s) under different storage conditions			
	Shift in the Binding Energy	Amount of Si(-O) ₂	Amount of Si(-OH) _x	Bondability
Si:O ₂ RIE	High	Increase	High until 150 s activation time	Better at lower activation time [92][20][45]
Si:O ₂ RIE+20RH	Low	Increase	Increase	Good at lower activation
Si:O ₂ RIE+20D+20RH	Low	Increase	Increase	Good at lower activation
SiO ₂ :O ₂ RIE	Negligible	Decrease	Increase	Better at lower activation time
SiO ₂ :O ₂ RIE+20RH	Negligible	Decrease	Increase	Better at lower activation time
SiO ₂ :O ₂ RIE+20D+20RH	Negligible	Decrease	Increase	Good at lower activation
Glass:O ₂ RIE	Only for Si-based oxides	-	-	Better at low activation time

4.4 Conclusions

The X-ray Photoelectron Spectroscopy (XPS) of silicon (Si), silicon dioxide (SiO₂), and glass was studied after treatment in oxygen-reactive ion-etching plasma, followed by

exposure in relative and ambient humidity. Wide-scan XPS of Si and SiO₂ showed Si_{2p}, Si_{2s}, C, and O_{1s} peaks before plasma activation. XPS of glass also showed the same peaks with an additional peak of sodium. An increase of O_{1s} peak intensity with increased plasma-activation time was also observed. An unwanted peak of fluorine was observed only in Si and glass. This fluorine is due to physisorbed or chemisorbed contaminant from the wafer cleaning using hydrofluoric acid.

High-resolution XPS spectra of Si before and after O₂ RIE plasma treatment showed that Si(-O)₂ shifted to a higher binding energy. This shift in the binding energy is correlated with the high surface reactivity of Si. This high surface reactivity plays a significant role in the hydrophilic bonding of Si-based substrates. After storage of the activated Si wafers in humidity, significant overlap of silicon oxide (i.e., Si(-O)₂) and silanol groups (i.e., Si(-OH)_x) was observed. Also, a considerable coverage of silanol groups was evident after storage in the ambient and relative humidity. The increased coverage of silanol groups suggests that hydrophilic Si surfaces have higher interaction with water molecules. The variation of Si(-O)₂ and Si(-OH)_x components at different activation times were explained by crystal-orientation-dependent surface roughness and oxidation rates. Conversely, this explanation might prove wrong if the least reactive crystal planes (e.g., (111)) are exposed and cause decreased oxidation. However, the increased amount of Si(-OH)_x below 300 s activation time is good for bonding with low temperature heating.

In contrast to Si, the high insulating properties of SiO₂ caused an insignificant shift in the binding energy of the high-resolution XPS of SiO₂. Yet, the substantial presence of Si(-

Chapter 4. Surface Chemical Analysis

O_2 and an increase of $Si(-OH)_x$ was observed due to oxygen plasma oxidation and humidity storage. These results are favorable for hydrophilic wafer bonding.

Finally, the oxygen RIE plasma-activation of glass showed oxide peaks for Si and other alkaline materials. Plasma-oxidation-induced oxides and sub-oxides of Si also appeared. The physical damage caused by prolonged activation created an opaque glass surface and high surface roughness. Thus, lower activation times are good for glass based bonding.

CHAPTER 5.

CONCLUSIONS AND FUTURE WORK

5.1 Conclusions

The water contact angle, roughness, hardness, and elemental and compositional states of oxygen reactive-ion etching (O_2 RIE), plasma-activated silicon (Si), silicon dioxide (SiO_2), and glass surfaces were investigated with or without storage in ambient and 98% relative humidity. The surface roughness for Si was increased with the increase of plasma-activation time, and it was higher than that of SiO_2 . The surface roughness of the activated Si was reduced after treating with humidity and air, but no considerable change was observed in SiO_2 . The reduced roughness of Si is due to the higher accumulation of

Chapter 5. Conclusions and Future Work

water molecules on the surface. The significant increase of roughness of glass at 1200 s is due to the surface damage. The low surface roughness at lower activation times is suitable for direct wafer bonding.

The oxygen plasma-activated Si showed a lower contact angle than that of the as-received Si, which increased with activation time. Also, Si and SiO₂ showed high surface reactivity after plasma activation, which was considerably reduced after storage in ambient and relative humidity. The contact angle of the plasma-activated Si and SiO₂ surfaces was decreased due to the augmented OH groups in relative and ambient humidity. Moreover, plasma-activated glass showed hydrophilic properties and a highly reactive surface, resulting in contact angles below 2°, which is beyond the detection limit of the equipment. The high hydrophilicity and surface reactivity at lower activation times can result in better bondability. Also, the high hydrophilicity after ambient humidity treatment may have good bondability, provided that the surface contains OH groups.

The hardness of Si was decreased with increased activation time due to higher surface roughness and the formation of amorphous layers of Si. A considerable reduction in the hardness of the plasma-activated glass at 1200 s was observed due to the highly increased surface roughness. Furthermore, the relative- and ambient-humidity-storage-induced variation was observed in Si and SiO₂. This dependence of the hardness is thought to be due to the quality of the complex formation of the absorbents (e.g., -OH), deposited layers (e.g., carbon), oxides (i.e., Si-OH), and sub-oxides (i.e., Si-O₂, Si-O₄) on the

surface. Although high surface hardness is observed at low activation times (i.e., high bondability regions), the role of hardness on bondability needs further investigation.

Before plasma activation, wide-scan XPS of Si and SiO₂ showed Si_{2p}, Si_{2s}, C, and O_{1s} peaks, and glass showed the same peaks plus an additional peak of sodium. The O₂ RIE plasma showed an increase of O_{1s} peak intensity with increased plasma activation time. High-resolution XPS spectra of Si before and after O₂ RIE plasma treatment showed that Si(-O)₂ shifted to a higher binding energy, which could be correlated with the high surface reactivity of Si. This high surface reactivity is required for the hydrophilic bonding of Si-based substrates. Considerable coverage of silanol groups was evident after storage in the relative and ambient humidity. Increased coverage of silanol groups is indicative of the interaction of water molecules with the hydrophilic Si surfaces. Crystal-orientation-dependent surface roughness and oxidation rates were explained with the variation of Si(-O)₂ and Si(-OH)_x components at different activation times, although the least reactive crystal planes (e.g., (111)) might have decreased oxidation. However, the increased amount of Si(-OH)_x below 300 s activation time is good for bonding with low temperature heating.

Unlike Si, the high-resolution XPS of SiO₂ showed an insignificant shift in binding energy, which is attributable to its high insulating properties. However, the presence of Si(-O)₂ due to oxygen plasma-oxidation, and the increase of Si(-OH)_x due to humidity storage was observed, which is good for hydrophilic wafer bonding.

Chapter 5. Conclusions and Future Work

Oxygen plasma-activation of glass showed oxide peaks due to Si and other alkalines. Also, the silicon oxides and sub-oxides appeared due to plasma oxidation. Prolonged activation resulted in an opaque glass surface and high surface roughness due to surface damage. Thus, glass-based bonding is good at lower activation times.

5.2 Future Work

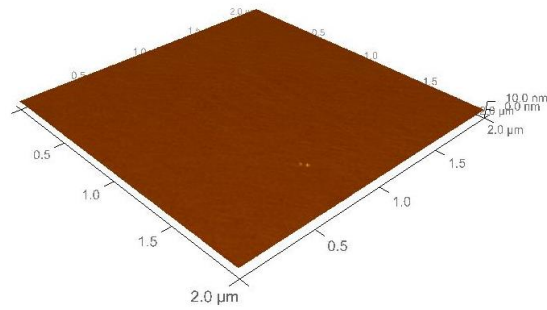
In this thesis, O₂ RIE plasma has been used for investigating the bondability of Si, SiO₂, and glass surfaces with or without storage in ambient and 98% relative humidity. Our previous study showed that O₂ RIE plasma followed by microwave radical plasma (known as Sequential Plasma Activation) results in higher hydrophilic and reactive surfaces than in the O₂ RIE. Therefore, the potential areas of future research may be described as follows:

1. Investigation of surface properties of materials due to Sequential Plasma Activation.
2. Investigation of surface properties of polymer materials due to different plasma activation and other environmental effects.
3. Further investigation on the role of hardness on bondability.
4. Investigation of the bonded interface characteristics with nondestructive techniques such as Scanning Acoustic Microscopy, Fourier Transform Infrared spectroscopy, and Raman Spectroscopy.

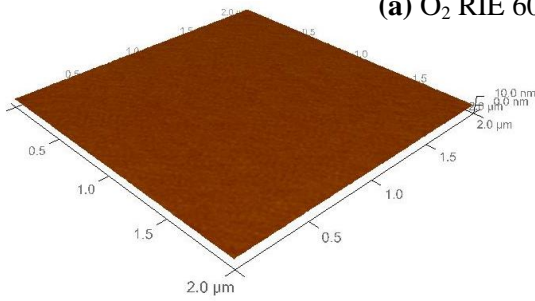
5. Investigation of surface properties for semiconductor/polymer, polymer/metal bonding for MEMS and biomedical applications.
6. Investigation of surface properties of new materials and composites, such as graphene, graphene-metal, and polymers with carbon nanotubes for high-performance environmental and biomedical systems.

APPENDIX I

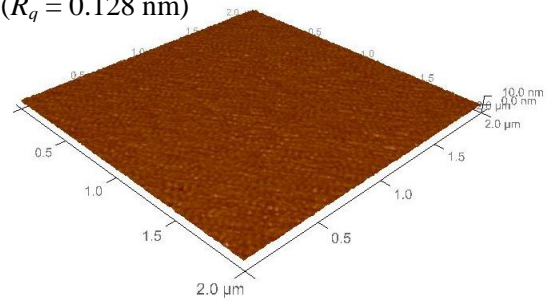
AFM IMAGES OF Si AFTER O₂ RIE PLASMA-ACTIVATION AND 20 DAYS OF STORAGE IN 98% RH HUMIDITY



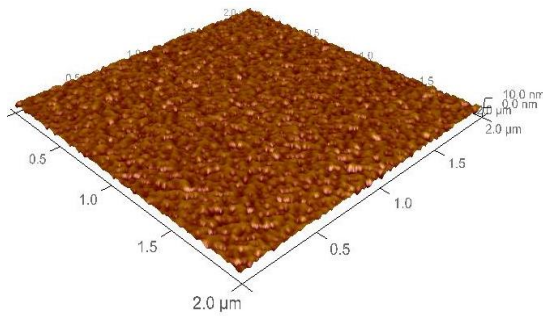
(a) O₂ RIE 60 s ($R_q = 0.128$ nm)



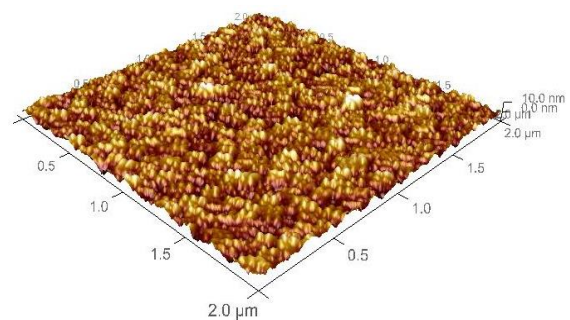
(b) O₂ RIE 150 s ($R_q = 0.197$ nm)



(c) O₂ RIE 300 s ($R_q = 0.391$ nm)

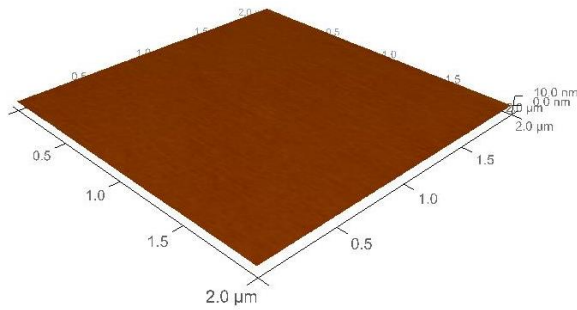


(d) O₂ RIE 600 s ($R_q = 1.176$ nm)

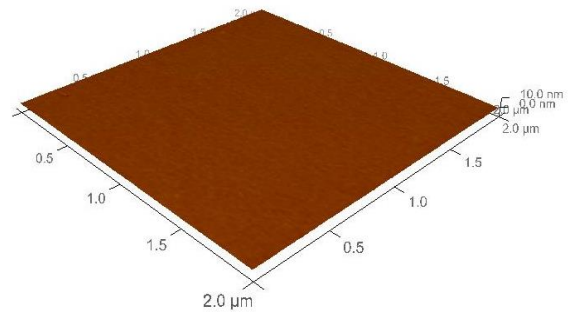


(e) O₂ RIE 1200 s ($R_q = 2.343$ nm)

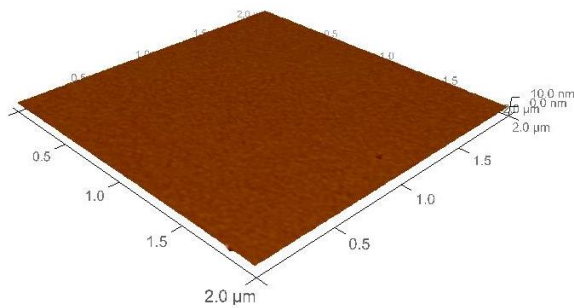
AFM IMAGES OF Si AFTER O₂ RIE PLASMA-ACTIVATION FOLLOWED BY 20 DAYS OF STORAGE IN CLEANROOM AMBIENT HUMIDITY AND 20 DAYS OF STORAGE IN 98% RH HUMIDITY



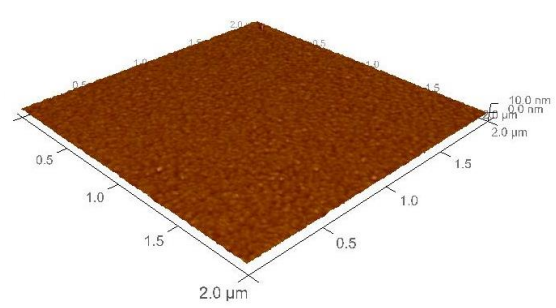
(a) As-received ($R_q = 0.12$ nm)



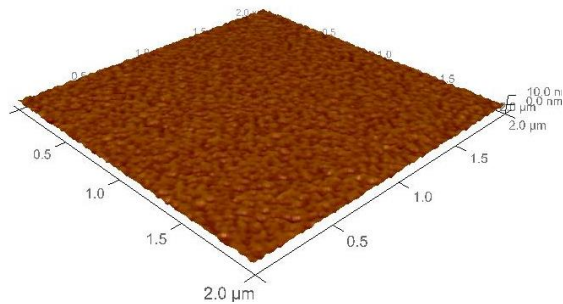
(b) O₂ RIE 60 s ($R_q = 0.138$ nm)



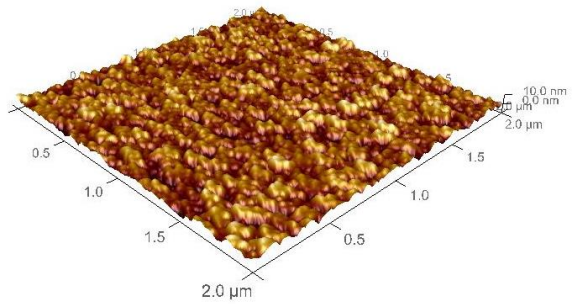
(c) O₂ RIE 150 s ($R_q = 0.211$ nm)



(d) O₂ RIE 300 s ($R_q = 0.48$ nm)



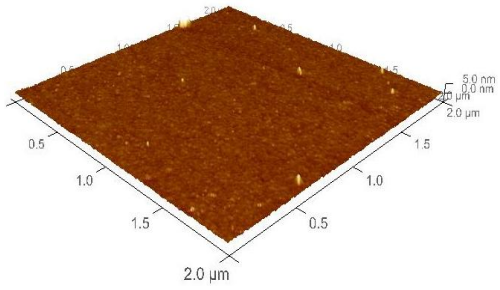
(e) O₂ RIE 600 s ($R_q = 0.60$ nm)



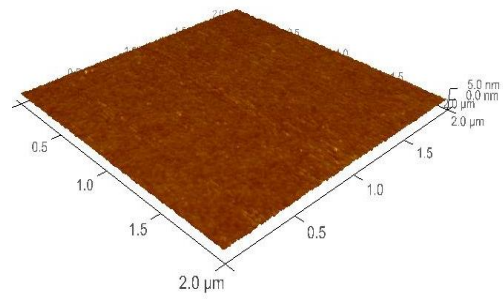
(f) O₂ RIE 1200 s ($R_q = 2.23$ nm)

APPENDIX I

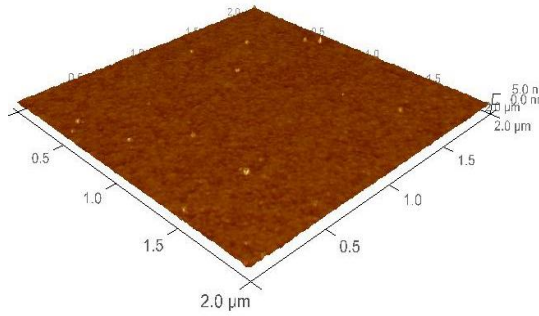
AFM IMAGES OF SiO₂ AFTER O₂ RIE PLASMA-ACTIVATION



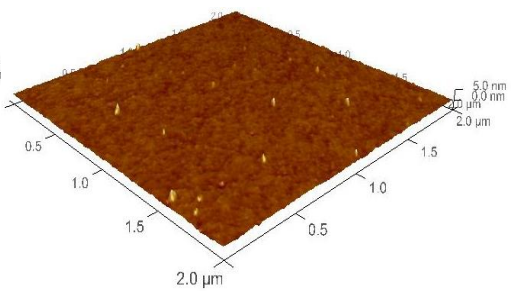
(a) As-received SiO₂ ($R_q = 0.22$ nm)



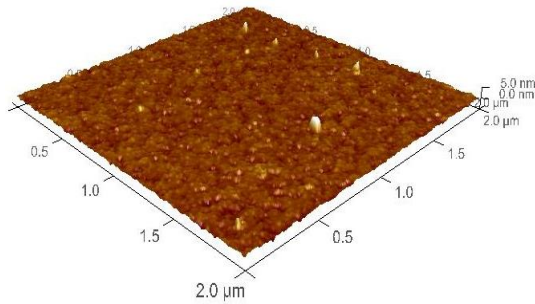
(b) O₂ RIE 60 s ($R_q = 0.17$ nm)



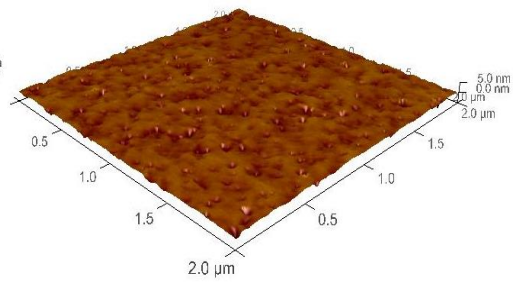
(c) O₂ RIE 150 s ($R_q = 0.20$ nm)



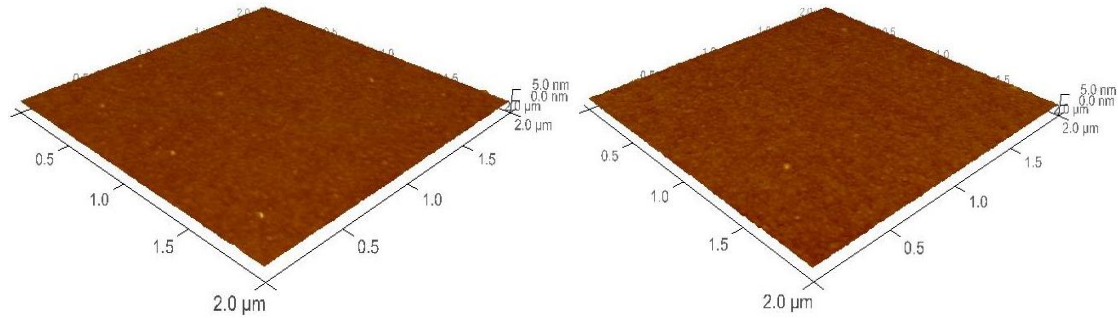
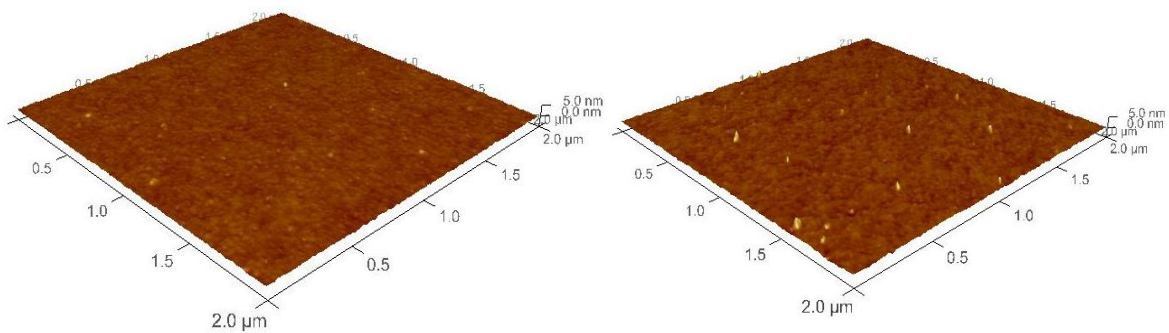
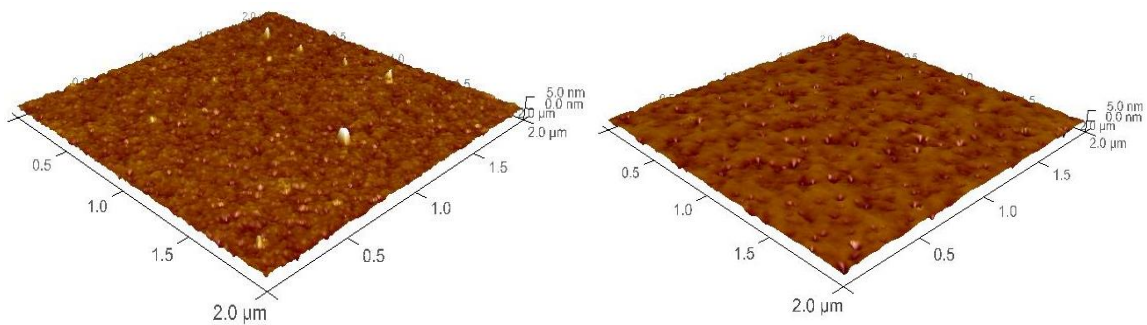
(d) O₂ RIE 300 s ($R_q = 0.26$ nm)



(e) O₂ RIE 600 s ($R_q = 0.38$ nm)

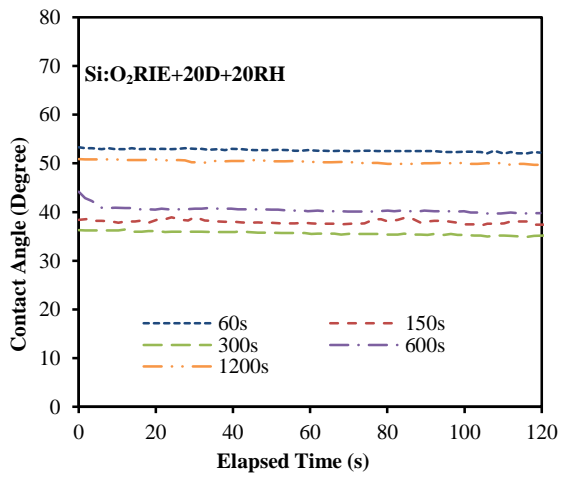
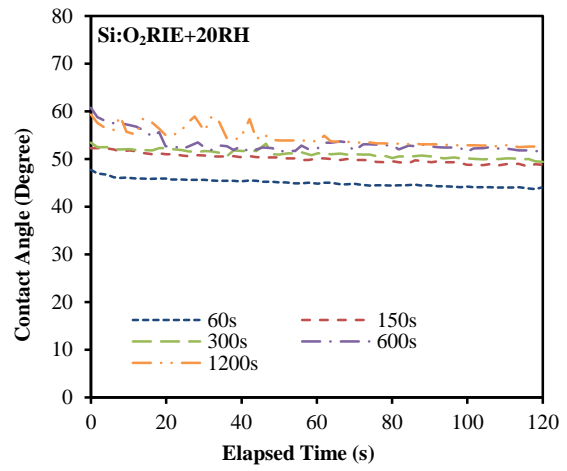
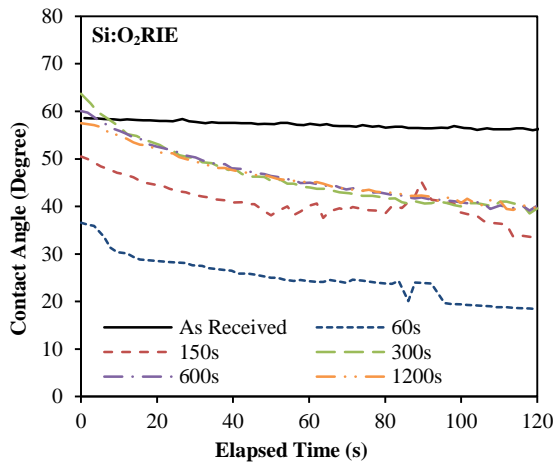


(f) O₂ RIE 1200 s ($R_q = 0.44$ nm)

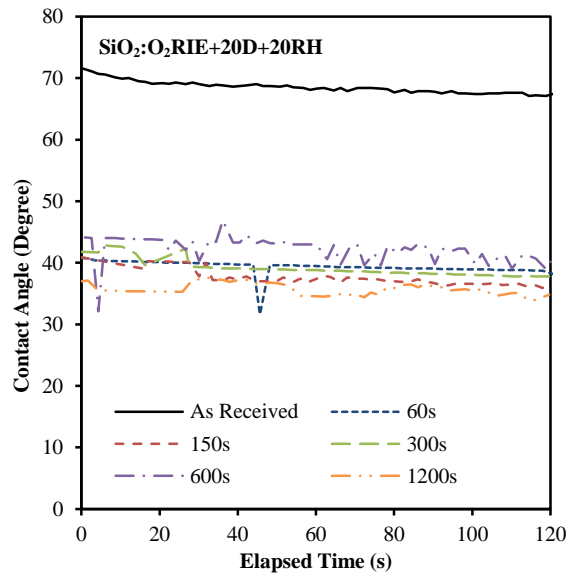
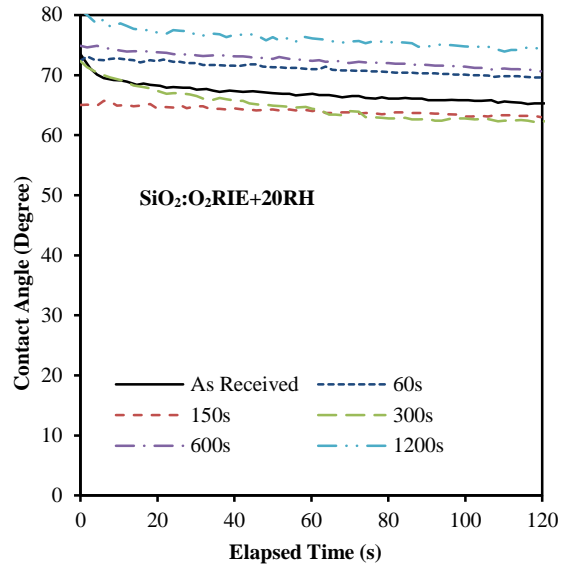
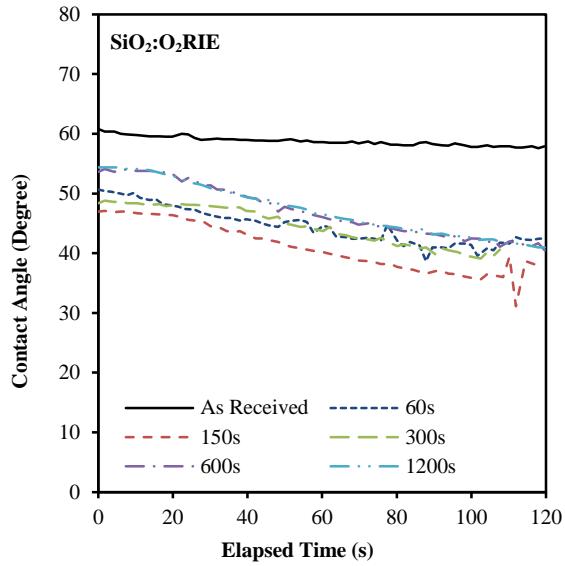
AFM IMAGES OF SiO₂ AFTER O₂ RIE PLASMA ACTIVATION AND 20 DAYS OF STORAGE IN 98% RH HUMIDITY**(a)** As-received SiO₂ ($R_q = 0.15$ nm)**(b)** O₂ RIE 60 s ($R_q = 0.17$ nm)**(c)** O₂ RIE 150 s ($R_q = 0.21$ nm)**(d)** O₂ RIE 300 s ($R_q = 0.25$ nm)**(e)** O₂ RIE 600 s ($R_q = 0.35$ nm)**(f)** O₂ RIE 1200 s ($R_q = 0.41$ nm)

APPENDIX II

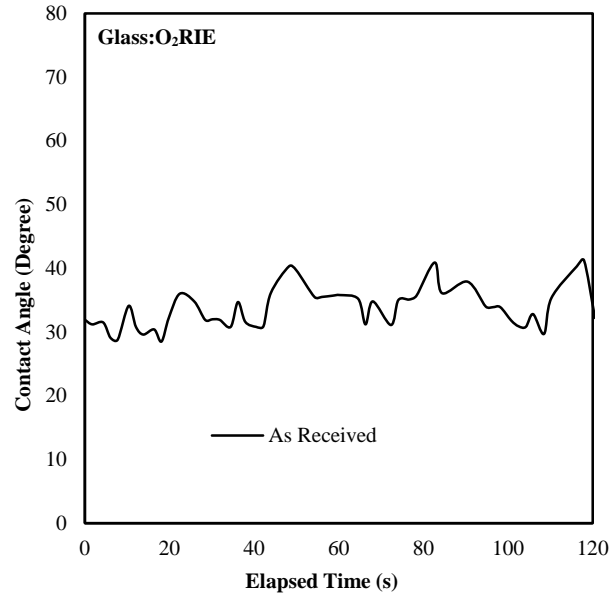
CONTACT ANGLE VERSUS ELAPSED TIME FOR Si

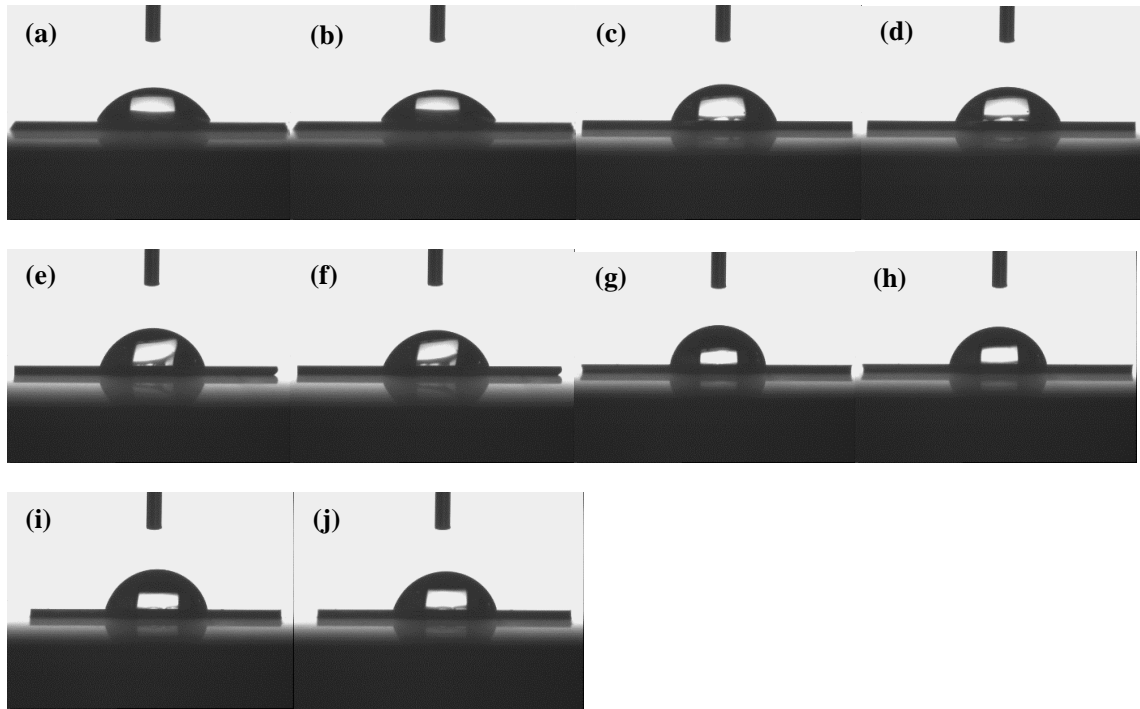


CONTACT ANGLE VERSUS ELAPSED TIME FOR SiO₂

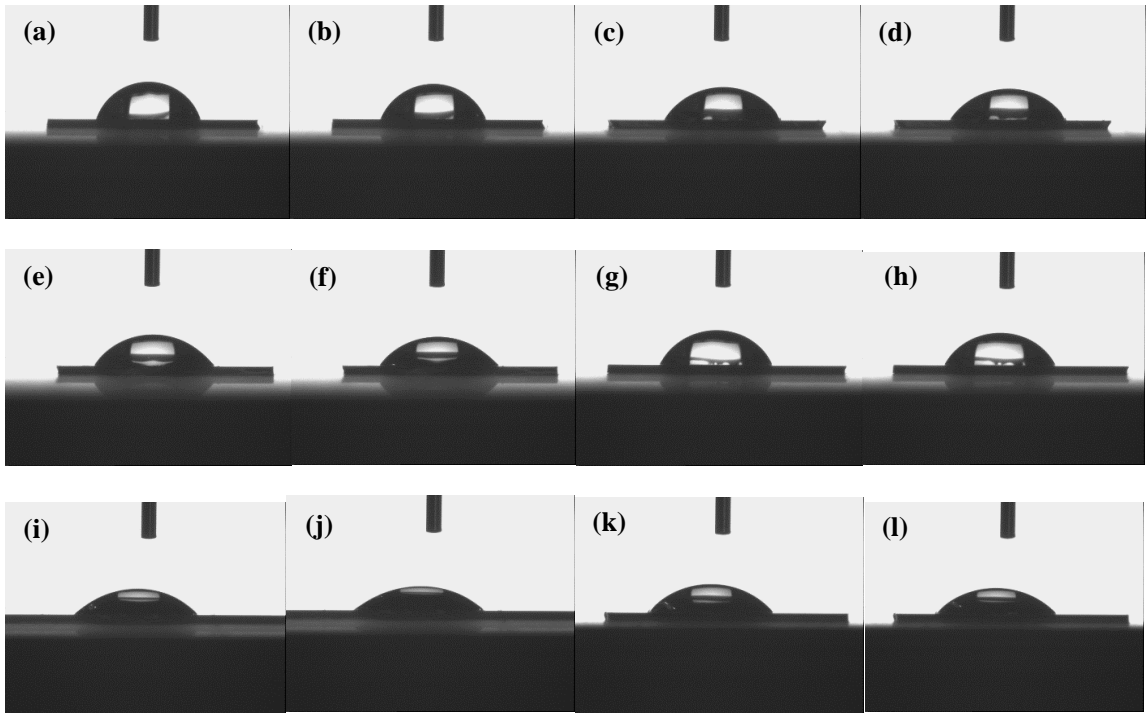


CONTACT ANGLE VERSUS ELAPSED TIME FOR GLASS

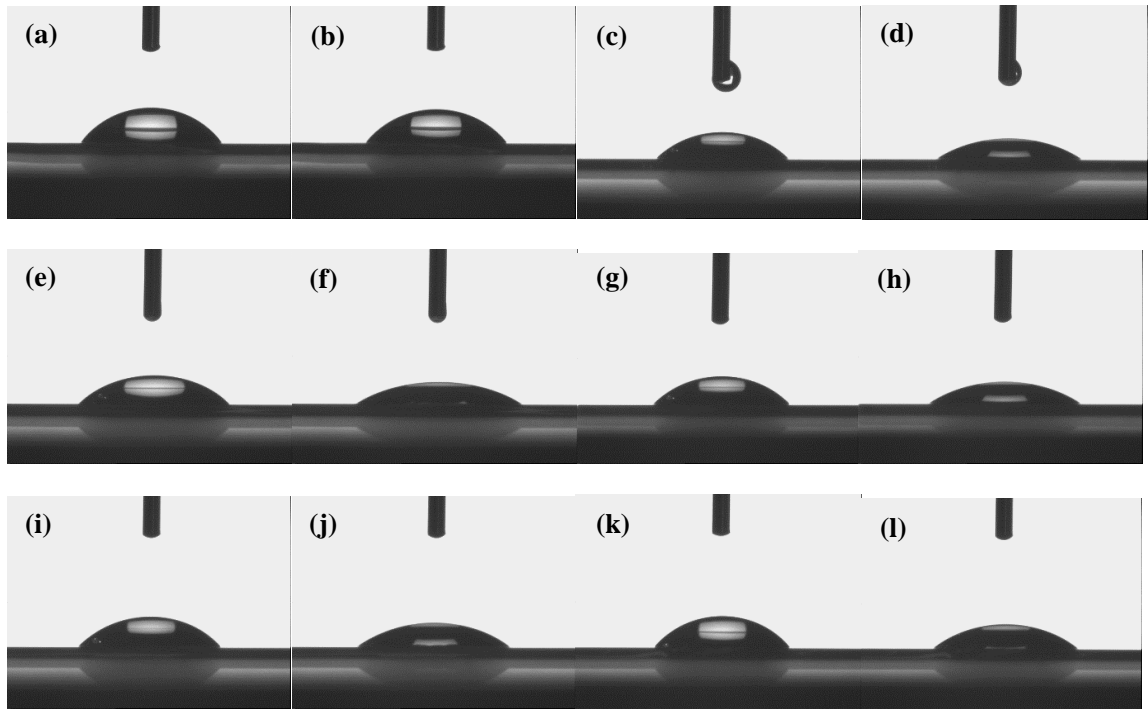


DROP SHAPE IMAGES OF Si:O₂RIE+20RH

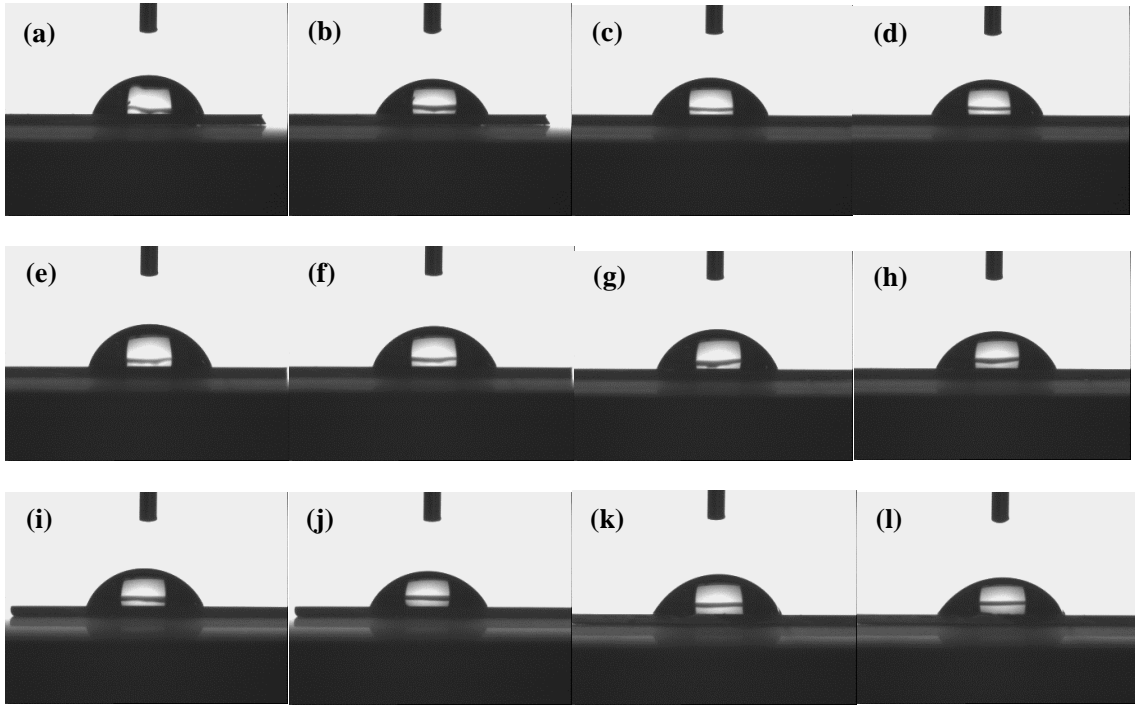
Drop shape of water immediately after putting the drop on Si:O₂RIE+20RH at (a) 60 s, (c) 150 s, (e) 300 s, (g) 600 s, and (i) 1200 s. Drop shape of water after 2 minutes of putting the drop on Si:O₂RIE+20RH at (b) 60 s, (d) 150 s, (f) 300 s, (h) 600 s, and (j) 1200 s.

DROP SHAPE IMAGES OF Si:O₂RIE+20D+20RH

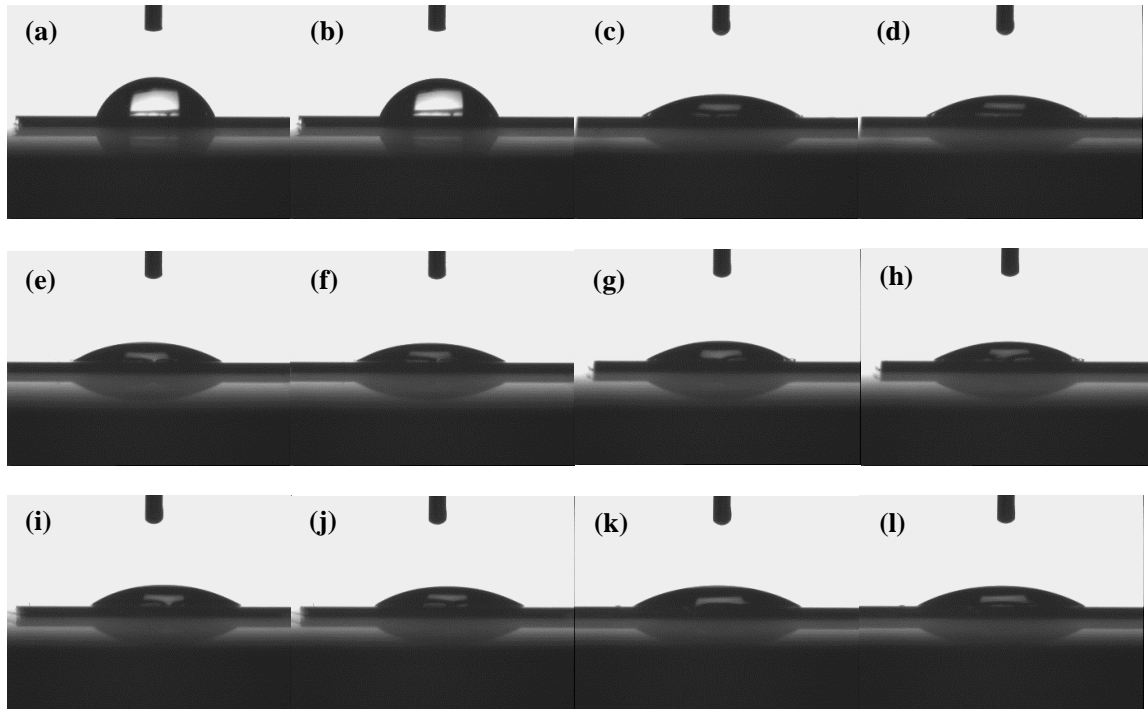
Drop shape of water immediately after putting the drop on Si:O₂RIE+20D+20RH at (a) as-received (c) 60 s, (e) 150 s, (g) 300 s, (i) 600 s and (k) 1200 s. Drop shape of water after 2 minutes of putting the drop on Si:O₂RIE+20D+20RH at (b) as-received, (d) 60 s, (f) 150 s, (h) 300 s, (j) 600 s, and (l) 1200 s.

DROP SHAPE IMAGES OF SiO₂:O₂RIE

Drop shape of water immediately after putting the drop on SiO₂:O₂RIE at (a) as-received, (c) 60 s, (e) 150 s, (g) 300 s, (i) 600 s, and (k) 1200 s. Drop shape of water after 2 minutes of putting the drop on SiO₂:O₂RIE at (b) as-received, (d) 60 s, (f) 150 s, (h) 300 s, (j) 600 s, and (l) 1200 s.

DROP SHAPE IMAGES OF Si:O₂RIE+20RH

Drop shape of water immediately after putting the drop on SiO₂:O₂RIE+20RH at (a) as-received, (c) 60 s, (e) 150 s, (g) 300 s, (i) 600 s, and (k) 1200 s. Drop shape of water after 2 minutes of putting the drop on SiO₂:O₂RIE+20RH at (b) as-received, (d) 60 s, (f) 150 s, (h) 300 s, (j) 600 s, and (l) 1200 s.

DROP SHAPE IMAGES OF $\text{SiO}_2:\text{O}_2\text{RIE}+20\text{D}+20\text{RH}$ 

Drop shape of water immediately after putting the drop on $\text{SiO}_2:\text{O}_2\text{RIE}+20\text{D}+20\text{RH}$ at (a) as-received, (c) 60 s, (e) 150 s, (g) 300 s, (i) 600 s, and (k) 1200 s. Drop shape of water after 2 minutes of putting the drop on $\text{SiO}_2:\text{O}_2\text{RIE}+20\text{D}+20\text{RH}$ at (b) as-received, (d) 60 s, (f) 150 s, (h) 300 s, (j) 600 s, and (l) 1200 s.

APPENDIX III

TABLE 1: CURVE FITTING RESULTS OF O_{1s} OF Si:O₂RIE

Si:O ₂ RIE	Component	Centre (eV)	Intensity (cps)	FWHM (eV)	Area (cps*eV)	Ratio (%)
As-received	Si-O ₂	531.972	2680.45	0.6	350.716	66.5351
	Si-(OH) _x	531.127	907.53	0.5	98.9528	18.7725
	Si-O ₄	532.946	710.281	0.5	77.4456	14.6924
60 s	Si-O ₂	532.689	2157.08	0.7	329.277	76.5628
	Si-(OH) _x	531.584	527.024	0.7	80.4486	18.7057
	Si-O ₄	533.512	311.041	0.3	20.3487	4.73143
150 s	Si-O ₂	532.831	4731.67	0.75	773.878	89.237
	Si-(OH) _x	531.7	592.222	0.6	77.4876	8.93521
	Si-O ₄	533.801	363.436	0.2	15.8509	1.82779
300 s	Si-O ₂	532.917	5266.72	0.8	918.813	94.2056
	Si-(OH) _x	531.658	433.457	0.4	37.8096	3.87661
	Si-O ₄	533.594	214.431	0.4	18.7044	1.91776
600 s	Si-O ₂	533.119	5161.93	0.75	844.248	93.6524
	Si-(OH) _x	532.133	369.676	0.5	40.3077	4.47134
	Si-O ₄	533.74	193.905	0.4	16.914	1.87627
1200 s	Si-O ₂	533.55	5314.62	0.75	869.221	90.3811
	Si-(OH) _x	532.564	432.392	0.6	56.5751	5.88265
	Si-O ₄	534.577	329.549	0.5	35.9325	3.73624

TABLE 2: CURVE FITTING RESULTS OF O_{1s} OF Si:O₂RIE+20RH

Si:O ₂ RIE +20RH	Component	Centre (eV)	Intensity (cps)	FWHM (eV)	Area (cps*eV)	Ratio (%)
60 s	Si-O ₂	532.261	2829.66	0.7	431.945	69.5726
	Si-(OH) _x	531.07	899.906	0.7	137.37	22.1259
	Si-O ₄	533.236	472.69	0.5	51.5399	8.30144
150 s	Si-O ₂	532.102	2344.57	0.75	383.46	74.4924
	Si-(OH) _x	531.087	717.038	0.5	78.1824	15.188
	Si-O ₄	533.15	487.197	0.5	53.1216	10.3196
300 s	Si-O ₂	532.74	5002.24	0.7	763.589	73.492
	Si-(OH) _x	531.916	1351.34	0.5	147.343	14.1811
	Si-O ₄	533.44	1174.64	0.5	128.078	12.3269
600 s	Si-O ₂	532.89	5176	0.7	790.112	71.5989
	Si-(OH) _x	532.092	1667.69	0.6	218.205	19.7734
	Si-O ₄	533.824	873.19	0.5	95.2084	8.62766
1200 s	Si-O ₂	532.916	6087.49	0.7	929.251	77.3292
	Si-(OH) _x	532.05	1921.4	0.5	209.5	17.4339
	Si-O ₄	533.688	577.164	0.5	62.9312	5.23693

TABLE 3: CURVE FITTING RESULTS OF O_{1s} OF Si:O₂RIE+20D+20RH

Si:O₂RIE +20D +20RH	Component	Centre (eV)	Intensity (cps)	FWHM (eV)	Area (cps*eV)	Ratio (%)
As-received	Si-O ₂	532.042	3240.68	0.7	494.687	72.9351
	Si-(OH) _x	531.203	830.91	0.6	108.718	16.029
	Si-O ₄	533.1	572.074	0.6	74.8514	11.0359
60 s	Si-O ₂	532.626	4671.99	0.7	713.176	73.8353
	Si-(OH) _x	531.651	1264.18	0.6	165.408	17.1247
	Si-O ₄	533.438	800.821	0.5	87.3177	9.04002
150 s	Si-O ₂	532.653	3815.66	0.7	582.458	59.0395
	Si-(OH) _x	531.963	1883.12	0.7	287.457	29.1375
	Si-O ₄	533.357	1069.75	0.5	116.641	11.823
300 s	Si-O ₂	532.585	3516.52	0.7	536.794	65.1199
	Si-(OH) _x	531.8	1574.25	0.6	205.978	24.9877
	Si-O ₄	533.357	747.872	0.5	81.5444	9.89236
600 s	Si-O ₂	532.759	4527.47	0.7	691.115	65.4673
	Si-(OH) _x	531.988	1951.35	0.6	255.318	24.1856
	Si-O ₄	533.625	1001.79	0.5	109.231	10.3471
1200 s	Si-O ₂	532.77	5901.45	0.7	900.853	76.7192
	Si-(OH) _x	531.903	1838.51	0.5	200.462	17.072
	Si-O ₄	533.582	835.805	0.4	72.9057	6.20886

TABLE 4: CURVE FITTING RESULTS OF Si_{2p} OF Si:O₂RIE

Si:O ₂ RIE	Component	Centre (eV)	Intensity (cps)	FWHM (eV)	Area (cps*eV)	Ratio (%)
As-received	Si	98.903	2464.47	0.4	214.971	57.597
	Si-(OH) _x	99.495	984.327	0.4	85.861	23.0046
	Si-O ₂	102.6	474.3	0.7	72.4014	19.3984
60 s	Si	98.958	2699.8	0.6	353.247	71.8912
	Si-(OH) _x	99.572	764.483	0.3	50.0133	10.1785
	Si-O ₂	103.6	404.307	1	88.1032	17.9303
150 s	Si	99.0322	2818	0.5	307.261	59.4529
	Si-(OH) _x	99.7	580.487	0.4	50.6348	9.79748
	Si-O ₂	103.7	809.744	0.9	158.918	30.7496
300 s	Si	98.9773	2540.09	0.5	276.959	55.6267
	Si-(OH) _x	99.5	578.064	0.4	50.4235	10.1275
	Si-O ₂	103.85	977.36	0.8	170.506	34.2459
600 s	Si	98.9856	2020.93	0.4	176.282	37.6284
	Si-(OH) _x	99.5	756.322	0.4	65.9726	14.0822
	Si-O ₂	104	1296.76	0.8	226.227	48.2894
1200 s	Si	98.9752	1720.96	0.4	150.117	34.2264
	Si-(OH) _x	99.664	450.62	0.4	39.3068	8.96191
	Si-O ₂	104.368	1038.76	1.1	249.175	56.8117

TABLE 5: CURVE FITTING RESULTS OF Si_{2p} OF Si:O₂RIE+20RH

Si:O ₂ RIE +20RH	Component	Centre (eV)	Intensity (cps)	FWHM (eV)	Area (cps*eV)	Ratio (%)
60 s	Si	98.9818	1614.79	0.5	176.069	50.4873
	Si-(OH) _x	99.78	420.367	0.5	45.8348	13.143
	Si-O ₂	102.091	582.101	1	126.835	36.3697
150 s	Si	99.05	2048.85	0.6	268.076	72.8967
	Si-(OH) _x	100.139	249.779	0.5	27.2347	7.40581
	Si-O ₂	102.295	333.032	1	72.4369	19.6974
300 s	Si	99.1047	1443.98	0.5	157.444	39.1248
	Si-(OH) _x	99.724	430.508	0.3	28.1643	6.99883
	Si-O ₂	103.381	995.051	1	216.806	53.8763
600 s	Si	99.05	1329.4	0.5	144.952	40.9142
	Si-(OH) _x	99.629	243.099	0.4	21.2051	5.98536
	Si-O ₂	103.501	958.789	0.9	188.126	53.1005
1200 s	Si	99.0744	1143.41	0.5	124.672	31.8343
	Si-(OH) _x	99.658	425.278	0.4	37.0962	9.47234
	Si-O ₂	103.482	1171.19	0.9	229.859	58.6934

TABLE 6: CURVE FITTING RESULTS OF Si_{2p} OF Si:O₂RIE+20D+20RH

Si:O ₂ RIE +20D +20RH	Component	Centre (eV)	Intensity (cps)	FWHM (eV)	Area (cps*eV)	Ratio (%)
As-received	Si	99	2045.53	0.4	178.428	50.4591
	Si-(OH) _x	99.651	880.384	0.4	76.7943	21.7173
	Si-O ₂	102.533	501.758	0.9	98.3867	27.8236
60 s	Si	99.0456	1752.28	0.4	152.848	36.4962
	Si-(OH) _x	99.653	888.914	0.4	77.5383	18.5142
	Si-O ₂	103.262	864.574	1	188.419	44.9897
150 s	Si	99	1689.16	0.6	221.013	49.2998
	Si-(OH) _x	99.701	522.083	0.4	45.5404	10.1583
	Si-O ₂	103.25	833.789	1	181.751	40.5419
300 s	Si	99.0694	2110.64	0.4	184.107	48.198
	Si-(OH) _x	99.76	817.291	0.4	71.2908	18.6635
	Si-O ₂	103.179	645.085	0.9	126.583	33.1385
600 s	Si	99.1029	1525.93	0.5	166.38	44.2441
	Si-(OH) _x	99.746	493.375	0.4	43.0362	11.4442
	Si-O ₂	103.343	849.063	0.9	166.634	44.3116
1200 s	Si	99.0171	1473.37	0.4	128.519	32.9986
	Si-(OH) _x	99.672	621.981	0.4	54.2542	13.9304
	Si-O ₂	103.4	1053.5	0.9	206.695	53.071

TABLE 7: CURVE FITTING RESULTS OF O_{1s} OF SiO₂:O₂RIE

SiO ₂ :O ₂ RIE +20D +20RH	Component	Centre (eV)	Intensity (cps)	FWHM (eV)	Area (cps*eV)	Ratio (%)
As-received	Si-O ₂	530.366	2095.96	0.6	274.24	30.0397
	Si-O ₄	533.361	2595.35	0.8	452.775	49.596
	Si-(OH) _x	531.6	852.527	1	185.911	20.3643
60 s	Si-O ₂	530.52	882.378	0.8	153.936	15.5523
	Si-O ₄	533.295	4705.11	0.8	820.835	82.9295
	Si-(OH) _x	531.753	68.9093	1	15.0271	1.5182
150 s	Si-O ₂	530.74	1275.37	0.8	222.496	23.9413
	Si-O ₄	533.537	3788.54	0.8	660.935	71.1188
	Si-(OH) _x	531.9	233.914	0.9	45.9088	4.93994
300 s	Si-O ₂	530.674	1766.54	0.7	269.661	27.7722
	Si-O ₄	533.648	3585.79	0.8	625.564	64.4265
	Si-(OH) _x	531.9	434.198	0.8	75.7485	7.80129
600 s	Si-O ₂	530.608	1928.89	0.8	336.507	35.7927
	Si-O ₄	533.559	2664.53	0.9	522.95	55.6239
	Si-(OH) _x	531.8	462.563	0.8	80.697	8.58338
1200 s	Si-O ₂	530.586	1511.25	0.8	263.646	42.467
	Si-O ₄	533.1	1261.4	0.9	247.567	39.877
	Si-(OH) _x	531.753	502.65	1	109.613	17.656

TABLE 8: CURVE FITTING RESULTS OF O_{1s} OF SiO₂:O₂RIE+20RH

SiO ₂ :O ₂ RIE + 20D+20RH	Component	Centre (eV)	Intensity (cps)	FWHM (eV)	Area (cps*eV)	Ratio (%)
As-received	Si-O ₂	530.3	774.024	0.6	101.275	8.1124
	Si-O ₄	533.361	5947.62	0.8	1037.6	83.1146
	Si-(OH) _x	531.665	502.233	1	109.522	8.77302
60 s	Si-O ₂	530.608	987.207	0.6	129.168	9.14167
	Si-O ₄	533.449	5639.77	1	1229.87	87.0417
	Si-(OH) _x	531.423	274.768	0.9	53.9269	3.81659
150 s	Si-O ₂	530.674	1612.33	0.8	281.28	33.3736
	Si-O ₄	533.339	2362.89	0.9	463.749	55.0233
	Si-(OH) _x	531.9	448.447	1	97.793	11.603
300 s	Si-O ₂	530.388	1956.74	0.7	298.695	31.7785
	Si-O ₄	533.2	2842.38	0.8	495.872	52.7563
	Si-(OH) _x	531.6	666.58	1	145.361	15.4652
600 s	Si-O ₂	530.6	1590.89	0.9	312.234	26.3404
	Si-O ₄	533.559	3456.88	1	753.843	63.5951
	Si-(OH) _x	532	547.087	1	119.303	10.0646
1200 s	Si-O ₂	530.586	2001.22	0.8	349.125	46.3864
	Si-O ₄	532.943	1682.38	0.9	330.189	43.8705
	Si-(OH) _x	531.8	336.273	1	73.3312	9.74313

TABLE 8: CURVE FITTING RESULTS OF O_{1s} OF SiO₂:O₂RIE+20D+20RH

SiO ₂ :O ₂ RIE + 20D+20RH	Component	Centre (eV)	Intensity (cps)	FWHM (eV)	Area (cps*eV)	Ratio (%)
As-received	Si-O ₂	530.409	1342.36	0.8	234.183	26.7476
	Si-O ₄	533.3	3149.24	0.8	549.406	62.7513
	Si-(OH) _x	531.806	421.607	1	91.9401	10.5011
60 s	Si-O ₂	530.51	1342.36	0.7	234.183	15.031
	Si-O ₄	533.3	3149.24	0.8	549.406	80.015
	Si-(OH) _x	531.801	421.607	1	91.9401	4.954
150 s	Si-O ₂	530.432	1296.71	0.7	197.942	18.4711
	Si-O ₄	533.2	3878.78	0.9	761.263	71.038
	Si-(OH) _x	531.6	515.538	1	112.424	10.4909
300 s	Si-O ₂	530.455	2500.97	0.7	381.772	35.3487
	Si-O ₄	533.272	2967.14	0.8	517.637	47.9287
	Si-(OH) _x	531.7	828.202	1	180.606	16.7226
600 s	Si-O ₂	533	3140.56	0.9	616.376	68.9611
	Si-O ₄	530.317	908.739	0.7	138.718	15.52
	Si-(OH) _x	531.348	636.069	1	138.708	15.5188
1200 s	Si-O ₂	530.615	2715.78	0.7	414.562	44.2928
	Si-O ₄	533.341	1899.11	0.8	331.312	35.3982
	Si-(OH) _x	532.012	871.665	1	190.084	20.309

REFERENCES

- [1] A. Qureshi, W. P. Kang, J. L. Davidson, and Y. Gurbuz, “Review on carbon-derived, solid-state, micro and nano sensors for electrochemical sensing applications,” *Diamond and Related Materials*, vol. 18, no. 12, pp. 1401–1420, Dec. 2009.
- [2] A. Lymberis and L. Gatzoulis., “Wearable health systems: from smart technologies to real applications.,” in *Proceedings of the 28th Annual International Conference of the IEEE Engineering in Medicine and Biology Society*, 2006, pp. 29–30.
- [3] M. Staples, K. Daniel, M. J. Cima, and R. Langer, “Application of micro- and nano-electromechanical devices to drug delivery.,” *Pharmaceutical research*, vol. 23, no. 5, pp. 847–63, May 2006.
- [4] “International Technology Roadmap for Semiconductors,” 2012.
- [5] G. Kräuter, A. Schumacher, and U. Gösele, “Low temperature silicon direct bonding for application in micromechanics: bonding energies for different combinations of oxides,” *Sensors and Actuators A: Physical*, vol. 70, no. 3, pp. 271–275, Oct. 1998.
- [6] H. Takagi, R. Maeda, T. R. Chung, and T. Suga, “Low-temperature direct bonding of silicon and silicon dioxide by the surface activation method,” *Sensors and Actuators A: Physical*, vol. 70, no. 1–2, pp. 164–170, Oct. 1998.
- [7] J. Wei, S. M. L. Nai, C. K. Wong, and L. C. Lee, “Glass-to-glass anodic bonding process and electrostatic force,” *Thin Solid Films*, vol. 462–463, pp. 487–491, Sep. 2004.
- [8] H. K. Singh, “Determining interfacial adhesion performance and reliability for microelectronics applications using a wedge test method,” Virginia Polytechnic Institute and State University, 2005.
- [9] Q. Tong, G. Cha, R. Gafiteanu, and U. Gosele, “Low Temperature Wafer Direct Bonding,” *Journal of Microelectromechanical Systems*, vol. 3, no. 1, pp. 29–35, 1994.
- [10] Q.-Y. . Tong and U. Gosele, *Semiconductor Wafer Bonding Science and Technology*. New York: John Wiley & Sons, Inc., 1999, pp. 17–24.

REFERENCES

- [11] G. Galilei, *Discorsi E Dimostrazioni Matematiche*. reprinted, edited by Le Opere (Mailand, 1938), Vol. 2., 1638.
- [12] L. Rayleigh, “A Study of Glass Surfaces in Optical Contact,” *Proceedings of the Royal Society A: Mathematical, Physical and Engineering Sciences*, vol. 156, no. 888, pp. 326–349, Aug. 1936.
- [13] H. G. Van Bueren, J. Haisma, and H. De Lang, “A small and stable continuous gas laser,” *Physics Letters*, vol. 2, no. 7, pp. 340–341, Nov. 1962.
- [14] G. A. Antypas and J. Edgecumbe, “Glass–sealed GaAs–AlGaAs transmission photocathode,” *Applied Physics Letters*, vol. 26, no. 7, p. 371, 1975.
- [15] M. Shimbo, K. Furukawa, K. Fukuda, and K. Tanzawa, “Silicon-to-silicon direct bonding method,” *Journal of Applied Physics*, vol. 60, no. 8, p. 2987, 1986.
- [16] J. B. Lasky, “Wafer bonding for silicon-on-insulator technologies,” *Applied Physics Letters*, vol. 48, no. 1, p. 78, 1986.
- [17] K. Petersen, P. Barth, J. Poydock, J. Brown, J. Mallon, and J. Bryzek, “Silicon fusion bonding for pressure sensors,” in *IEEE Technical Digest on Solid-State Sensor and Actuator Workshop*, pp. 144–147.
- [18] J. Haisma, “Direct bonding in patent literature,” *Philips Journal of Research*, vol. 49, no. 1–2, pp. 165–170, 1995.
- [19] J. Haisma, B. A. C. M. Spierings, U. K. P. Biermann, and A. A. van Gorkum, “Diversity and feasibility of direct bonding: a survey of a dedicated optical technology,” *Applied Optics*, vol. 33, no. 7, pp. 1154–1169, 1994.
- [20] T. Plach, K. Hingerl, S. Tollabimazraehno, G. Hesser, V. Dragoi, and M. Wimplinger, “Mechanisms for room temperature direct wafer bonding,” *Journal of Applied Physics*, vol. 113, no. 9, p. 094905, 2013.
- [21] R. Stengl, T. Tan, and U. Gösele, “A Model for the Silicon Wafer Bonding Process,” *Japanese Journal of Applied Physics*, vol. 28, no. Part 1, No. 10, pp. 1735–1741, Oct. 1989.
- [22] M. Reiche and T. Wilhelm, “Semiconductor Wafer Bonding.” [Online]. Available: <http://www.mpi-halle.mpg.de/departement2/research-areas/silicon-photonics-photovoltaics/wafer-bonding-light-emitters/abstract/semiconductor-wafer-bonding/>.

- [23] S. Bengtsson and O. Engström, "Interface charge control of directly bonded silicon structures," *Journal of Applied Physics*, vol. 66, no. 3, p. 1231, 1989.
- [24] Y. Backlund, K. Ljungberg, and A. Soderberg, "A suggested mechanism for silicon direct bonding from studying hydrophilic and hydrophobic surfaces," *Journal of Micromechanics and Microengineering*, vol. 2, no. 3, pp. 158–160, Sep. 1992.
- [25] K. Ljungberg, A. Söderbärg, and Y. Bäcklund, "Spontaneous bonding of hydrophobic silicon surfaces," *Applied Physics Letters*, vol. 62, no. 12, p. 1362, 1993.
- [26] Q.-Y. Tong, E. Schmidt, U. Gösele, and M. Reiche, "Hydrophobic silicon wafer bonding," *Applied Physics Letters*, vol. 64, no. 5, p. 625, 1994.
- [27] Q.-Y. Tong, "The Role of Surface Chemistry in Bonding of Standard Silicon Wafers," *Journal of The Electrochemical Society*, vol. 144, no. 1, p. 384, 1997.
- [28] M. K. Weldon, Y. J. Chabal, D. R. Hamann, S. B. Christman, and E. E. Chaban, "Physics and chemistry of silicon wafer bonding investigated by infrared absorption spectroscopy Physics and chemistry of silicon wafer bonding investigated by infrared absorption spectroscopy *," vol. 3095, no. 1996.
- [29] G. Wallis, "Field Assisted Glass-Metal Sealing," *Journal of Applied Physics*, vol. 40, no. 10, p. 3946, 1969.
- [30] A. Gerlach, D. Maas, D. Seidel, H. Bartuch, S. Schundau, and K. Kaschlik, "Low-temperature anodic bonding of silicon to silicon wafers by means of intermediate glass layers," *Microsystem Technologies*, vol. 5, no. 3, pp. 144–149, Feb. 1999.
- [31] T. Rogers and J. Kowal, "Selection of glass, anodic bonding conditions and material compatibility for silicon-glass capacitive sensors," *Sensors and Actuators A: Physical*, vol. 46, no. 1–3, pp. 113–120, Jan. 1995.
- [32] J. Wei, H. Xie, M. L. Nai, C. K. Wong, and L. C. Lee, "Low temperature wafer anodic bonding," *Journal of Micromechanics and Microengineering*, vol. 13, no. 2, pp. 217–222, Mar. 2003.
- [33] T. Suni, K. Henttinen, I. Suni, and J. Mäkinen, "Effects of Plasma Activation on Hydrophilic Bonding of Si and SiO₂," *Journal of The Electrochemical Society*, vol. 149, no. 6, p. G348, 2002.

REFERENCES

- [34] S. Guha, E. P. Gusev, H. Okorn-Schmidt, M. Copel, L.-A. Ragnarsson, N. A. Bojarczuk, and P. Ronsheim, "High temperature stability of Al₂O₃ dielectrics on Si: Interfacial metal diffusion and mobility degradation," *Applied Physics Letters*, vol. 81, no. 16, p. 2956, 2002.
- [35] S. Bengtsson and P. Amirfeiz, "Room Temperature Wafer Bonding of Silicon, Oxidized Silicon, and Crystalline Quartz," vol. 1, no. Di, pp. 909–915, 2000.
- [36] S. N. Farrens, J. R. Dekker, K. Smith, Jason, and B. E. Roberds, "Chemical Free Room Temperature Wafer To Wafer Direct Bonding," *J. Electrochem. Soc.*, vol. 142, no. 11, pp. 3949–3955, 1995.
- [37] G. Kissinger and W. Kissinger, "Hydrophilicity of Silicon Wafers for Direct Bonding," *Physica Status Solidi (a)*, vol. 123, no. 1, pp. 185–192, Jan. 1991.
- [38] A. Sanz-Velasco, P. Amirfeiz, S. Bengtsson, and C. Colinge, "Room Temperature Wafer Bonding Using Oxygen Plasma Treatment in Reactive Ion Etchers With and Without Inductively Coupled Plasma," *Journal of The Electrochemical Society*, vol. 150, no. 2, p. G155, 2003.
- [39] K. Y. Byun, I. Ferain, and C. Colinge, "Effect of Free Radical Activation for Low Temperature Si to Si Wafer Bonding," *Journal of The Electrochemical Society*, vol. 157, no. 1, p. H109, 2010.
- [40] P. Amirfeiz, S. Bengtsson, M. Bergh, E. Zanghellini, and L. Börjesson, "Formation of Silicon Structures by Plasma-Activated Wafer Bonding," vol. 147, no. 7, pp. 2693–2698, 2000.
- [41] H. Moriceau, F. Rieutord, C. Morales, and A. M. Charvet, "Surface plasma treatments enabling low temperature direct bonding," *Microsystem Technologies*, vol. 12, no. 5, pp. 378–382, Oct. 2005.
- [42] S. Choi, W. Choi, Y. Lee, and B. Ju, "Effect of oxygen plasma treatment on anodic bonding," *Journal of the Korean Physical Society*, vol. 38, no. 3, pp. 207–209, 2001.
- [43] M. M. R. Howlader, P. R. Selvaganapathy, M. J. Deen, and T. Suga, "Nanobonding Technology Toward Electronic, Fluidic, and Photonic Systems Integration," *IEEE Journal of Selected Topics in Quantum Electronics*, vol. 17, no. 3, pp. 689–703, May 2011.
- [44] V. Dragoi, G. Mittendorfer, C. Thanner, and P. Lindner, "Wafer-level plasma activated bonding: new technology for MEMS fabrication," *Microsystem Technologies*, vol. 14, no. 4–5, pp. 509–515, Oct. 2007.

- [45] M. M. R. Howlader, T. Suga, H. Itoh, T. H. Lee, and M. J. Kim, "Role of Heating on Plasma-Activated Silicon Wafers Bonding," *Journal of The Electrochemical Society*, vol. 156, no. 11, p. H846, 2009.
- [46] M. G. Kibria, F. Zhang, T. H. Lee, M. J. Kim, and M. M. R. Howlader, "Comprehensive investigation of sequential plasma activated Si/Si bonded interfaces for nano-integration on the wafer scale.," *Nanotechnology*, vol. 21, no. 13, p. 134011, Apr. 2010.
- [47] J. Arokiaraj, S. Tripathy, S. Vicknesh, and S. J. Chua, "Si layer transfer to InP substrate using low-temperature wafer bonding," *Applied Surface Science*, vol. 253, no. 3, pp. 1243–1246, Nov. 2006.
- [48] T. H. Kim, "Sequential activation process for wafer direct bonding at room temperature," The University of Tokyo, 2004.
- [49] T. H. Kim, M. M. R. Howlader, T. Itoh, and T. Suga, "Room temperature Cu–Cu direct bonding using surface activated bonding method," *Journal of Vacuum Science & Technology A: Vacuum, Surfaces, and Films*, vol. 21, no. 2, p. 449, 2003.
- [50] W. Kern, "The Evolution of Silicon Wafer Cleaning Technology," no. June, pp. 7–12, 1990.
- [51] C. Gui, M. Elwenspoek, N. Tas, and J. G. E. Gardeniers, "The effect of surface roughness on direct wafer bonding," *Journal of Applied Physics*, vol. 85, no. 10, p. 7448, 1999.
- [52] M. M. R. Howlader, S. Suehara, H. Takagi, T. H. Kim, R. Maeda, and T. Suga, "Room-Temperature Microfluidics Packaging Using Sequential Plasma Activation Process," *IEEE Transactions on Advanced Packaging*, vol. 29, no. 3, pp. 448–456, Aug. 2006.
- [53] A. Plöbl, "Wafer direct bonding: tailoring adhesion between brittle materials," *Materials Science and Engineering: R: Reports*, vol. 25, no. 1–2, pp. 1–88, Mar. 1999.
- [54] R. Stengl, K. Mitani, V. Lehmann, and U. Gosele, "Silicon wafer bonding: chemistry, elasto-mechanics, and manufacturing," in *IEEE SOS/SOI Technology Conference*, pp. 123–124.
- [55] Q.-Y. Tong, "Thickness Considerations in Direct Silicon Wafer Bonding," *Journal of The Electrochemical Society*, vol. 142, no. 11, p. 3975, 1995.

REFERENCES

- [56] H. Takagi, R. Maeda, T. R. Chung, N. Hosoda, and T. Suga, "Effect of Surface Roughness on Room-Temperature Wafer Bonding by Ar Beam Surface Activation," *Japanese Journal of Applied Physics*, vol. 37, no. Part 1, No. 7A, pp. 4197–4203, Jul. 1998.
- [57] K. Meine, K. Kloß, T. Schneider, and D. Spaltmann, "The influence of surface roughness on the adhesion force," *Surface and Interface Analysis*, vol. 36, no. 8, pp. 694–697, Aug. 2004.
- [58] A. A. Tseng, "Effects of surface roughness and oxide layer on wafer bonding strength using transmission laser bonding technique," *Thermal and Thermomechanical Proceedings 10th Intersociety Conference on Phenomena in Electronics Systems, 2006. IThERM 2006.*, pp. 1349–1357.
- [59] Z. Tang, P. Peng, T. Shi, G. Liao, L. Nie, and S. Liu, "Effect of nanoscale surface topography on low temperature direct wafer bonding process with UV activation," *Sensors and Actuators A: Physical*, vol. 151, no. 1, pp. 81–86, Apr. 2009.
- [60] N. Miki and S. M. Spearing, "Effect of nanoscale surface roughness on the bonding energy of direct-bonded silicon wafers," *Journal of Applied Physics*, vol. 94, no. 10, p. 6800, 2003.
- [61] X. Ma, C. Chen, W. Liu, X. Liu, X. Du, Z. Song, and C. Lin, "Study of the Ge Wafer Surface Hydrophilicity after Low-Temperature Plasma Activation," *Journal of The Electrochemical Society*, vol. 156, no. 5, p. H307, 2009.
- [62] M. M. R. Howlader, M. G. Kibria, F. Zhang, and M. J. Kim, "Hybrid plasma bonding for void-free strong bonded interface of silicon/glass at 200 degrees C.," *Talanta*, vol. 82, no. 2, pp. 508–15, Jul. 2010.
- [63] K. Hermansson, U. Lindberg, B. Hok, and G. Palmkog, "Wetting properties of silicon surfaces," in *TRANSDUCERS '91: 1991 International Conference on Solid-State Sensors and Actuators. Digest of Technical Papers*, 1991, pp. 193–196.
- [64] T. Corti and U. K. Krieger, "Improved inverted bubble method for measuring small contact angles at crystal-solution-vapor interfaces," *Applied Optics*, vol. 46, no. 23, p. 5835, 2007.
- [65] X. Ma, C. Chen, W. Liu, X. Liu, X. Du, Z. Song, and C. Lin, "Study of the Ge Wafer Surface Hydrophilicity after Low-Temperature Plasma Activation," *Journal of The Electrochemical Society*, vol. 156, no. 5, p. H307, 2009.
- [66] X. Ma, W. Liu, X. Du, X. Liu, Z. Song, C. Lin, and P. K. Chu, "Germanium surface hydrophilicity and low-temperature Ge layer transfer by Ge–SiO₂

- bonding,” *Journal of Vacuum Science & Technology B: Microelectronics and Nanometer Structures*, vol. 28, no. 4, p. 769, 2010.
- [67] M. Ueda, C. Lepienski, E. Rangel, N. Cruz, and F. Dias, “Nanohardness and contact angle of Si wafers implanted with N and C and Al alloy with N by plasma ion implantation,” *Surface and Coatings Technology*, vol. 156, no. 1–3, pp. 190–194, Jul. 2002.
- [68] K. J. Trevino, J. C. Shearer, B. D. Tompkins, and E. R. Fisher, “Comparing Isoelectric Point and Surface Composition of Plasma Modified Native and Deposited SiO₂ Films Using Contact Angle Titrations and X-ray Photoelectron Spectroscopy,” *Plasma Processes and Polymers*, vol. 8, no. 10, pp. 951–964, Oct. 2011.
- [69] Y. Feng, Z. Zhou, X. Ye, and J. Xiong, “Passive valves based on hydrophobic microfluidics,” *Sensors and Actuators A: Physical*, vol. 108, no. 1–3, pp. 138–143, Nov. 2003.
- [70] A. C. Fischer-Cripps, *Nanoindentation*, vol. 1. New York, NY: Springer New York, 2011, pp. 21–38.
- [71] X. Li, B. Bhushan, K. Takashima, C.-W. Baek, and Y.-K. Kim, “Mechanical characterization of micro/nanoscale structures for MEMS/NEMS applications using nanoindentation techniques.,” *Ultramicroscopy*, vol. 97, no. 1–4, pp. 481–94, 2003.
- [72] K. Tapily, H. Baumgart, D. Gu, A. Elmustafa, M. Krause, and M. Petzold, “Effect of Wafer Bonding and Layer Splitting on Nanomechanical Properties of Standard and Strained SOI Films,” *ECS Transactions*, vol. 16, no. 8, pp. 337–345, 2008.
- [73] Y. Huang, A. Sai Sarathi Vasan, R. Doraiswami, M. Osterman, and M. Pecht, “MEMS Reliability Review,” *IEEE Transactions on Device and Materials Reliability*, vol. 12, no. 2, pp. 482–493, Jun. 2012.
- [74] W. S. Su, H. Y. Huang, and W. Fang, “Tuning the Mechanical Properties of SiO₂ Thin Film Using Plasma Treatments for MEMS Applications,” in *2007 Digest of papers Microprocesses and Nanotechnology*, 2007, vol. 8483, pp. 498–499.
- [75] M. M. R. Howlader, F. Zhang, and M. G. Kibria, “Void nucleation at a sequentially plasma-activated silicon/silicon bonded interface,” *Journal of Micromechanics and Microengineering*, vol. 20, no. 6, p. 065012, Jun. 2010.

REFERENCES

- [76] K. Y. Byun, P. Fleming, N. Bennett, F. Gity, P. McNally, M. Morris, I. Ferain, and C. Colinge, "Comprehensive investigation of Ge–Si bonded interfaces using oxygen radical activation," *Journal of Applied Physics*, vol. 109, no. 12, p. 123529, 2011.
- [77] T. L. Barr, "An XPS study of Si as it occurs in adsorbents, catalysts, and thin films," *Applications of Surface Science, North-Holland Publishing Company*, vol. 15, pp. 1–35, 1983.
- [78] V. A. Labunov and P. V. Protasevich, "XPS and AES investigations of Silicon by ion-implanted oxygen," *Nuclear Instruments and Methods in Physics Research, North-Holland, Amsterdam*, vol. B39, pp. 466–468, 1989.
- [79] S. Vepiek, Z. Iqbal, H. R. Oswald, and A. P. Webb, "Properties of polycrystalline silicon prepared by chemical transport in hydrogen plasma at temperatures between 80 and 400 degrees C," *J. Phys. C: Solid State Phys*, vol. 14, pp. 295–308, 1981.
- [80] K. T. Sung, "Oxidation of silicon in an oxygen plasma generated by a multipolar electron cyclotron resonance source," *Journal of Vacuum Science & Technology B: Microelectronics and Nanometer Structures*, vol. 10, no. 5, p. 2211, Sep. 1992.
- [81] T. Hattori, H. Yamagishi, N. Koike, K. Imai, and K. Yamabe, "Structural studies of ultrathin silicon oxides and their interfaces by XPS," *Applied Surface Science*, vol. 41–42, pp. 416–419, Nov. 1989.
- [82] S. A. Nelson, H. D. Hailen, and R. A. Buhrman, "A structural and electrical comparison of thin SiO₂ films grown on silicon by plasma anodization and rapid thermal processing to furnace oxidation," *J. Appl Phys*, vol. 63, pp. 5027–5035, 1988.
- [83] A. Mekki, D. Holland, C. F. McConville, and M. Salim, "An XPS study of iron sodium silicate glass surfaces," *Journal of Non-Crystalline Solids*, vol. 208, no. 3, pp. 267–276, Dec. 1996.
- [84] Y. C. Araujo, P. G. Toledo, V. Leon, and H. Y. Gonzalez, "Wettability of Silane-Treated Glass Slides as Determined from X-Ray Photoelectron Spectroscopy," *Journal of Colloid and Interface Science*, vol. 176, no. 2, pp. 485–490, Dec. 1995.
- [85] J. Park and A. Tseng, "Transmission laser bonding of glass with silicon wafer," in *Proceedings of 2004 JUSFA*, 2004, pp. 1–7.
- [86] A. A. Tseng, J.-S. Park, G. P. Vakanas, H. Wu, M. Raudensky, and T. P. Chen, "Influences of interface oxidation on transmission laser bonding of wafers for

- microsystem packaging,” *Microsystem Technologies*, vol. 13, no. 1, pp. 49–59, Sep. 2006.
- [87] T. Miura, Y. Benino, R. Sato, and T. Komatsu, “Universal hardness and elastic recovery in Vickers nanoindentation of copper phosphate and silicate glasses,” *Journal of the European Ceramic Society*, vol. 23, no. 3, pp. 409–416, Mar. 2003.
- [88] M. M. R. Howlader, G. Kagami, S. H. Lee, J. G. Wang, M. J. Kim, and A. Yamauchi, “Sequential Plasma-Activated Bonding Mechanism of Silicon/Silicon Wafers,” *Journal of Microelectromechanical Systems*, vol. 19, no. 4, pp. 840–848, Aug. 2010.
- [89] F. Zhang, M. Kibria, K. Cormier, and M. Howlader, “Surface and Interface Characterization of Sequentially Plasma Activated Silicon, Silicon dioxide and Germanium Wafers for Low Temperature Bonding Applications,” in *ECS Transactions*, 2010, vol. 33, no. 4, pp. 329–338.
- [90] M. M. R. Howlader, S. Suehara, and T. Suga, “Room temperature wafer level glass/glass bonding,” *Sensors and Actuators A: Physical*, vol. 127, no. 1, pp. 31–36, Feb. 2006.
- [91] S. Luo and C. P. Wong, “Influence of temperature and humidity on adhesion of underfills for flip chip packaging,” *IEEE Transactions on Components and Packaging Technologies*, vol. 28, no. 1, pp. 88–94, Mar. 2005.
- [92] A. U. Alam, M. M. R. Howlader, and M. J. Deen, “Effect of Oxygen Plasma and Humidity on Surface Roughness, Water Contact Angle and Hardness of Silicon, Silicon Dioxide and Glass,” *Journal of Micromachining and Microengineering*, unpublished manuscript submitted.
- [93] A. U. Alam, M. M. R. Howlader, and M. J. Deen, “Oxygen Plasma and Humidity Dependent Surface Analysis of Silicon, Silicon Dioxide and Glass for Direct Wafer Bonding,” *Journal of Electrochemical Society*, vol. 2, no. 12, P515-P523, 2013.
- [94] R. A. Wilson and H. A. Bullen, “Introduction to Scanning Probe Microscopy (SPM), Basic Theory Atomic Force Microscopy (AFM).”
- [95] “Atomic Force Microscopy (AFM).” [Online]. Available: <http://pharm.virginia.edu/AFM.html>. [Accessed: 16-Sep-2013].
- [96] K. Boussu, B. Van der Bruggen, a Volodin, J. Snauwaert, C. Van Haesendonck, and C. Vandecasteele, “Roughness and hydrophobicity studies of nanofiltration

REFERENCES

- membranes using different modes of AFM.,” *Journal of colloid and interface science*, vol. 286, no. 2, pp. 632–8, Jun. 2005.
- [97] S. S. Lyer and A. J. Auberton-Hervé, *Silicon Wafer Bonding Technology: For VLSI and MEMS Applications*. London: INSPEC, 2002.
- [98] KRÜSS, “Contact angle.” [Online]. Available: <http://www.kruss.de/en/theory/measurements/contact-angle/measurement-contact-angle.html>. [Accessed: 28-Aug-2013].
- [99] ramé-hart, “Information on Contact Angle.” [Online]. Available: <http://www.ramehart.com/contactangle.htm>. [Accessed: 16-Sep-2013].
- [100] Shimadzu, “Short Manual, DUH-211 DUH-211S.”
- [101] Shimadzu, “SHIMADZU Dynamic Ultra-micro Hardness Tester.”
- [102] JEOL, “Handbook of X-ray Photoelectron Spectroscopy,” Japan, 1991.
- [103] R. Paynter, “XPS Theory.” [Online]. Available: http://csacs.mcgill.ca/francais/docs/CHEM634/XPS_Paynter_t.pdf. [Accessed: 16-Sep-2013].
- [104] “Espec Products.” [Online]. Available: http://www.espec.com/na/gallery/image_med/181/platinous. [Accessed: 01-Oct-2013].
- [105] D.-I. Kim, K.-H. Kim, and H.-S. Ahn, “Tribological properties of adsorbed water layer on silicon surfaces,” *International Journal of Precision Engineering and Manufacturing*, vol. 11, no. 5, pp. 741–746, Oct. 2010.
- [106] N. Miki and S. M. Spearing, “Effect of nanoscale surface roughness on the bonding energy of direct-bonded silicon wafers,” *Journal of Applied Physics*, vol. 94, no. 10, p. 6800, 2003.
- [107] N. Pussadee, “Poly(dimethylsiloxane) Based Micro- and Nanofluidic Device Fabrication for Electrophoresis Applications,” Ohio State University, 2010.
- [108] D. Pasquariello, C. Hedlund, and K. Hjort, “Oxidation and Induced Damage in Oxygen Plasma In Situ Wafer Bonding,” *Journal of The Electrochemical Society*, vol. 147, no. 7, p. 2699, 2000.

- [109] R. H. Esser, K. D. Hobart, and F. J. Kub, "Improved Low-Temperature Si-Si Hydrophilic Wafer Bonding," *Journal of The Electrochemical Society*, vol. 150, no. 3, p. G228, 2003.
- [110] M. G. Kibria, "Sequentially Plasma Activated Bonding for Wafer Scale Nano-Integration," McMaster University, 2010.
- [111] T. Plach, K. Hingerl, S. Tollabimazraehno, G. Hesser, V. Dragoi, and M. Wimplinger, "Mechanisms for room temperature direct wafer bonding," *Journal of Applied Physics*, vol. 113, no. 9, p. 094905, 2013.
- [112] W. Eaton and J. Smith, "Micromachined pressure sensors: review and recent developments," *Smart Materials and Structures*, vol. 530, 1997.
- [113] H.-B. Fang, J.-Q. Liu, Z.-Y. Xu, L. Dong, L. Wang, D. Chen, B.-C. Cai, and Y. Liu, "Fabrication and performance of MEMS-based piezoelectric power generator for vibration energy harvesting," *Microelectronics Journal*, vol. 37, no. 11, pp. 1280–1284, Nov. 2006.
- [114] J. R. Ligenza, "Oxidation of Silicon by High-Pressure Steam," *Journal of The Electrochemical Society*, vol. 109, no. 2, p. 73, 1962.
- [115] M. M. R. Howlader and T. E. Doyle, "Low temperature nanointegration for emerging biomedical applications," *Microelectronics Reliability*, vol. 52, no. 2, pp. 361–374, Feb. 2012.
- [116] W. D. Nix, "Elastic and plastic properties of thin films on substrates: nanoindentation techniques," *Materials Science and Engineering: A*, vol. 234–236, pp. 37–44, Aug. 1997.
- [117] D. P. Holmes, B. Tavakol, G. Froehlicher, and H. A. Stone, "Control and manipulation of microfluidic flow via elastic deformations," *Soft Matter*, vol. 9, no. 29, p. 7049, 2013.
- [118] W. Kern, "The Evolution of Silicon Wafer Cleaning Technology," *Journal of The Electrochemical Society*, vol. 137, no. 6, p. 1887, 1990.
- [119] M. Grundner and H. Jacob, "Investigations on hydrophilic and hydrophobic silicon (100) wafer surfaces by X-ray photoelectron and high-resolution electron energy loss-spectroscopy," *Applied Physics A Solids and Surfaces*, vol. 39, no. 2, pp. 73–82, Feb. 1986.

REFERENCES

- [120] S. P. Kobeleva, T. G. Sergeeva, B. M. Leiferov, and a. L. Ivanova, "XPS and PL studies of porous silicon treated in water and oxygen-rich gases," *Physica A: Statistical Mechanics and its Applications*, vol. 241, no. 1–2, pp. 398–402, Jul. 1997.
- [121] J. R. Ligenza, "Effect of crystal orientation on oxidation rates of silicon in high pressure steam," *Journal of Physical Chemistry*, vol. 65, no. 11, pp. 2011–2014, Nov. 1961.
- [122] R. E. Oosterbroek, J. W. Berenschot, H. V. Jansen, A. J. Nijdam, G. Pandraud, A. van den Berg, and M. C. Elwenspoek, "Etching methodologies in <111>-oriented silicon wafers," *Journal of Microelectromechanical Systems*, vol. 9, no. 3, pp. 390–398, Sep. 2000.
- [123] A. Verdaguer, C. Weis, G. Oncins, G. Ketteler, H. Bluhm, and M. Salmeron, "Growth and structure of water on SiO₂ films on Si Investigated by Kelvin probe microscopy and in Situ X-ray spectroscopies.," *Langmuir : the ACS journal of surfaces and colloids*, vol. 23, no. 19, pp. 9699–703, Sep. 2007.
- [124] F. Leisenberger, R. Duschek, R. Czaputa, F. P. Netzer, G. Beamson, and J. a. D. Matthew, "A high resolution XPS study of a complex insulator: the case of porous silicon," *Applied Surface Science*, vol. 108, no. 2, pp. 273–281, Feb. 1997.
- [125] O. Guaitella, M. Hübner, S. Welzel, D. Marinov, J. Röpcke, and a Rousseau, "Evidence for surface oxidation on Pyrex of NO into NO₂ by adsorbed O atoms," *Plasma Sources Science and Technology*, vol. 19, no. 4, p. 045026, Aug. 2010.
- [126] M. M. R. Howlader, F. Zhang, and M. Jamal Deen, "Formation of gallium arsenide nanostructures in Pyrex glass.," *Nanotechnology*, vol. 24, no. 31, p. 315301, Aug. 2013.
- [127] J.-W. He, X. Xu, J. S. Corneille, and D. W. Goodman, "X-ray photoelectron spectroscopic characterization of ultra-thin silicon oxide films on a Mo(100) surface," *Surface Science*, vol. 279, no. 1–2, pp. 119–126, Dec. 1992.